A Study on Characterization of One-dimensional Semiconductor Nanomaterials by Microwave Atomic Force Microscopy

Department of Micro-Nano Mechanical Science and Engineering, Nagoya University

Minji Zhao

Content

Chapter 1 Introduction

1.1 Semiconductor one-dimensional nanomaterials

In recent years, the continuous advances of nanotechnology lead to the synthesis and characterization of one-dimensional nanostructures in a group of different nanostructures such as nanowires, nanoneedles, nanobelts and nanotubes [1-3]. Particularly, the metal oxide nanomaterials have drawn a rising interest for both fundamental researches and electronic industry. Owing to their unique geometry with high aspect ratio, the one-dimensional nanomaterials have well-defined chemical composition, surface terminations, higher surface-to-volume ratio [4]. Additionally, the surface effects of these fascinating materials are of great significance because of the high specific surface that caused a high-performance chemical property, such as applications in different catalyst and chemical adsorption [5-8]. These materials with well-defined crystal structures and increased surface vacancies are vitally promising for the applications in gas sensors with promoted stabilities, especially in polycrystalline systems that related to grain coalescence and unsteadiness of different electrical properties. They have now been widely used in many areas, such as transparent electronics, piezoelectric transducers, ceramics, catalysis, sensors, electro-optical and electro-chromic devices [9-11].

Among the different types of semiconductor one-dimension nanomaterials, ZnO,

CuO and SnO_2 are common and diverse materials among the various groups of semiconductors.

CuO is an interesting metal oxide and has a variety of application. The cupric oxide one-dimensional nanomaterials have high sensitivity for toxic gases such as carbon monoxide [12-14], nitrogen dioxide [12,15] and hydrogen sulfide [13,16,17]. In addition, this material shows promising applications in rechargeable battery electrodes, photovoltaics, infrared detectors and field emitting devices.

As an n-type semiconductor material, SnO_2 has a relatively large band gap [18,19] with a high optical transparency and an advanced electrical conductivity that are different from other Group IV element semiconductors. For instance, the superior optical transparency of SnO_2 make it suitable to fabricate optically passive component in a variety of different devices [20-22]. Recently, one-dimensional SnO_2-based gas sensors such as nanobelts [23], nanorods [24], nanowires [25], and nanotubes [26] have been reported to show higher responses compared with those of bulk and thin film-based sensors due to their ultrahigh surface area-to-volume ratio [27]. Research about SnO_2 nanomaterials have gain a great popularity recently due to its promoted properties and promising applications in solar cells [28], catalyst chemical material [29, 30], and different chemical sensors, etc. [31,32]. On the other hand, SnO_2 nanowire is of particular interest for metal-oxide-based field effect transistors based on its surface sensitivity to adsorbents of oxidizing and reducing gases. Tremendous efforts have been devoted to developing SnO_2 nanowire with the goal of producing a new generation of high-performance devices including electronic devices [33,34], gas sensors [35,36] and

biosensors [37,38].

The zinc oxide (ZnO) is a commercially important material used in protective coating, sunscreens and paints owe to its low cost and nontoxic property. In the past decade, ZnO thin films and different nanostructures have been fabricated. Comparing with various wide band gap semiconductors, ZnO with a band gap of 3.37 eV has been considered as one of the best candidates for economic and large-scale optoelectronic applications [39,40]. Because of their unique structural one-dimensionality and possible quantum confinement effects in two dimensions [41], ZnO nanowires can possess novel electronic and optical properties with uses as, field-effect transistors [42], photodetectors [43] and solar cells [44].

1.2 Evaluation of electrical properties of semiconductor one-dimensional nanomaterials

Evaluation of the local electrical properties of semiconductor one-dimensional nanomaterials is significant [45-50] because of their wide applications in electronic devices, gas sensors and chemical sensors. Among the different electrical properties, the relative permittivity and electrical conductivity of the semiconductor one-dimensional nanomaterials are evaluated in this research.

In recent years, the nanomaterial based high frequency electronic devices are of interest for applications in high-speed logic integrated circuit, communication devices,

and optics that are operated at around 100 GHz [51] [52]. When the devices are operated at high frequency that from 100 GHz to several terahertz, the relative permittivity and electrical conductivity of the nanomaterial will change, which is different from the situation without the external AC electric field. Thus, the evaluation of the electrical properties around 100 GHz is significant to accurately model the data and determining the high-frequency electrical properties.

According to our information, the relative permittivity is a significant parameter since it determines the application of a materials. The material with a low permittivity is desirable for applications such as high-speed integrated circuits and some nanodevices [53], while that with a high permittivity can be used for high energy storage [54]. With the prevalence of the high-performance nanomaterials, metrology tools are urgently needed to quantitatively characterize electrical properties at the nanoscale.

On the other hand, during the utmost important hunt for the newer nanomaterials with applicable properties in nano-electronics devices, a variety of nanomaterials are fabricated with different electrical conductivities that stem from the density and arrangement of dopant, impurity atoms, carrier density and carrier mobility. Evaluation of the local electrical conductivity of the one-dimensional nanomaterials is proved greatly significant because of the following two reasons. Firstly, it helps to understand the nature of the nanomaterials and pave the path to optimize different nano-electronic devices. Secondly, it helps to understand the change in conductance induced by gas adsorption, light response [55] and optoelectronic devices [56].

Field effect transistors (FETs) have played a significant role in the electronics industry since the middle of the last century. The FET device includes source and drain electrodes contacting a semiconductor. A dielectric material is placed on one interface of the semiconductor, and a gate electrode is placed at the opposite one. The gate voltage is able to control the carrier density in the semiconductor. When the semiconductor one-dimensional nanomaterials are utilized in the FET, the electronic properties and sensitivity of the device will be significantly improved [57][58]. Meanwhile, the nanomaterial FET device can be fabricated in ultra-small dimensions [59]. Because of these advantages, the nanomaterial FET not only is a basic electronic device but also exhibits a broad range of applications in high-performance devices such as in gas sensors, biosensors and optoelectronic devices [60-63]. Thus, the evaluation of the electrical properties of nanomaterial FET is extremely significant.

Previous studies on nanowire FETs are mostly based on two-terminal measurement method [64][65] and four-terminal measurement method [66] which can measure the output characteristic. Although the results from previous measurements illustrated the characteristics of the entire nanowire devices, these methods fail to measure the local electrical property of the one-dimensional nanomaterial FET devices. In order to characterize the electrical features of nanomaterials, serval techniques based on atomic force microscope (AFM) including scanning kelvin probe microscopy, electron force microscopy, microwave impedance microscopy and microwave atomic force microscopy are springing up in recent years.

1.2.1 Scanning kelvin probe microscopy

Scanning Kelvin probe force microscopy (KPFM) is a scanning probe microscopy (SPM) that is a modification of AFM and associated techniques [67-71]. The topography and potential distribution of a surface can be simultaneously mapped with this technique. The probe tip operates at a close distance from the surface, which enables the enhanced spatial resolution relative to a standard Kelvin probe. KPFM is developed and first use to study photoresist-covered Si wafers [72] and semiconductor dopant profiles [73].

Recently, the KPFM with AFM surface-approach spectroscopy methods are used for characterizing in-plane piezoelectric potential of ZnO nanowires [74]. The measurement results directly observed the of carrier concentration coupling phenomenon in ZnO nanowire. In another research, the SKPM is used to study the shifts of the Fermi levels, and the changes in surface band bending in a single GaN nanowire [75]. The obtained quantitative electrical information has been applied to the study of nanowire p-n junctions with an extremely high resolution. However, this technique works in contact mode which may cause damage to the evaluated sample.

1.2.2 Electrostatic Force Microscopy

Electrostatic Force Microscopy (EFM) is mainly devoted to voltage detection and

can measure local dc voltage in a contact mode [76]. By applying a voltage between a sample and the EFM probe, the local voltage as well as the electrostatic force can be measured [77]. The capacitance between the tip and sample can also be evaluated. EFM was used on materials where normally existed surface voltages need to detect and structures where the effects of external applied voltage need to analyze. Recently the EFM technique was used to observe charge generation of a conjugated polymer solar cell [78].

1.2.3 Microwave Impedance Microscopy

Microwave impedance microscopy (MIM) is a scanning probe technique that characterizes local complex permittivity of solid-state samples [79]. In a typical MIM operation, electrical signal is sent to a metal tip and generates a strong electric field near the tip apex which is screened by the material through dielectric and conductive response. MIM was applied to measure the electrical conductivity and relative permittivity of a series of bulk dielectrics [80] and nanoribbons [81] in tapping mode with high resolution (300 nm) [80].

1.2.4 Microwave atomic force microscopy

To combine the strong points of AFM and those of the microwave measurement

method, microwave atomic force microscopy (M-AFM) has been developed to be able to evaluate the topographic and microwave images at the same time at nanoscale. Along with the scientific exploration, the M-AFM technique has also undergone continuous improvements over the years. Different from the techniques introduced above in terms of mechanism, M-AFM measured the reflected microwave signal and that is used to calculate the conductivity of the sample [82].

The probe of M-AFM has a unique wave guide that can propagate and receive the microwave signal as shown in Fig. 1.1 [82] [83]. Because of the special structure of the probe that combines the parallel plate waveguide and high-resolution AFM probe, the M-AFM technique can quantitatively evaluate the topographic images and reflected microwave signals at nanoscale in non-contact mode [84].

For instance, the conductivity of metallic films was evaluated by M-AFM in Fig. 1.2 [82]. M-AFM has high resolution which is about 170 nm. However, from Fig. 1.2 (a) to (e), the measured topography of the film provides little surface characteristics. Thus, in this research, the advantages of M-AFM are not fully revealed. Based on the contribution of this study, the full merits of M-AFM will be shown in future study.

In previous research, the evaluation of electrical conductivity [82] and relative permittivity is developed by M-AFM technique on bulk material. Keeping a standoff distance between the M-AFM probe and sample, M-AFM can characterize the topographic images of the sample, the reflected microwave images and the atomic interaction caused by incident microwave on the sample surface at the same time. In this research, a novel evaluation method containing a theoretical model and a

calibration technique is established to quantitatively evaluate the local conductivity that was developed on a series of metal films. Thus, this research demonstrates that the quantitative evaluation of the local electrical conductivity has been realized by M-AFM at the nanoscale.

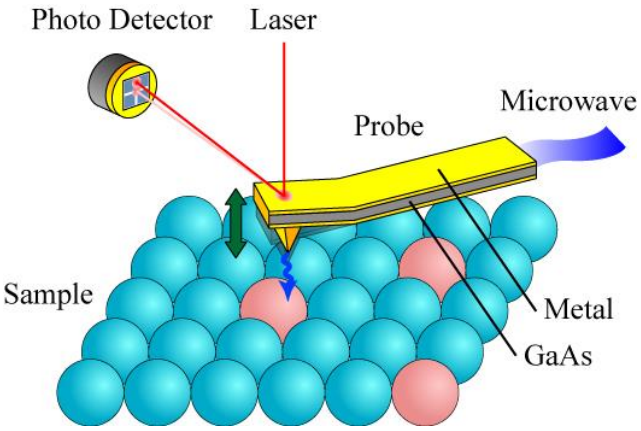

Fig. 1.1 The schematic diagram of the M-AFM

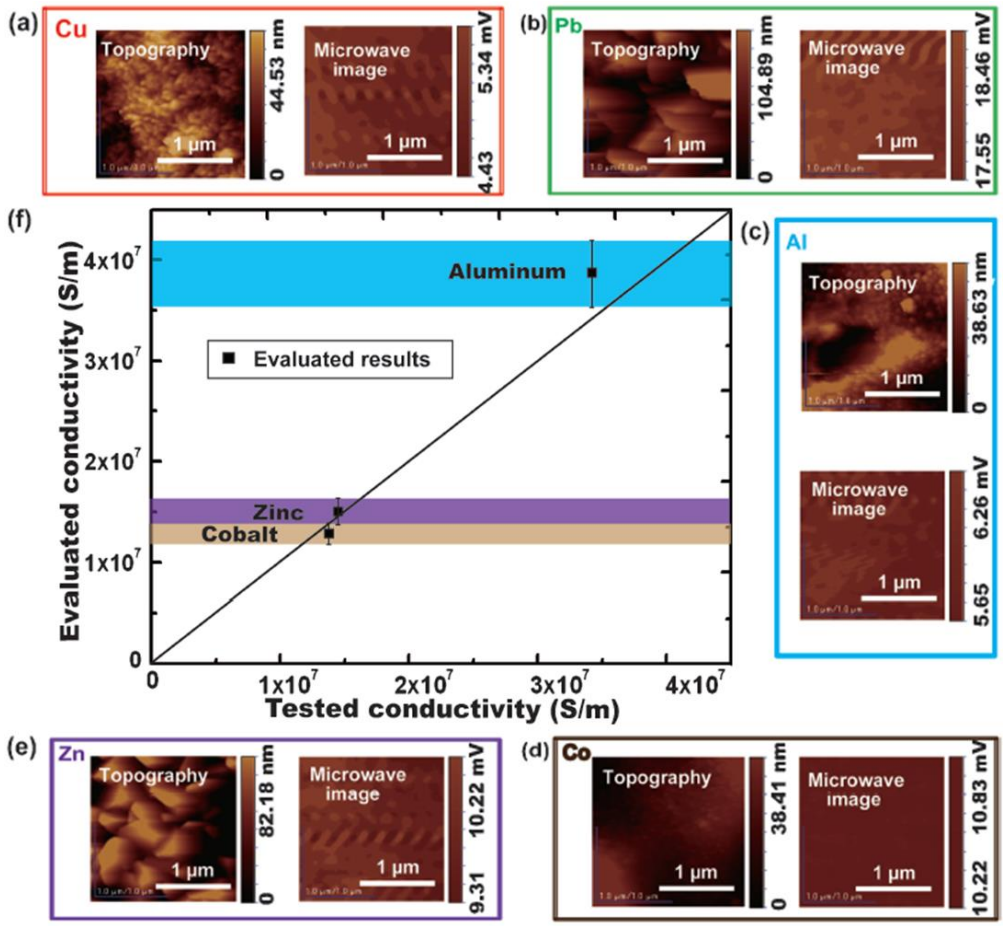

Fig. 1.2 (a)-(e) Topographies and microwave images of a series of metal materials; (f) evaluated conductivities of the samples in comparison with tested conductivities. [82]

For the dielectric materials, the relative permittivity is much more significant than electrical conductivity [85]. Recently, the relative permittivity of the dielectric materials was developed by M-AFM. This study established a theoretical model and analyzed the influence of microwave on the interatomic force between the tip of the M-AFM probe and the sample. This study also provides an evaluation equation as well as a calibration method to quantitatively evaluate the relative permittivity of the sample by the force gradient curves between the tip of the M-AFM probe and sample. Utilizing the theoretical model and the evaluation equation, the local relative permittivity of

different kinds of semiconductor bulk materials were respectively obtained. In Fig. 1.3, the evaluated relative permittivity by M-AFM is in agreement with the nominal relative permittivity from reference. This research provides a novel evaluation method for the local relative permittivity of dielectric materials in a non-contact and non-destructive fashion. Different from SKPM, EFM and MIM that measure images of electrical properties between a probe and a sample with electrode-like probe, M-AFM probe functions like a microwave sensor which measures the reflected local microwave signal and evaluates the relative permittivity as well as the conductivity. Although this study established a theoretical model to measure the relative permittivity with high accuracy by the unique feature of M-AFM, the samples in this research, Ge wafer, ZrO_2 films and Al_2O_3 films, are bulk materials. As M-AFM is more suitable to evaluate the nanomaterials because of its high resolution, sensitivity and non-destructive characteristic, further research is needed to reveal the advantages of M-AFM technique in nanomaterials.

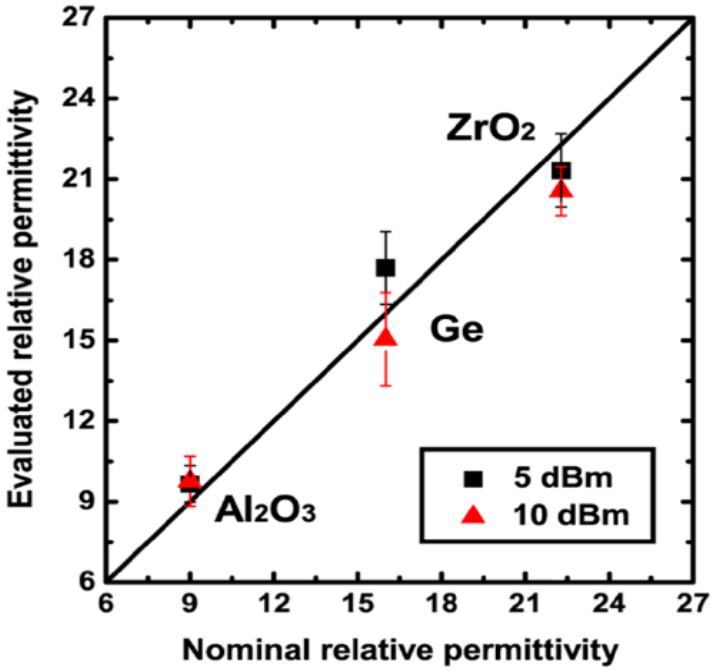

Fig. 1.3 The evaluated relative permittivity by M-AFM compared with nominal relative permittivity

1.3 Objective

This study aims at evaluating the electrical properties of semiconductor one-dimensional nanowires quantitatively in a non-contact mode by M-AFM.

There are several unresolved issues in the current AFM based techniques such as SKPM, EFM and MIM. Firstly, since they work in contact or tapping mode, which could damage the nanomaterials. Secondly, the resolution of tapping mode MIM is above 300 nm, which is insufficient to evaluate the one-dimensional nanomaterials. In addition, the conductivity of nanomaterial FETs is difficult to measure quantitatively.

The previous researches in M-AFM provided us with a series of theoretical models to solve these issues. They evaluated the electrical conductivity of metallic bulk

material and relative permittivity of dielectric bulk materials in nanometer scale, respectively. Here, by applying the theoretical models, the electrical properties of different nanowires and nanobelt devices are quantitatively evaluated in non-contact mode with high resolution. The research objective is accomplished through the following goals.

1) To investigate the theoretical model of evaluating the relative permittivity by M-AFM, a theoretical model based on nearfield approximation will be established to describe the dependence of the electrical field on the probe-sample distance in Chapter 3. The effect of microwave on the interaction between the tip and sample will be clarified. By utilizing this effect caused by microwave, a quantitative distance dependence can be obtained, which will provide a prerequisite theoretical support for a non-contact evaluation in a near-field region.

2) To evaluate the local relative permittivity of the semiconductor one-dimensional nanowires, the relative permittivity of different semiconductor one-dimensional nanowires will be evaluated in Chapter 3. To increase the difference of reflectivity between the substrate and nanowires and to visualize the nanowires in microwave image, the silicon wafer substrates coated with a 100 nm Au film will be used in the experiment. The topography and microwave image of nanowires will be measured by M-AFM. Several points will be selected from the topography image and the force distance curves on those points will be measured with and without microwave.

From the force curves, the local relative permittivity will be evaluated.

3) To investigate the theoretical model of evaluating the electrical conductivity by M-AFM, a nondestructive method to measure the electrical conductivity of semiconductor material using M-AFM will be built up in Chapter 4. The distinguishing features of M-AFM are its ability to maintain a constant standoff distance between the probe tip and the sample surface and to measure the microwave signal interacted with the sample. By the reflected microwave signal, the reflection coefficient of the material can be calculated and thus the electrical conductivity can be obtained. Both the topography and electrical conductivity images of the sample will be simultaneously characterized.

4) To evaluate the electrical conductivity of SnO_2 nanobelt FET under a changing external voltage, the electrical conductivity of SnO_2 FET will be evaluated in Chapter 4. First, the SnO_2 nanobelt FET will be fabricated. Then the output characteristic as well as the electrical conductivity of the SnO_2 nanobelt FET will be measured by two-terminal measurement method. M-AFM will be applied to measure the SnO_2 nanobelt FET under different gate-source voltages with the same drain-source voltage. The result evaluated by M-AFM will be compared with that of terminal measurement method.

1.4 Thesis organization

In this thesis, comprehensive research on the application of M-AFM on the semiconductor nanomaterials was presented.

Chapter 1 introduced the background of this research, and the objectives of this study.

In Chapter 2, the principles of the AFM and microwave measurement system of M-AFM were respectively introduced. Particularly the working principle of M-AFM and the mechanism of the microwave measurement method based on the M-AFM were respectively introduced. Next, the fabrication of the M-AFM probe was introduced. The SEM images of the fabrication results after each step were illustrated. In order to evaluate the fabricated probes, the experiment which applying the fabricated probes was carried out a sample consisted with Au film and Si substrate. The evaluated results measured by M-AFM were presented and discussed, which demonstrates that the fabricated M-AFM probes can precisely evaluate the topography and microwave image on the nanometer scale.

Chapter 3 mainly focuses on the quantitative characterization of the local relative permittivity on the nanometer scale. Based on the force curve measurement method and the additional force caused by microwave between M-AFM and sample, a novel analytical method and evaluation equations to evaluate the local relative permittivity of one-dimensional nanomaterials were proposed. One reference material was used as a reference material for calibration and the relative permittivity of each kind of nanomaterials were evaluated respectively.

In Chapter 4, the field effect of the one-dimensional metal oxide nanomaterials was studied by M-AFM. First of all, the SnO_2 nanobelt FET was fabricated. Secondly the output characteristic of the fabricated SnO_2 nanobelt FET and the electrical conductivity were measured by a parametric test fixture. Finally, M-AFM was utilized to measure the SnO_2 nanobelt FET under different gate-source voltages with the same drain-source voltage. The experimental result shows that the change of electrical conductivity of the SnO_2 nanobelt under different gate-source voltages can be distinguished by M-AFM.

Finally, the most significant achievements in this study were summarized and respectively discussed in Chapter 5.

Reference

[1] P. Yang, H. Yan, S. Mao, R. Russo, J. Johnson, R. Saykally, N. Morris, J. Pham, R. He, and H. Choi, Controlled growth of ZnO nanowires and their optical properties, Adv. Mater, **12**, 323 (2002).

[2] T. Zhai, H. Zhong, Z. Gu, A. Peng, H. Fu, Y. Ma, Y. Li, and J. Yao, Manipulation of the morphology of ZnSe sub-micro structures using CdSe nanocrystals as the seeds, J. Phys.Chem. C, **111**, 2980 (2007).

[3] C. M. Lieber, and Z. Wang, Functional nanowires, MRS Bull, **32**, 99 (2007).

[4] Z. Wang, Characterizing the structure and properties of individual wire-like nanoentities, Adv Mater, **12**, 1295 (2000).

[5] S. Lettieri, A. Bismuto, P. Maddalena, C. Baratto, E. Comini, G. Faglia, et al., Gas sensitive light emission properties of tin oxide and zinc oxide nanobelts, J Non-Cryst Solids, **352**, 1457 (2006).

[6] E. Comini, G. Faglia, G. Sberveglieri, Z. Pan, and Z. Wang, Stable and highly sensitive gas sensors based on semiconducting oxide nanobelts, Appl Phys Lett, **81**, 1869 (2002).

[7] Y. Zhang, A. Kolmakov, S. Chretien, H. Metiu, and M. Moskovits, Control of catalytic reactions at the surface of a metal oxide nanowire by manipulating electron density inside it, Nano Lett, **4**, 403 (2004).

[8] M. Huang, Y. Wu, H. Feick, N. Tran, E. Weber, and P. Yang, Catalytic growth of zinc oxide nanowires by vapor transport, AdvMater, **13**, 113 (2001).

[9] G. Shen, P. Chen, K. Ryu, and C. Zhou, Devices and chemical sensing applications

of metal oxide nanowires, J. Mater. Chem., **19**, 828 (2009).

[10] J. Lu, P. Chang, and Z. Fan, Quai-one-dimensional metal oxide materials-synthesis, properties and applications, Mater. Sci. Eng. R., **52**, 49 (2006).

[11] A. Kolmakov, and M. Moskovits, Chemical sensing and catalysis by one-dimensional metal-oxide nanostructures, Annu. Rev. Mater. Res., **34**, 151 (2004).

(12) Y. Kim, I. Hwang, S. Kim, C. Lee, and J. Lee, CuO nanowire gas sensors for air quality control in automotive cabin, Sens. Actuators B, **135**, 298 (2008).

(13) S. Steinhauer, E. Brunet, T. Maier, G. Mutinati, A. Köck, O. Freudenberg, C. Gspan, W. Grogger, A. Neuhold, and R. Resel, Gas sensing properties of novel CuO nanowire devices, Sens. Actuators B, **187**, 50 (2013).

(14) S. Steinhauer, V. Singh, C. Cassidy, C. Gspan, W. Grogger, M. Sowwan, and A. Köck, Single CuO nanowires decorated with sizeselected Pd nanoparticles for CO sensing in humid atmosphere, Nanotechnology, **26**, 175502 (2015).

(15) D. Li, J. Hu, R. Wu, and J. Lu, Conductometric chemical sensor based on individual CuO nanowires, Nanotechnology, **21**, 485502 (2010).

(16) J. Chen, K. Wang, L. Hartman, and W. Zhou, H2S detection by vertically aligned CuO nanowire array sensors, J. Phys. Chem. C, **112**, 16017 (2008).

(17) H. Kim, C. Jin, S. Park, S. Kim, and C. Lee, H2S gas sensing properties of bare and Pd-functionalized CuO nanorods, Sens. Actuators B, **161**, 594 (2012).

[18] S. Kucheyev, T. Baumann, P. Sterne, Y. Wang, T. van Buuren, A. Hamza, et al., Surface electronic states in three dimensional SnO2 nanostructures, Phys Rev B, **72**, 035404 (2005).

[19] Y. Suda, H. Kawasaki, J. Namba, K. Iwatsuji, K. Doi, and K. Wada, Properties of palladium doped tin oxide thin films for gas sensors grown by PLD method combined with sputtering process, Surf. Coat Tech., **1293**, 174 (2003).

[20] H. Hosono, Y. Mishima, H. Takezoe, and K. Mackenzie, Nanomaterials: from research to applications, London: Elsevier Ltd., (2006).

[21] A. Walsh, L. Silva, and S. Wei, Origins of band gap renormalization in degenerately doped semiconductors, Phys. Rev. B, **78**, 075211 (2008).

[22] T. Minami, Transparent conducting oxide semiconductors for transparent electrodes, Semicond Sci. Technol, **20**, 35 (2005).

[23] E. Comini, G. Faglia, G. Sberveglieri, Z. Pan, and L. Zhong, Stable and high-sensitive gas sensors based on semiconducting oxide nanobelts, Appl. Phys. Lett., **81**, 1869 (2002).

[24] D. Wang, X. Chu, and M. Gong, Gas-sensing properties of sensors based on singlecrystalline SnO2 nanorods prepared by a simple molten-salt method, Sens. Actuators B, **117**, 183 (2006).

[25] V. Sysoev, J. Goschnick, T. Schneider, E. Strelcov, and A. Kolmakov, A gradient microarray electronic nose based on percolating SnO2 nanowire sensing elements, Nano Lett., **7**, 3182 (2007).

[26] T. Hamaguchi, N. Yabuki, M. Uno, S. Yamanaka, M. Egashira, Y. Shimizu, and T. Hyodo, Synthesis and H2 gas sensing properties of tin oxide nanohole arrays with various electrodes, Sens. Actuators B, **113**, 852 (2006).

[27] B. Wang, L. Zhu, Y. Yang, N. Xu, and G. Yang, Fabrication of a SnO2 nanowire

gas sensors and sensor performance for hydrogen, J. Phys. Chem. C, **112**, 6643 (2008).

[28] S. Vishwakarma, Rahmatullah, and H. Prasad, Low cost SnO2:P/SiO2/n-Si (textured) heterojunction solar cells, Journal of Physics D: Applied Physics, **26**, 959 (1993).

[29] D. Pyke, R. Reid R, and R. Tilley, Structures of tin oxide − antimony oxide catalysts, J Chem Soc Faraday I, **76**, 1174 (1980).

[30] A. Dodd, A. McKinley, M. Saunders, and T. Tsuzuki, Mechanochemical synthesis of nanocrystalline SnO2‐ZnO photocatalysts, Nanotechnology, **17**, 692 (2006).

[31] S. Ferrere, A. Zaban, and B. Gsegg, Dye sensitization of nanocrystalline tin oxide by perylene derivatives, J Phys Chem B, **101**, 4490 (1997).

[32] J. Song, D. Lee, Y. Kim, and Y. Kang, Preparation of water dispersed indium tin oxide sol solution, Mol. Cryst. Liq. Cryst., **444**, 247 (2006).

[33] D. Liu, S. Han, C. Li, T. Tang, W. Jin, X. Liu, B. Lei, and C. Zhou, Laser ablation synthesis and electron transport studies of tin oxide nanowires, Adv. Mater., **15,** 1754 (2003).

[34] S. Kalinin, J. Shin, S. Jesse, D. Geohegan, A. Baddorf, Y. Lilach, M. Moskovits, and A. Kolmakov, Electronic transport imaging in a multiwire SnO2 chemical fieldeffect transistor device, J. Appl. Phys., **98**, 044503 (2005).

[35] A. Maiti, J. Rodriguez, M. Law, P. Kung, J. McKinney, and P. Yang, SnO2 nanoribbons as NO2 sensors: insights from first principles calculations, Nano Lett., **3**, 1025 (2003).

[36] L. Fields, Y. Cheng, P. Xiong, and J. Zheng, Room-temperature low-power

hydrogen sensor based on a single tin dioxide nanobelt, Appl. Phys. Lett., **88**, 263102 (2006).

[37] Y. Cheng, C. Yun, R. Yang, J. Zheng, Z. Wang, G. Strouse, and P. Xiong, Mechanism and optimization of pH sensing with single SnO2 nanobelt, Nano Lett., **8**, 4179 (2008).

[38] C. Baratto, S. Todros, E. Comini, G. Faglia, M. Ferroni, G. Sberveglieri, G. Andreano, L. Cellai, A. Flamini, G. Marrazza, A. Nannini, G. Pennelli, and M. Piotto, SnO2 nanowire bio-transistor for electrical DNA sensing, in: IEEE SENSORS Conference, **2007**, 1132 (2007).

[39] Ü. Özgür, Y. I. Alivov, C. Liu, A. Teke, M. A. Reshchikov, S. Doğan, V. Avrutin, S. J. Cho, and H. Morkoçd, A comprehensive review of ZnO materials and devices, Journal of applied physics, **98** [4], 11 (2005).

[40] Y. Ryu, T. Lee, J. A. Lubguban, H. W. White, B. Kim, Next generation of oxide photonic devices: ZnO based ultraviolet light emitting diodes, Appl Phys Lett, **88**, 241108 (2006).

[41] M. Law, J. Goldberger, and P. Yang, Mater, Semiconductor nanowires and nanotubes, Annual Review of Materials Research, **34**, 83 (2004).

[42] J. Goldberger, D. J. Sirbuly, M. Law, and P. Yang, ZnO nanowire transistors, The Journal of Physical Chemistry B, **109** [1], 9 (2005).

[43] H. Kind, H. Yan, B. Messer, M. Law, and P. Yang, Nanowire Ultraviolet Photodetectors and Optical Switches, Advanced Materials, **14** [2], 158 (2002).

[44] M. Law, L. E. Greene, J. C. Johnson, R. Saykally, and P. Yang, Nanowire dye-

sensitized solar cells, Nature materials, **4** [6], 455 (2005).

[45] R. G. Breckenridge, and W. R. Hosler, Electrical properties of titanium dioxide semiconductors, Physical Review, **91** [4], 793 (1953).

[46] L. L. Kazmerski, Chemical, compositional, and electrical properties of semiconductor grain boundaries, Journal of Vacuum Science and Technology, **20** [3] 423 (1982).

[47] T. Gao, Q. Li, and T. Wang, Sonochemical synthesis, optical properties, and electrical properties of core/shell-type ZnO nanorod/CdS nanoparticle composites, Chemistry of materials, **17** [4], 887 (2005).

[48] F. Greuter, and G. Blatter, Electrical properties of grain boundaries in polycrystalline compound semiconductors, Semiconductor Science and Technology **5** [2], 111 (1990).

[49] J. Liu, X. Wang, Q. Peng, Y. Li, Preparation and gas sensing properties of vanadium oxide nanobelts coated with semiconductor oxides, Sensors and Actuators B: Chemical, **115** [1], 481 (2006).

[50] C. Nayral, E. Viala, V. Colliere, P. Fau, F. Senocq A. Maisonnat B. Chaudret, Synthesis and use of a novel SnO2 nanomaterial for gas sensing. Applied Surface Science, **164** [14], 219 (2000).

[51] E. Lind, High frequency III–V nanowire MOSFETs, Semiconductor Science and Technology, **31** [9], 093005 (2016).

[52] T. Chang, X. Zhang, X. Zhang, H. Cui, Accurate determination of dielectric permittivity of polymers from 75 GHz to 1.6 THz using both S-parameters and

transmission spectroscopy, Applied Optics **56** [12], 3287 (2017).

[53] L. Guo, X. Qin, and F. Zaera, Chemical Treatment of Low-k Dielectric Surfaces for Patterning of Thin Solid Films in Microelectronic Applications, ACS applied materials & interfaces, **8** [9], 6293 (2016).

[54] X. Hao, A review on the dielectric materials for high energy-storage application, Journal of Advanced Dielectrics, **3** [1], 1330001 (2013).

[55] S. V. Kalinin, J. Shin, S. Jesse, D. Geohegan, and A. P. Baddorf, Electronic transport imaging in a multiwire SnO2 chemical field-effect transistor device, Journal of Applied Physics **98** [4], 044503 (2005).

[56] Y. Ahn, J. Dunning, and J. Park, Scanning photocurrent imaging and electronic band studies in silicon nanowire field effect transistors, Nano Letters, **5** [7], 1367 (2005).

[57] A. Nehra, K. P. Singh, Current trends in nanomaterial embedded field effect transistor-based biosensor, Biosensors and Bioelectronics, **74**, 731 (2015).

[58] A. Zhang, C. M. Lieber, Nano-bioelectronics, Chemical Reviews, **116** [1], 215 (2016).

[59] L. Syedmoradi, A. Ahmadi, M. Norton, and K. Omidfar, A review on nanomaterial-based field effect transistor technology for biomarker detection, Microchimica Acta, **186** [11], 1 (2019).

[60] Y. Huang, X. Duan, Y. Cui, L. J. Lauhon, K. Kim, C. M. Lieber, Logic gates and computation from assembled nanowire building blocks, Science, **294** [5545], 1313 (2001).

[61] E. Comini, G. Faglia, and G. Sberveglieri, Stable and highly sensitive gas sensors based on semiconducting oxide nanobelts, Applied Physics Letters, **81** [10], 1869 (2002).

[62] C. Jin, and H. Jang, One-dimensional oxide nanostructures as gas-sensing materials: review and issues, Sensors, **10** [4], 4083 (2010).

[63] Y. Cheng, K. Chen, N. Meyer, J. Yuan, L. Hirst, P. B. Chase, and P. Xiong, Functionalized SnO2 nanobelt field-effect transistor sensors for label-free detection of cardiac troponin, Biosensors and Bioelectronics, **26** [11], 4538 (2011).

[64] P. Andrei, J. Zheng, L. Fields, Y. Cheng, and P. Xiong, Modeling and simulation of single nanobelt SnO2 gas sensors with FET structure, Sensors and Actuators B: Chemical **128,** [1], 226 (2007).

[65] E. Dattoli, Q. Wan, W. Guo, Y. Chen, X. Pan, and W. Lu, Fully transparent thin-film transistor devices based on SnO2 nanowires, Nano letters, **7** [8], 2463 (2007).

[66] Y. Cheng, R. Yang, J. Zheng, Z. Wang, P. Xiong, Characterizing individual SnO2 nanobelt field-effect transistors and their intrinsic responses to hydrogen and ambient gases, Materials Chemistry and Physics, **137** [1],372 (2012).

[67] H. Hoppe, T. Glatzel, M. Niggemann, A. Hinsch, M. C. Lux-Steiner, and N. S. Sariciftci, Kelvin probe force microscopy study on conjugated polymer/fullerene bulk heterojunction organic solar cells, Nano letters, **5**[2], 269 (2005).

[68] R. Dabirian, V. Palermo, A. Liscio, E. Schwartz, M. Otten, C. E. Finlayson, E. Treossi, R. H. Friend, G. Calestani, K. Mu¨llen, R. Nolte, A. E. Rowan, and P. Samorı, The relationship between nanoscale architecture and charge transport in conjugated

nanocrystals bridged by multichromophoric polymers, Journal of the American Chemical Society, **131** [20], 7055 (2009).

[69] S. Sadewasser, P. Jelinek, C. Fang, O. Custance, Y. Yamada, Y. Sugimoto, M. Abe, and S. Morita, New insights on atomic-resolution frequency-modulation Kelvin-probe force-microscopy imaging of semiconductors, Physical review letters, **103** [26], 266103 (2009).

[70] C. Barth, T. Hynninen, M. Bieletzki, C. R. Henry, A. S. Foster, F. Esch, and U. Heiz, AFM tip characterization by Kelvin probe force microscopy, New Journal of Physics, **12** [9], 093024 (2010).

[71] V. Guillaumin, P. Schmutz, and G. S. Frankel, Characterization of corrosion interfaces by the scanning Kelvin probe force microscopy technique, Journal of the electrochemical society, **148** [5], 163 (2001).

[72] Y. Martin, D. W. Abraham, and H. K. Wickramasinghe, High‐resolution capacitance measurement and potentiometry by force microscopy, Applied Physics Letters, **52** [13], 1103 (1988).

[73] C. C. Williams, J. Slinkman, W. P. Hough, and H. K. Wickramasinghe, Lateral dopant profiling with 200 nm resolution by scanning capacitance microscopy, Applied Physics Letters, **55** [16], 1662 (1989).

[74] D. J. Bayerl, and X. Wang, Three‐Dimensional Kelvin Probe Microscopy for Characterizing In‐Plane Piezoelectric Potential of Laterally Deflected ZnO Micro‐/Nanowires, Advanced Functional Materials, **22** [3], 652 (2012).

[75] A. Minj, A. Cros, T. Auzelle, J. Pernot, and B. Daudin, Direct assessment of p–n

junctions in single GaN nanowires by Kelvin probe force microscopy, Nanotechnology, **27** [38], 385202 (2016).

[76] M. Rao, and K. Ravindranadh, Insight into Nanotechnology and Applications of Nanomaterials, INTERNATIONAL JOURNAL OF ADVANCES IN PHARMACY, BIOLOGY AND CHEMISTRY, **2** [1], 2277 (2013).

[77] P. Girard, Electrostatic force microscopy: principles and some applications to semiconductors, Nanotechnology, **12** [4], 485 (2001).

[78] C. Coffey, and D. Ginger, Time-resolved electrostatic force microscopy of polymer solar cells, Nature materials **5**, 735 (2006).

[79] K. Lai, W. Kundhikanjana, H. Peng, Y. Cui, M. Kelly, and Z. Shen, Tapping mode microwave impedance microscopy, Review of scientific instruments, **80**, 043707 (2009).

[80] X. Wu, Z. Hao, D. Wu, L. Zheng, Z. Jiang, V. Ganesan, Y. Wang, and K. Lai, Quantitative measurements of nanoscale permittivity and conductivity using tuning-fork-based microwave impedance microscopy, Review of Scientific Instruments, **89**, 043704 (2018).

[81] K. Lai, H. Peng, W. Kundhikanjana, D. Schoen, C. Xie, S. Meister, Y. Cui, M. Kelly, and Z. Shen, Nanoscale electronic inhomogeneity in In2Se3 nanoribbons revealed by microwave impedance microscopy, Nano letters, **9**, 1265 (2009).

[82] L. Zhang, Y. Ju, A. Hosoi, and A. Fujimoto, Microwave atomic force microscopy: quantitative measurement and characterization of electrical properties on the nanometer scale, Applied Physics Express, **5**, 016602 (2011).

[83] Y. Ju, M. Hamada, T. Kobayashi, H. Soyama, A microwave probe nanostructure for atomic force microscopy, Microsystem technologies, **15**, 1195(2009).

[84] L. Zhang, Y. Ju, A. Hosoi, and A. Fujimoto, Microwave atomic force microscopy imaging for nanometer-scale electrical property characterization, Review of Scientific Instruments, **81**, 123708 (2010).

[85] B. Tong, M. Zhao, Y. Toku, Y. Morita, and Y. Ju, Local permittivity measurement of dielectric materials based on the non-contact force curve of microwave atomic force microscopy, Review of Scientific Instruments, **90**, 033706 (2019).

Chapter 2 Principle of M-AFM and Fabrication of M-AFM probe

Introduction

In this chapter, the principle of M-AFM and fabrication of M-AFM probe are introduced. M-AFM is a complex device which consists of microwave measurement system and atomic force microscopy. Firstly, the principle and working mode of the atomic force microscopy will be introduced. To transport the microwave and measure the reflected microwave signal, the microwave measurement system is also introduced. Then the fabrication process of M-AFM probes is described. Finally, the fabricated probes are evaluated by M-AFM system.

2.1 Principle of M-AFM

The microwave atomic force microscopy (M-AFM) combines the principles of the atomic force microscopy (AFM) and those of the microwave measurement method [1-3]. M-AFM keeps vibration at a constant distance from the evaluated material during measurement. By measuring the change of the resonance frequency of the M-AFM

probe, the topography and reflected microwave signal of the sample can be respectively evaluated with nanoscale resolution.

Fig. 2.1 shows the image of M-AFM probe during the measurement. Unlike other SPM techniques, the M-AFM probes have a special structure which can function as a parallel plate waveguide. The microwave transmits through the waveguide and is incident on the sample from the slit at the tip of the probe.

The unique structure of M-AFM probe provides a series of special advantages for this technique. First of all, the M-AFM result has high resolution based on AFM. Then the M-AFM works in a non-contact mode which won't cause damage to the sample. Finally, by utilizing the M-AFM probe, the electrical property evaluation can be realized on a nano-meter scale with high sensitivity.

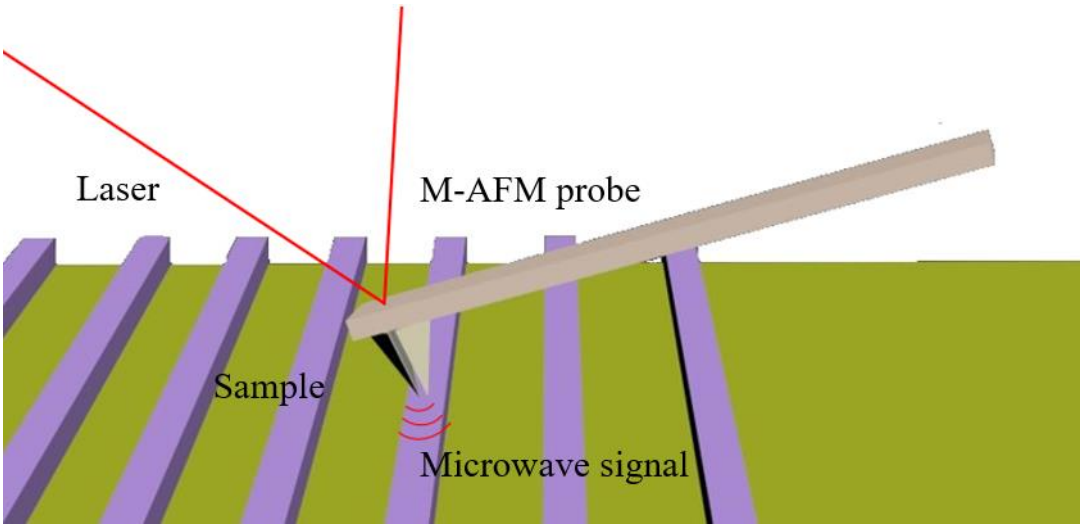

Fig. 2.1 M-AFM probe during measurement.

2.1.1 Working mode of M-AFM

M-AFM works in a frequency modulation (FM) mode that is a non-contact mode. In FM-AFM, the probe can evaluate the sample in a non-destructive and non-contact fashion with a nanometer scale spatial resolution.

In FM-AFM, a cantilever with resonant frequency f_0 and spring constant k is subject to controlled positive feedback such that it oscillates with constant amplitude A as shown in Fig. 2.2.

Firstly, the deflected signal transmits in a bandpass filter. Secondly, the signal is divided into three branches: the first one is a phase shift signal that enters an analog multiplier and then functions as a fed back signal; the oscillation amplitude and the gain input g are calculated by the second branch of signal; the last one is applied to feed the frequency detector.

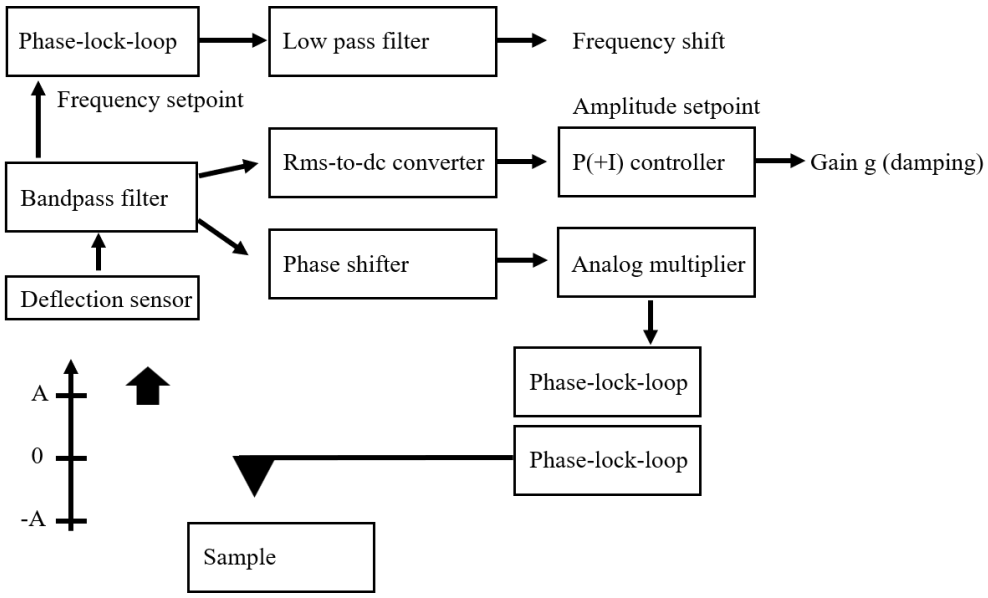

Fig. 2.2 The working principle of the FM-AFM [4].

When force between tip and sample is applied, the vibration frequency of the cantilever f is given by $f = f_0 + \Delta f$. Where, f_0 is the resonant frequency of the probe and Δf is the change of the frequency during measurement.

The resonant frequency of a harmonic oscillator can be represented as $\left(\frac{k^*}{m^*}\right)^{\frac{1}{2}}/(2\pi)$, where k^* is the effective spring constant and m is the effective mass. If the second derivation of the tip-sample potential $k_{ts} = (\partial^2 V_{ts})/(\partial z^2)$ is constant for the whole range covered by the oscillating cantilever, $k = k_{ts} + k_0$. If $k_{ts} << k$, the square root can be expanded as a Taylor series and the shift in eigenfrequency is approximately given by:

$$\Delta f = \frac{k_{ts}}{2k} f_0 \qquad (2.1)$$

By measuring Δf, the change of the force between tip and sample can be obtained.

The oscillator circuit plays a significant role in the system. In order to understand the working principle of FM-AFM, it is necessary to discuss the cantilever motion. The cantilever of the probe can be considered as a damped harmonic oscillator with an piezoelectrical signal. For sinusoidal driven signals $A_{drive}e^{i2\pi f_{drive}t}$ and a quality factor Q>>1, the oscillation amplitude of the cantilever *A* can be represented by the equation below:

$$\frac{A}{A_{drive}} = \frac{1}{1-\frac{f_{drive}^2}{f_0^2}+if_{drive}/(f_0Q)} \tag{2.2}$$

where A_{drive} and f_{drive} are the amplitude and frequency of the driving signal. The absolute value of the amplitude $|A|$ is given by

$$|A| = \frac{|A_{drive}|}{\sqrt{\left(1-\frac{f_{drive}^2}{f_0^2}\right)+f_{drive}^2/(f_0^2Q^2)}} \tag{2.3}$$

And the phase shift between the driving and resulting signals φ is

$$\varphi = \arctan\left[\frac{f_{drive}}{Qf_0(1-f_{drive}^2/f_0^2)}\right] \tag{2.4}$$

In here, the Q is the Q factor which is a property to indicate how underdamped an oscillator is. When it is a closed feedback loop, the driving frequency can be calculated by f_0, the phase shift φ, and the force between tip and sample. By applying the

oscillator system in Fig. 2.2, controlled positive feedback on the probe vibration at a constant amplitude can be obtained.

In Fig. 2.2, the gain g is a resulting signal. g is enhanced by multiplying with a phase shifted cantilever deflection signal q''. The oscillation amplitude of the cantilever is set at its minimum value by adjusting the phase shifter and the driving signal.

During the measurement of FM-AFM, it is significant to discuss the motion of the cantilever that is considered as a weakly disturbed harmonic oscillator with an amplitude A at a distance $q(t)$ to a sample. The minimum distance between tip and sample is $q = d$ and $q(t) = q'(t) + d + A$.

The Hamiltonian of the cantilever is:

$$H = \frac{p^2}{2m^*} + \frac{kq'^2}{2} + V_{ts}(q) \qquad (2.5)$$

Where k is the spring constant, and m^* is the effective mass. And $m^* V_{ts} = \frac{m^* dq'}{dt}$. The unperturbed motion is given by:

$$q'(t) = A\cos(2\pi f_0 t) \qquad (2.6)$$

Next, it is significant to understand the change of resonance frequency under the influence of external force during the vibration of the cantilever. The resonance frequency of the cantilever without external force can be represented as the equation

below:

$$f_0 = \frac{1}{2\pi}\sqrt{\frac{k}{m^*}} \tag{2.8}$$

If the change of the interatomic force between the tip and the sample $k_{ts} = -\frac{\partial F_{ts}}{\partial z}$ is constant during the vibration, the change of the frequency can be represented as below:

$$\Delta f = f_0 \frac{k_{ts}}{2k} \tag{2.9}$$

Thus, if k_{ts} can be obtained by measuring Δf, the non-contact measurement method can be realized.

In the FM-AFM, the cantilever keeps vibrating at a frequency moderately higher than the resonance frequency. The amplitude of the vibration is several nanometers. When the tip and of the probe is influenced by the external long-range forces such as Van der Waals force, the vibrating frequency will decrease. When FM-AFM is scanning above a sample, the force between the tip and sample will change due to the variation in the distance caused by the uneven sample surface. The vibration frequency keeps at a constant value by the feedback loop system during the measurement. When the system detects a decrease in frequency, it immediately adjusts the distance between the tip and sample. Thus, the topographic image of the sample surface can be obtained. But regarding the M-AFM, there is a parallel plate waveguide inside the cantilever of M-AFM probe, which means it is necessary to discuss the influence of the cantilever's

vibration on the microwave transmission. When M-AFM is scanning the sample, the resonance frequency of the cantilever is around 150 kHz and the frequency of the microwave is 94 GHz. As the frequency of the microwave is much higher than that of cantilever, the microwave signal can be considered as a constant value on each measuring point. And thus, the influence of the cantilever's vibration on the microwave signal is negligible.

2.1.2 Experimental setup of M-AFM

In Fig. 2.3, the experimental setup of M-AFM was schematically illustrated [6]. In this system, the microwave is generated by an analog signal generator with a frequency of 16.66 GHz. Then, a six-time frequency multiplier is applied to increase the frequency to 94 GHz. The microwave signal was transmitted into a magic tee and was divided into two branches. One was transmitted to the probe to sense the sample and receive the reflected signal while the slit on the tip emitted microwave onto the sample surface. The other one was sent to the attenuator and the tunable-short as a reference microwave signal with a constant phase difference comparing with the signal reflected from the sample. By adjusting the attenuator and the tunable-short, the reference signal was set at a given value by adjusting the output voltage of the detector, while the distance between M-AFM probe and sample is long (about 1cm). Finally, a detector that measured the reference signal and microwave signal from the M-AFM probe was connected to the magic tee and was used to indicate the voltage converted from the

reflected microwave signals.

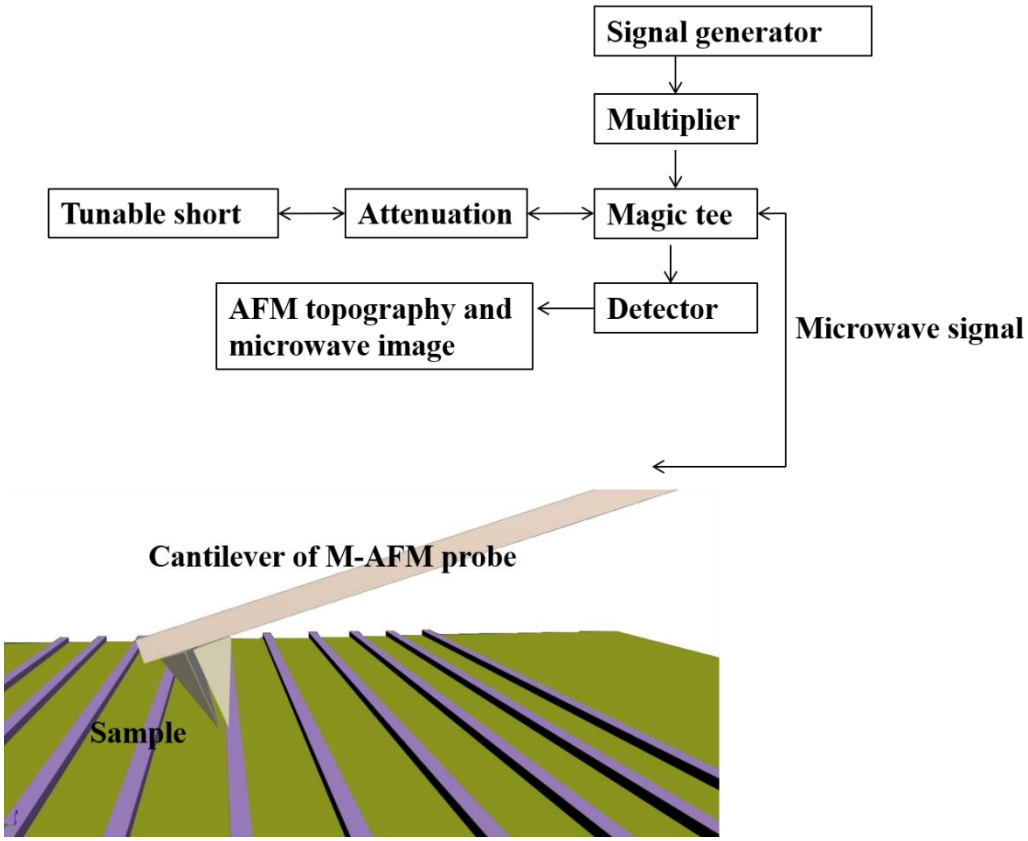

Fig. 2. 3 The microwave system of M-AFM [6].

2.2 Fabrication of M-AFM probe

Before the fabrication of the M-AFM probe, the size of the probe should be determined. In the previous researches, the measurement methods of conductivity and relative permittivity based on M-AFM are established by using bulk materials. In this study, the target samples are one-dimensional nanomaterials with width and thickness that are at least 100 nm. In order to evaluate the nanomaterials by M-AFM, the

dimension of the fabricated M-AFM probe in this study is less than 100 nm.

To determine the size of the probe, the spring constant that strongly influences the eigenfrequency of the cantilever must be determined at first. Meanwhile the parameter of electrical impedance which represents the characteristic of the transmission line of microwave is also significant that should be taken into consideration. To measure the topography with high resolution, the value of spring constant of the AFM cantilever should be high. The eigenfrequency will receive less influence from the noise during measurement when the sample is soft and small. Also, in order to detect microwave signal with high sensitivity, it is necessary to prevent reflection and attenuation of microwave as much as possible in the transmission line. Therefore, considering the connection with the external microwave source, the characteristic impedance of the transmission line is designed as 50 Ω. By considering these problems, the size of the probe can be determined as shown in Table 2.1. In Table 2.1, the size and substrate material of the probes are illustrated, the spring constant and the eigenfrequency of the cantilever, as well as the characteristic impedance can be calculated.

Table 2.1. Size of M-AFM probes.

Parameter		Value
Dimension of cantilever, [μm]	Width, a	42
	Length, l	250
	Thickness, d	15
Spring constant, k [N/m]		182.6
Resonance frequency, f_0 [kHz]		151.4
Characteristic impedance, Z_c [Ω]		51.8

As a material of the M-AFM probe, it is necessary to select a material that can function as the AFM probe and can also transmit the microwave. As depicted in the former content, the gallium arsenide (GaAs) which is a group III-V compound semiconductor having excellent insulation properties is used as a probe substrate [7]. The probe substrate was a single crystal gallium arsenide wafer of 2 inches in plane orientation (100), thickness 350 μm, double-sided mirror finished, non-doped. In addition, Au, which has good electrical conductivity and is chemically stable, was used for the conductor plate of the parallel plate line serving as a waveguide. To fabricate the probes, microelectromechanical system technology such as photolithography and wet etching was applied.

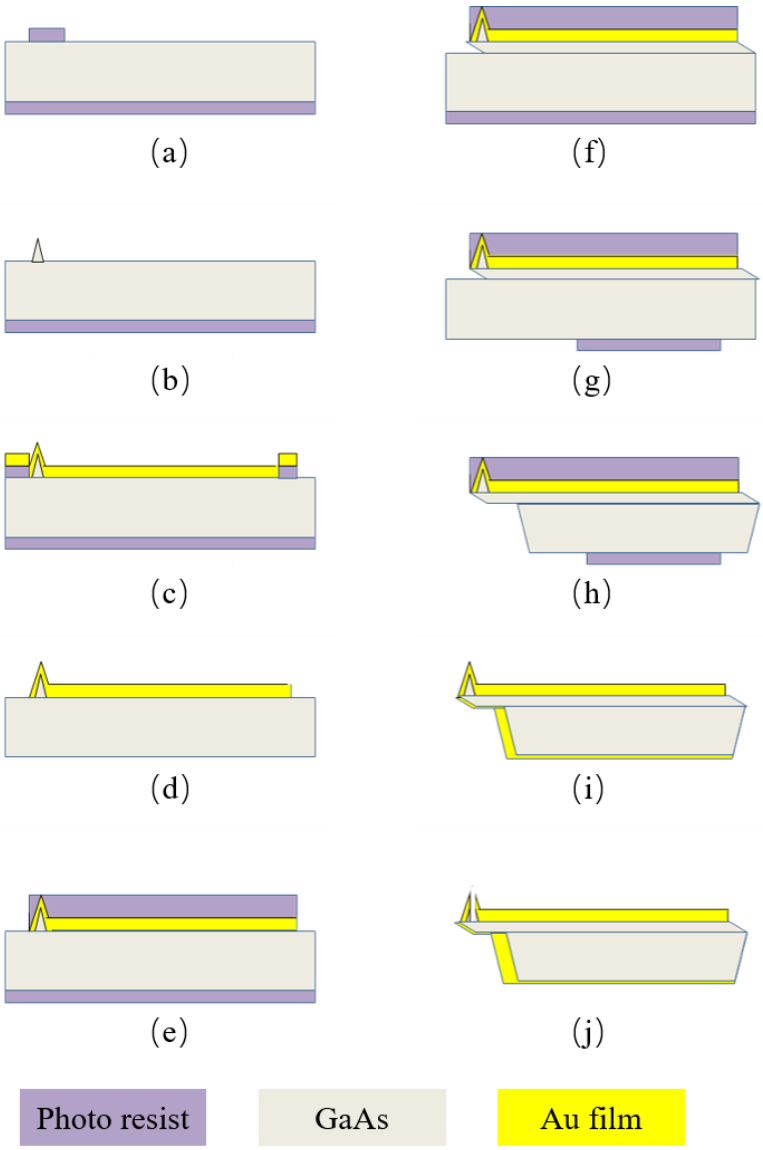

Fig. 2.4 Fabrication process of the M-AFM probe.

Photolithography mainly consists of three steps: photoresist application, exposure and development. The photoresist which is composed of resin, photosensitizer and organic solvent is applied to the wafer substrate. Ultraviolet rays will be irradiated through a patterned mask through a double-sided mask aligner to transfer the pattern to the resist resin. Unnecessary portions of the resist are dissolved by the developing solution. Pattern on the wafer is fabricated by the steps above. In addition, when

applying the resist to the wafer surface, a spin coating method was used to control the film thickness of the resist by the rotation speed of the spin coater. In the spin coating method, an arbitrary film thickness can be obtained by the following steps. First the wafer would be placed on a spinner. Then the spinner will fix the wafer by creating vacuum place under the wafer. By dropping photoresist on the wafer and rotating the spinner at a high speed, the excessive photoresist will be blown away. The film thickness also depends on the viscosity of the resist in addition to the rotation speed of the spinner.

Wet etching is a processing method in which material is removed mainly by chemical reaction with chemical liquid. In order to fabricate a probe, the crystal which has different chemical characteristic on different crystal planes is applied in the chemical etching [8]. In this method, the etching rate by wet etching varies greatly on different crystal planes. Meanwhile when the pattern on the wafer is fabricated by lithography, the etching rates of the crystal planes parallel to each side of the mask pattern are different form each other. The etching side surface obtained at this time is the one which has the least etching rate. Therefore, the etched sides have different etching speed depending on the direction of the pattern. Thus, the structure of the probe is fabricated. When fabricate the pattern with resist by photolithography, it is necessary to consider the crystal planes. In addition, gallium arsenide which is a compound semiconductor has a sphalerite structure. It is different from the crystal structure of silicon which is a diamond structure. So, the wet etching in the gallium arsenide is complicated than that of silicon and it is difficult to anticipate the etching result [9,10]. Furthermore, in the

wet etching, the back side of the wafer will be etched with the etching solution. So that the side etching progresses. In order to using the wet etching, it is necessary to prepare an etching mask to make an appropriate pattern during lithography so that the desired shape will be formed.

The fabrication processes of the probe are listed below. Fig. 2.4 illustrate the fabrication process.

(a) Patterning the etching mask for the tip.

(b) Fabricating the tip.

(c) Patterning the photoresist mask for the waveguide and coating Au film.

(d) Removing the photoresist and coating Au film.

(e) Patterning the etching mask for the cantilever.

(f) Wet etching to fabricate the wave guide of the M-AFM probe.

(g) Forming the etching mask for fabrication of the support part of the probe.

(h) Fabricating the support part of the probe by wet etching.

(i) Fabricating the Au film on the back side of the probe.

(j) Fabricating the nanoslit on the surface of the tip by focus ion beam.

To make the pattern on the wafer in photolithography, 3 kinds of photo resist are applied depending on the demand of manufacturing process. In order to fabricate the tip with high accuracy in micrometer order, FPPR-P-30 is applied. When fabricate the waveguide of the probe, the FNPR-L3 is used since it can fabricate an overhang structure pattern. When fabricate the cantilever and support of the probe, it is necessary to protect the tip of the probe. Thus FPPR-HW600A which has high viscosity and high

film thickness is applied.

During wet etching the structure of the probe is formed. And depending on the demand of the manufacture process, two kinds of the etching solution are applied. When fabricate the tip of the probe, the solution consist of H_3PO_4-H_2O_2-H_2O is applied since it has low etching rate. When fabricating the cantilever as well as the support of the probe, the solution consist of H_2SO_4-H_2O_2-H_2O is applied because it has a relatively high etching rate.

2.2.1 Fabrication of the tip

In order to form the tip of the probe by wet etching, first the photolithography is applied to fabricate a pattern on the wafer. There are two kinds of etching: dry etching and wet etching. Using the liquid chemicals, wet etching is widely applied as a material removal method. Before the wet etching, the pattern is fabricated on the sample by photolithography. The materials that are not covered by photoresist are removed by the chemical. The wet etching process generally contains a series of chemical reactions among the chemical enchants, the material and the byproducts. The wet etch process consists of the following parts. Firstly, the liquid etchant spread and move the target material that needs to be processed. Secondly, the chemical reactions occur between the etchant and the material. Finally, the byproducts are generated and diffuse away from the reacted material. In dry etching, plasmas or etchant gasses remove the substrate material. The reaction that takes place can be done utilizing high kinetic

energy of particle beams, chemical reaction or a combination of both. But the price of the dry etching is high and the etching rate of the dry etching is slow. In this part, the wet etching is applied since it doesn't demand complicated experimental devices. To fabricate the structure of the tip of the probe, the side etching is applied. To fabricate the cantilever and the support of the probe, the wet etching is applied.

To make a pattern for wet etching with micro-order accuracy, FPPR-P-30 is applied for its high etching resistance. In this research, the shape of the pattern is a square. Each side of the square is 18 micrometers. In Table 2.2, the condition of lithography to fabricate the tip is listed.

Table 2.2 Photolithography condition of fabrication of the tip

Resist		FPPR-P-30
Rotation speed, [rpm]		1500
Rotation time, [sec]		15
Prebake	Temperature, [℃]	100
	Time, [min]	10
Exposure, [mJ/㎠]		175
Developer		NMD-3
Developing time, [sec]		60
Postbake	Temperature, [℃]	145
	Time, [min]	20
Thickness of resist, [μm]		3

After the fabrication of the pattern by the lithography, the wet etching is applied and the tip will be fabricated in this step. The side etching is applied during the wet etching. With the process of the wet etching, the shape of the tip will be formed gradually. When the gallium arsenide around the pattern is removed and the pattern drops from its position. The tips are fabricated perfectly. Since the tip is significant for the measurement and it will affect the resolution of the experimental result. The etching rate should be slow when fabricate the tip. Thus, the etching solution should be chosen carefully. In this research, the solution which consists of phosphoric acid is applied. It should be mentioned that if the ratio of phosphoric acid increases, the tip of the will be sharper. Thus, the phosphoric acid to hydrogen peroxide ratio is 10 to 1 [9]. Meanwhile if the temperature of the solution is high, the shape of the tip will be blunt. So, the ice should be put around the reaction vessel to cool down the temperature of the solution. The condition of wet etching is listed in Table 2.3. After etching, the excessive resist will be removed with the acetone and cleaned by ultrasonic wave. The fabricated probe tip is displayed in Fig.2.5.

Table 2.3 Wet etching condition of fabrication of the tip

Etching time	Temperature, [℃]	Etching time, [min]
H_3PO_4:H_2O_2:H_2O=10:1:1	2	125

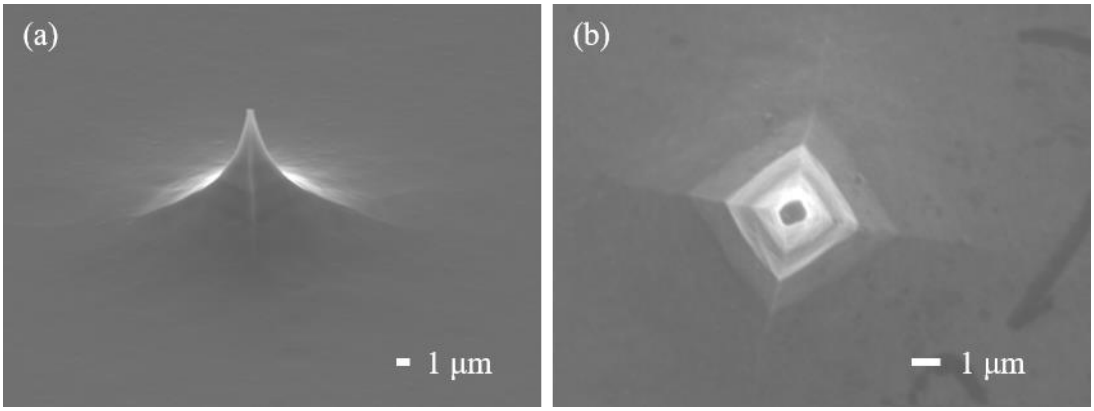

Fig. 2.5 The tip of M-AFM probe observed by SEM.

2.2.2 Fabrication of the cantilever

To fabricate the cantilever of the probe, first the waveguide of the probe will be fabricated. When coating the Au film to fabricate the waveguide by electron beam physical vapor deposition (EBPVD), pattern will be made on the wafer by lithography with photo resist. The photo resist is shown in Table 2.4. Before coating the photo resist on the wafer, the FAP is applied to increase the stickiness of the photo resist. After the fabrication of the pattern, the exposure is applied. In Table 2.4, the conditions of the lithography are listed. After fabrication of the pattern, electron beams vapor method is applied to coating the Au film on the wafer. Then the excessive Au film will be removed by clean the wafer in the acetone with ultrasonic wave. The condition for the film formation is listed as follows.

Table 2.4 Photo resist condition before EBPVD

HMDS		FAP
Rotation speed, [rpm]		1000
Rotation time, [sec]		20
Prebake	Temperature, [℃]	100
	Time, [min]	1

Meanwhile, Table 2.5 shows the EBPVD condition of coating on the probe. After coating the Au film, the excessive photo resist will be cleaned. Finally, the Au film will be formed on the probe.

Table 2.5 EBPVD condition of coating on the probe

Instrument	EBX-10D
Target	Au
Pressure, [Pa]	$2*10^{-3}$
Substrate temperature, [℃]	Room
Evaporation rate, [A/sec]	2
Evaporation time, [min]	8
Emission current, [mA]	100

In Fig. 2.6, the photo resist used to fabricate the overhang structure is illustrated with schematic diagram. After the fabrication of the Au film, the structure of the cantilever

will be fabricated. The process of making the cantilever is similar with that of tip fabrication which applied photolithography and wet etching. First the pattern is fabricated by lithography in Table 2.6. In order to protect the tip during wet etching in the latter process, the FPPR-HW600A is applied. The film thickness of this resist is 14 micrometer and it has high viscosity. The condition of lithography is listed in the Table 2.6.

Table 2.6 Photolithography condition of fabrication of the cantilever

Resist		FPPR-HW600A
Rotation speed, [rpm]		1000
Rotation time, [sec]		20
Prebake	Temperature, [℃]	110
	Time, [min]	15
Exposure, [mJ/㎠]		450
Developer		TMAH
Developing time, [sec]		180
Postbake	Temperature, [℃]	145
	Time, [min]	20
Thickness of resist, [μm]		14

The solution for wet etching is consisted of H_2SO_4, H_2O_2 and H_2O. Since the consistence of the H_2O_2 is high in this solution [11,12], the surface reaction rate on each crystal plane is different in Table 2.7. Unlike the process of tip fabrication, here the anisotropy etching is applied. In the solution, the ratio of H_2O_2: H_2SO_4: H_2O is 8:1:1. In such solution, the wet etching is anisotropy etching [13].

In this step, the pattern of the resist is parallel to the (011) crystal direction. When applied the mixed solution which is consisted of H_2SO_4, H_2O_2 and H_2O, on the side surface, a 45-degree inclined plane is formed and two inclined surface which parallel to (111) and (111) crystal plane is fabricated [14]. It is known that when the pattern is arranged in the direction rotated by 90 degrees in the (011) direction, the surfaces on the (111) and (111) direction are inverted mesa type and have an inclination of 60 to 75 degrees appear on the side. Therefore, in the latter step, the Au film on the back side can easily connect with the one on the surface of the probe and form the waveguide. The fabricated cantilever is illustrated in Fig. 2. 6.

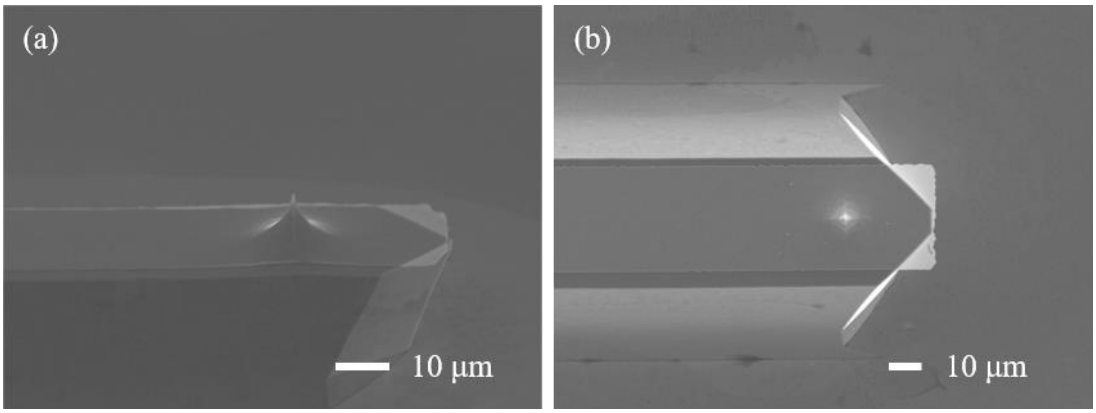

Fig. 2.6 The cantilever observed by SEM.

Table 2.7 wet etching condition of fabrication of the cantilever

Etching time	Temperature, [℃]	Etching time, [min]
H_2SO_4:H_2O_2:H_2O=1:8:1	2	8.5

2.2.3 Fabrication of the Support part of the Probe

The fabrication of the support of the probe is similar with that of the fabrication of the cantilever. This step also applied the photolithography and wet etching. When fabricating the support part of the cantilever, the wafer will be etched from the back surface.

Firstly, photolithograph is applied and pattern is fabricated on the back surface of the wafer. To fabricate the support part of the probe, FPPR-HW600A is applied as the photoresist which is the same as the one applied in cantilever fabrication. The condition for lithography is listed in Table 2.8. To make it difficult for Au film formation at both sides of the support part, pattern was formed and the support part of the probe becomes a mesa structure after wet etching on the back surface.

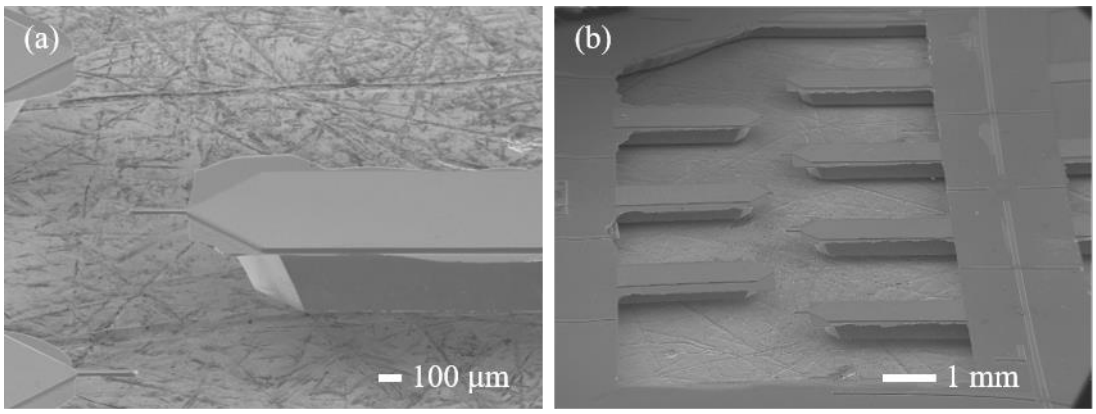

Fig. 2.7 The support observed by SEM.

Table 2.8 Wet etching condition of fabrication of the holder

Etching time	Temperature, [℃]	Etching time, [min]
H_2SO_4:H_2O_2:H_2O=1:8:1	2	140

After lithography, the etching solution consisted of H_2SO_4-H_2O_2-H_2O is applied for wet etching. The etching will start from the back surface of the wafer. The etching will be stopped when the cantilever of the wafer can be seen from the back surface of the wafer. In this step the time for etching coast much longer than that of the former steps since much more gallium arsenide on the wafer will be removed in this step. Thus, in this step, the etching is not uniformed easily and the cantilevers often disappears. In order to protect the cantilevers, the wafer was cut into quarters an etched so as to reduce the rate of disappearance of the cantilever caused by the excessive etching. In Table 2.8, the condition for fabricating the support is listed. The support part of the probe is illustrated in Fig. 2. 7.

2.2.4 Fabrication of the Au Film on the Backside of the Probe

After the fabrication of the support part, Au film is formed on the back surface of the probe and connects with the Au film on the probe surface at the end of the cantilever. EBPVD method same with that applied in cantilever fabrication is applied.

In the film formation, it is ideal that the parallel plate line is not short-circuited on the side face of the support part or the cantilever. And Au film on the top surface of the probe should be connected with that on the back surface at the terminal end position. Film forming condition by EB evaporation is listed in Table 2.5. In order to confirm whether the metal film on both sides of the probe is short-circuited, it was confirmed by the digital multimeter.

2.2.5 Focus ion Beam Processing

The waveguide was connected by depositing Au film on both surface of the probe. However, until this step, the waveguide is short-circuited, no potential difference occurs on both surface of the probe and the transmission of microwave is impossible. Therefore, a parallel plate line was constructed on the probe and a slit was processed by focused ion beam (FIB) processing that emits and detects the microwave at the probe tip. The slit traversed the waveguide so as to separate the metal film on the tip. As a result, a parallel plate waveguide is constructed in Fig. 2.8. The tip becomes the end of

the microwave waveguide. And the emission of microwave from the slit approachs maximum. In this research, a scanning ion microscope SMI 2050 manufactured by SEIKO EG&G was used. The condition for FIB processing is listed in Table 2.9. And the slit on the M-AFM probe is illustrated in Fig. 2.8.

Table 2.9 FIB condition

Instrument	SII SMI2050
Beam Condition	U.Fine
Depth, [μm]	0.2
Wide, [μm]	0.1

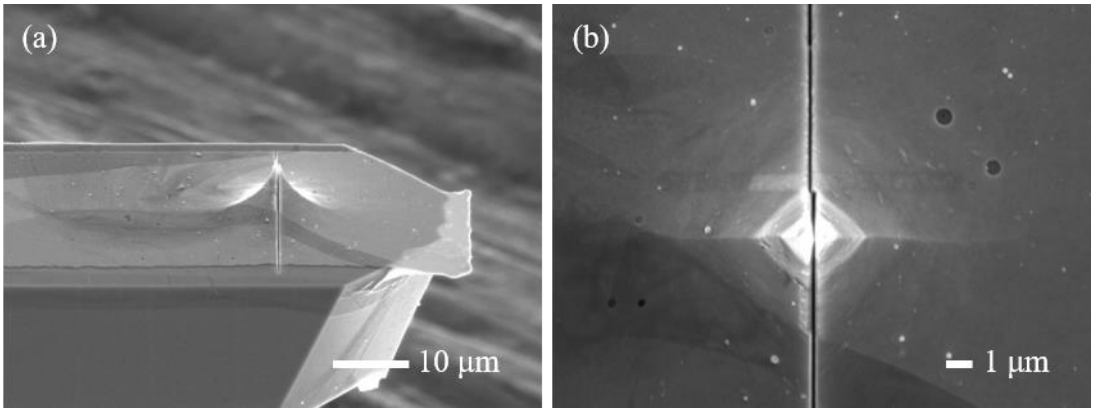

Fig. 2.8 Nanoslit on the tip observed by SEM.

2.3 Evaluation of the M-AFM Probes

2.3.1 Sample to Evaluate the Probe

To confirm whether the fabricated M-AFM probe can evaluate the topography and microwave image, measurement based on M-AFM was carried out. For confirmation of the waveguide, a thin metal lines sample was used. This metal thin wire specimen is made by depositing Au on a gallium arsenide substrate. The height of each line is 150 nm. A SEM image of the sample is shown in Fig. 2.9. As the measurement condition of the M-AFM, the measurement mode was non-contact mode, the measurement range was 12μm * 7μm. The scanning speed was 1 μm/s. The frequency of microwave was 94 GHz, and the microwave amplitude was 10 dbm.

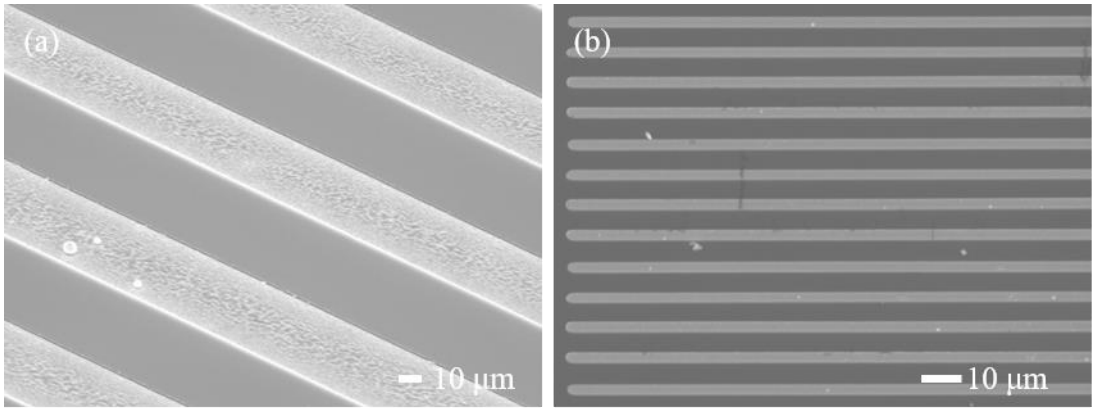

Fig. 2.9 The sample to evaluate the M-AFM probe.

2.3.2 Experiment to Evaluate the M-AFM Probe

To evaluate the fabricated waveguide of the probes, the experiment which applying the fabricated probes is arranged. The microwave is conducted by the probe, and a sample consisted of GaAs substrate and Au film is fabricated in this experiment. The detailed information on the surface is analyzed in Fig. 2.10 (a). In the Fig. 2.10 (b), the microwave image of the sample is scanned. The height difference between Au film and Si substrate is 120 nm in Fig 2.10 (a). Marked with black arrow in Fig. 2.10 (a), the lateral resolution of the M-AFM probe is 91 nm. In Fig. 2.10 (b), the lateral resolution of the M-AFM probe in microwave image is 46 nm. There is a difference in the lateral resolution between the topography and microwave image because the lateral resolution of the topography is determined by the sizes of the slit and tip of the probe, while the resolution of the microwave image only depends on the size of the slit on the tip. Since the shortest distance between two points on a sample that can be distinguished as different entities is lateral resolution of the M-AFM probe, the measured resolution indicated that the fabricated M-AFM probe can distinguish a nanomaterial that is larger than 91 nm. Thus, the fabricated probes are available to evaluate the nanowires in this study. In the previous stages, the multimeter is applied to confirm the insulation statement of each probe. The scanning region of the M-AFM is 12×7 micrometer, the scanning speed was 2 micrometer per second, the microwave frequency was 94 GHz, and the microwave amplitude was 10 dBm. According to the microwave image, the change of the reflected microwave signal is detected. Also, from (b) which illustrates

the reflection difference on the sample surface, it can be seen that the change distribution of the response of the microwave is obtained. The difference of the reflected microwave signal is 2.1 mV. This image is obtained due to a change in the microwave signal which is influenced by the electrical properties of material surface. The change distribution of the microwave also corresponds to the change of the part of the material of the sample. From these facts, it was found that the produced M-AFM probe can release and detect microwaves. There is a relationship between the reflection coefficient of microwave, conductivity, and relative permittivity, and the reflection coefficient of microwave obtained from the different aspects of these electrical characteristics changes. In this experiment, since a detector that outputs a voltage proportional to the square of the reflection coefficient of the microwave is used, the voltage distribution of the microwave image should reflect the change distribution of the conductivity of the material surface.

From the measurement result of the microwave image, since clear difference between GaAs and thin metal film can be confirmed, it can be seen that the microwave is guided inside the fabricated probe.

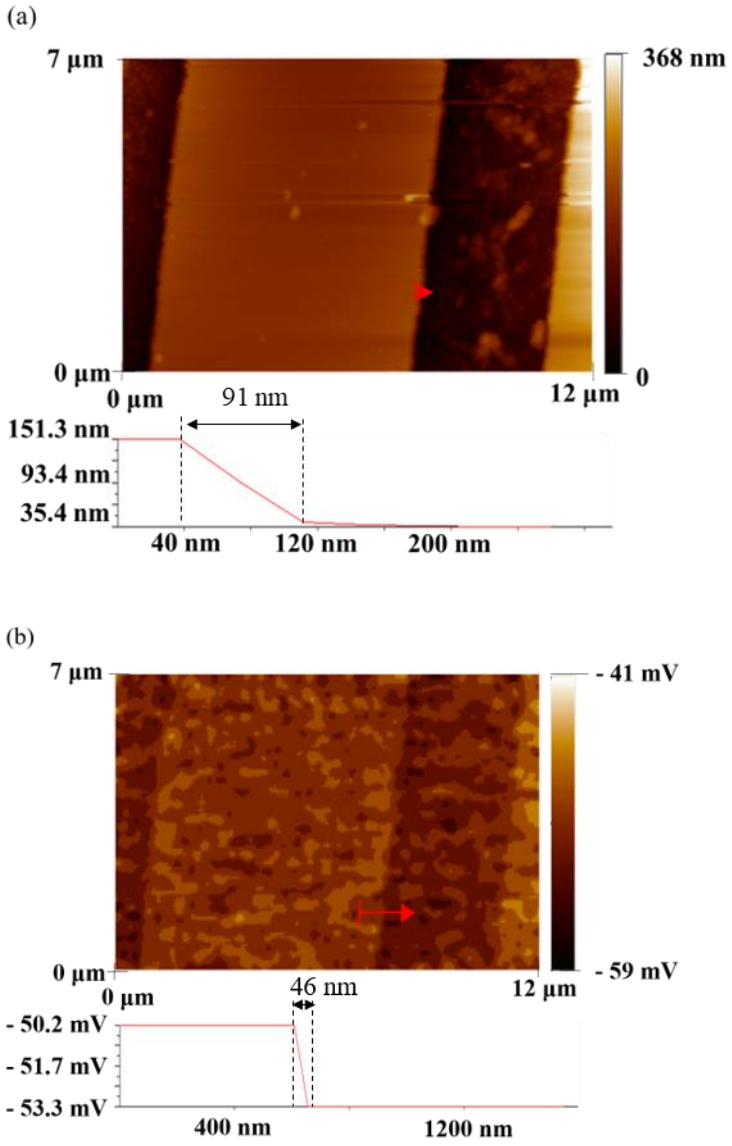

Fig. 2.10 The topography and microwave image measured by M-AFM with the fabricated probe.

2.4 Summary

In this chapter, the mechanisms of the AFM and the microwave system are described. The waveguide which is used to transport the microwave is constructed

based on the AFM probe. The semiconductor material, gallium arsenide, is chosen as the substrate of the probe. Consider that the spring constant of the cantilever should be small and the characteristic impedance of the parallel plate waveguide should be 50 Ω, the size of the probe is designed. The basic structure of the probe mainly applied the micro electron mechanical system such as photolithography and wet etching. The waveguide on the probe is coat by the EBPVD. After the FIB processing, a nanoslit is induced across the tip of M-AFM probe. Finally, the M-AFM probes are evaluated. The main results in this chapter are summarized as below:

(1) The tip of the fabricated probe is scanned by the scanning electron microscope. The height of the tips is about 7 micrometers. And the curvature radius is about 30 nm.

(2) The cantilever and the support part of the probe are also fabricated by the micro electron mechanical system. The experimental results are scanned by the scanning electron microscope. The waveguide coating on the probe is fabricated. By using the multimeter, it is confirmed that the waveguide is short circuit.

(3) A slit is induced on the probe, by utilizing the FIB processing. After the FIB processing, the probe is tested by the multimeter and it is confirmed that the waveguide is separated and insulated.

(4) The sample consisted of Au film and GaAs substrate is used to evaluate the probes. The topography and microwave images are scanned by the probes. Meanwhile the reflection change on the sample surface is detected on the nanoscale. According to the evaluated result, the resolution of the M-AFM probe is about 100 nm which

is extremely high compared with other scanning probe technique for electrical property evaluations. From the measurement result of the microwave image, clear difference between GaAs and thin metal film can be confirmed. These evaluated results suggest that the fabricated M-AFM probes have high performance.

Reference

[1] Y. Ju, T. Kobayashi, and H. Soyama, Development of a nanostructural microwave probe based on GaAs, Microsystem Technologies, **14**, 1021 (2008).

[2] L. Zhang, Y. Ju, A. Hosoi, and A. Fujimoto, Microwave atomic force microscopy imaging for nanometer-scale electrical property characterization., Review of Scientific Instruments, **81**, 123708 (2010).

[3] L. Zhang, Y. Song, A. Hosoi, Y. Morita, Y. Ju, Microwave atomic force microscope: MG63 osteoblast-like cells analysis on nanometer scale, Microsystem Technologies, **22,** 603 (2016).

[4] F. Giessibl, Advances in atomic force microscopy, Reviews of modern physics, **75**, 949 (2003).

[5] D. M. Pozar, Microwave engineering, John Wiley & Sons, 32 (2009).

[6] A. Fujimoto, L. Zhang, A. Hosoi, Y. Ju, Structure modification of M-AFM probe for the measurement of local conductivity. Microsystem technologies, **17**, 715 (2011).

[7] 赤崎 勇, III-V 族化合物半導体, pp. 148-151, 初版, 培風館

[8] 近藤 英一, 機械・材料系のためのマイクロ・ナノ加工の原理, pp. 131-139, 157-175, 初版, 共立出版

[8] 生駒 俊明, 河東 田隆, 長谷川 文夫, ガリウムヒ素, pp. 185-191, 初版, 丸善株式会社

[9] Y. Mori, and N. Watanabe, A new etching solution system, H_3PO_4-H_2O_2-H_2O, for GaAs and Its Kinetics, Journal of Electrochemical Society, **125**, 9 (1978)

[10] D. N. MacFadyen, On the preferential etching of GaAs by H_2SO_4-H_2O_2-H_2O,

Journal of Electrochemical Society, **130**, 9 (1983)

[11] Shinya lida and Kazuhiro Ito, Selective etching of gallium arsenide crystals in H_2SO_4-H_2O_2-H_2O system, Journal of Electrochemical Society, **118**, 768 (1971)

[12] 佐藤 洋行, 東北大学ナノメカニクス専攻, ガリウム砒素マイクロ波導波プローブの開発に関する研究, 東北大学修士論文 (2004)

[13] T. Ohnishi, T. Miyamoto, N. Tanifuji, Y. Matsuda, M. Minami, M. Motoki, S. Hirose, and S. Yamada, Micro-Fabrication of a prototype hybrid GaAs/Ceramics cantilever for SPM applications, Sensors and Actuators A, **137**, 34 (2007)

[14] K. Yamaguchi, and S. Tada, Fabrication of GaAs microtips for scanning tunneling microscopy by wet etching, Journal of Electrochemical Society, **143**, 8 (1996).

[15] X. Wu, Z. Hao, D. Wu, L. Zheng, Z. Jiang, V. Ganesan, Y. Wang, and K. Lai, Quantitative measurements of nanoscale permittivity and conductivity using tuning-fork-based microwave impedance microscopy, Review of Scientific Instruments, **89**, 043704 (2018).

Chapter 3 Quantitative Evaluation of Local Permittivity of Metal Oxide Nanomaterials Using Microwave Atomic Force Microscopy

3.1 Introduction

The metal oxide semiconductors such as zinc oxide [1], copper oxide [2] and tin oxide [3] are very common and variety dielectric materials among a series of different semiconductors. In the past years, a series of different methods including thermal oxidation [4], solution-phase growth [5], and template-assisted synthesis [6] have been utilized to fabricate various one-dimensional semiconductor nanomaterials. Owe to the high surface-volume ratio property, the semiconductor nanomaterials have improved physical and electronic properties [7, 8] which have been applied to a large number of electronic devices such as solar cells [9,10], photodetectors [11] and gas sensors [12,13]. For such dielectric insulator materials, permittivity is a meaningful electric property parameter since the dielectric materials with low permittivities are desirable for high-speed integrated circuits and some nanodevices [14], while the dielectric materials with high permittivities can be applied for high energy storage [15]. With the prevalence of the high-performance nanomaterials, metrology techniques are urgently required to quantitatively characterize electrical properties at the nanoscale.

M-AFM was developed to realize the non-contact and non-destructive evaluation for

nanomaterials [16, 17]. Microwave can propagate via the cantilever of the probe of M-AFM and then emit from a slit at the tip. Based on the microwave measurement and non-contact mode of AFM, M-AFM had been proved as a favorable technique to measure the electrical conductivity of the samples at nanoscale. Recently, in order to describe the atomic force effect by microwave on the interaction between the M-AFM probe and evaluated material, a theoretical model to quantitatively characterize the local relative permittivity of the sample have been developed [18]. And the relative permittivity of bulk materials measurement was established on the M-AFM. When the M-AFM tip is scanning the sample surface, an additional coulomb force is generated.

In order to measure the Coulomb force caused by microwave, force distance curve is measured in this study. Force distance curves is applied to study different surface physical or chemical properties. From the end of last century, a large number of studies characterize novel atomic forces based on force curves measurement.

For instance, in recent research, Force-distance-curve based AFM imaging has now reached an exciting stage where it can be used to image the architecture of complex biological systems and systematically analyze the local biological and physical properties with a nanometer scale [19]. To achieve the objective, the AFM technique is applied to measure the force curves on the sample. Each of the force curves reflects the local interatomic force on the sample with high accuracy and sensitivity. These interatomic forces are measured pixel by pixel on the sample. Thus, the interaction on the sample surface can be entirely mapped and reflected by the AFM. This research reveals that the force curve measurement method can evaluate the physical, chemical

and biological forces, and functions as a molecular toolbox, allowing the target surface property combining different kinds of interactions to be comprehensively investigated. Therefore, the force curve measurement method is a promising technique to the quantitatively analyze the biological, chemical and physical properties on different samples.

In this study, the force curve measurement method is applied on the insulators to analyze the force between the tip and sample. By measuring the force distance curve between the tip and sample, the relative permittivity of the sample material can be evaluated. In this chapter, the topography and microwave images of ZnO, CuO nanowires and SnO_2 nanobelts by the M-AFM was realized. In addition, the quantitative evaluation of the permittivities of the metal oxide nanomaterials was succeeded based on the force curves measured by M-AFM. In this chapter, the morphology and microwave image of one-dimensional nanomaterials are successfully visualized, and the local relative permittivity are evaluated in a quantitative and non-contact mode.

This chapter firstly describes the mechanism of the influence on the Van der Waals force caused by microwave and how to apply this effect to evaluate the permittivity of the semiconductor and insulator materials. Then the different samples are fabricated. After that the morphology and microwave images of ZnO, CuO nanowires and SnO_2 nanobelts are measured. Finally, the electrical permittivity of the one-dimensional nanomaterials is evaluated by M-AFM

3.2 Theoretical Model

As revealed in Fig. 3.1 (a), there are electrode charges on the Au film of M-AFM tip when the microwave is applied on the sample. The M-AFM probe that functions as a parallel plate waveguide conducts and emits the microwave through the slit on the probe. On the other hand, when the electrical field of the microwave is transmitted across a dielectric, the polarized atoms are caused in the sample. Since the direction of the electric field on the tip is contrary to that of dipoles' polarization on the sample surface, the dipoles generate an attractive force to the tip. Thus, the Coulomb force between the charge on the M-AFM probe and the dipoles in the sample is generated by the microwave emitted from the tip. In this research, the near field approximation is applied to the quantitative calculation since the distance between the tip and sample (about 10 nm) is significantly shorter than the wavelength of microwave. On the other hand, the structure of the M-AFM probe is considered has a sharp tip that only the charges at the top of the tip should be taken into consideration. Thus, the electrical field of the incident microwave is considered as the electric field of two groups of sinusoidally alternating charges with opposite polarities.

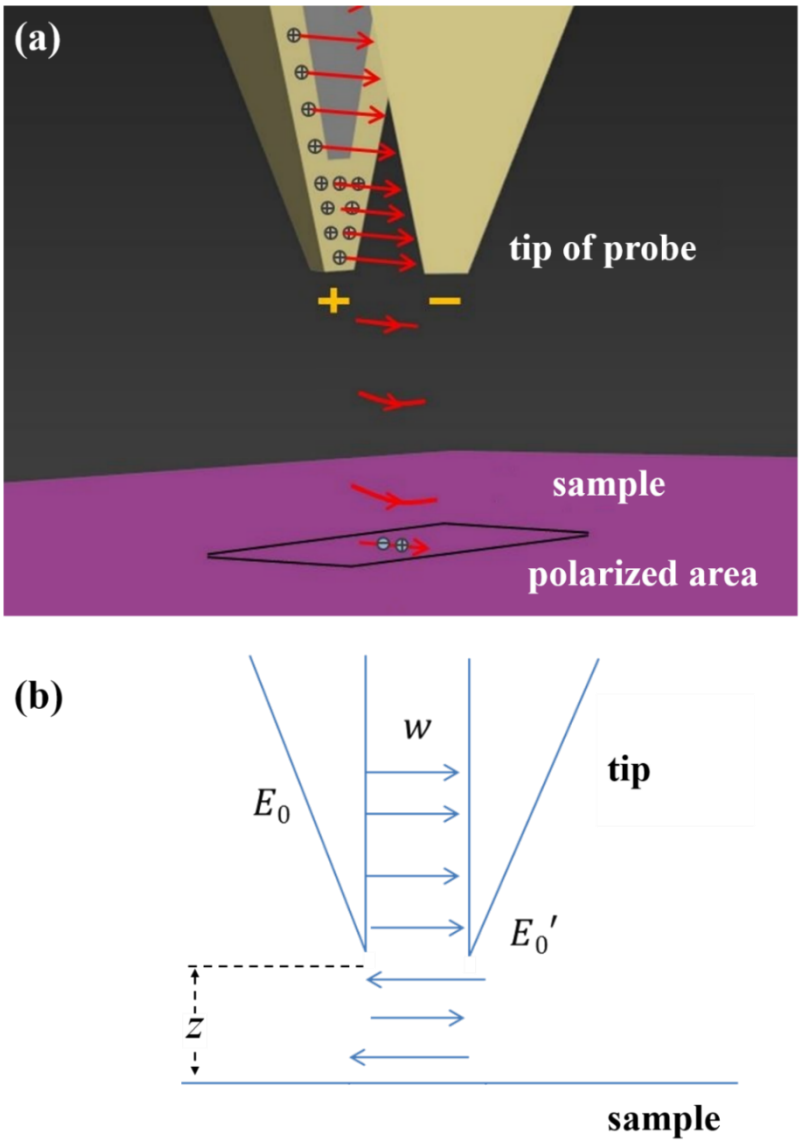

Fig. 3.1 The interaction between electrode charges of the tip and the dipoles on the sample surface.

Fig. 3.1 (b) illustrated the cross section between the tip and sample. The meaning of each parameter is explained. w is the distance between the two halves of the tip and z is the distance between tip and sample. E_0 is the incident electric-field amplitude at the middle of the dipole. E_0' is the reflected electric-field amplitude.

In this case, the equivalent charges q_0 is represented as the equation below:

$$q_0 = \frac{\pi}{2} w^2 \varepsilon_0 E_0 \qquad (3.1)$$

Where ε_0 is the permittivity of free space.

According to method of image charges, if a single point charge is placed over the sample with a distance z_0, the electric field of the polarized charge q_1 is represented as the equation below:

$$q_1 = \frac{1-\varepsilon_r}{1+\varepsilon_r} q_0 \qquad (3.2)$$

When microwave is applied, the effect of microwave should be taken into consideration. The Coulomb force F_{M0} between the M-AFM tip and sample can be expressed as [20]:

$$F_{M0} = -\frac{\varepsilon_r - 1}{\varepsilon_r + 1} \frac{\pi \varepsilon_0 w^4 E_0^2}{16} \left\{ \frac{1}{4z^2} - \frac{2z}{(4z^2 + w^2)^{\frac{3}{2}}} \right\} \qquad (3.3)$$

ε_r is the relative permittivity of the sample. Since the amplitude of electric field of microwave is shifting with time which is $E_0 sin\omega t$. Consider that the amplitude of microwave is time-dependent which is $E_0 \sin \omega t$. And the microwave frequency (94 GHz) is much more than that of cantilever vibration f_0 (100 kHz). The time-dependent force $F_{M0} sin^2\ \omega t$ that functions as its root mean square value is written as:

$$F_M = \frac{F_{M0}}{2} \qquad (3.4)$$

On the other hand, the atomic force F_A, between the tip and sample, is distance dependent, while F_A from an irregular-shaped structure consist of three terms, can be presented as [20]:

$$F_A = A_1 z^{-1} + A_2 z^{-2} + A_3 z^{-3} \qquad (3.5)$$

Where A_1, A_2, A_3 are parameters based on different components, and z is the distance between the tip and the sample, while $A_1 z^{-1}$, $A_2 z^{-2}$, and $A_3 z^{-3}$ stand the forces between the tip and sample in a conic, spherical and a cubic shape, respectively [21,22].

In the non-contact mode, the M-AFM probe vibrates at the resonance frequency with an amplitude of few nanometers, and the frequency of the vibration changes when the probe approaches the sample. Utilizing the small-amplitude approximation, the change of the resonance frequency, Δf, and the gradient of atomic force, dF_A/dz, can be written as:

$$\Delta f = -\frac{f_0}{2k}\frac{dF_A}{dz} \qquad (3.6)$$

Where k and f_0 are the spring constant and the resonance frequency of the cantilever. Therefore, through the measurement of M-AFM without microwave, the gradient of the

interatomic force is represented as follows:

$$-\frac{dF_A}{dz} = \frac{2k}{f_0}\Delta f = A_1' z^{-2} + A_2' z^{-3} + A_3' z^{-4} \qquad (3.7)$$

A_1', A_2', and A_3' can be determined based on the force curves of M-AFM. When the microwave is applied, the force between the tip and sample should be written as:

$$\Delta f' = -\frac{f_0}{2k}\left(\frac{dF_A}{dz} + \frac{dF_M}{dz}\right) \qquad (3.8)$$

Finally, the gradient of the force between the tip and sample should be written as:

$$-\frac{dF}{dz} = \frac{2k}{f_0}\Delta f' = A_1' z^{-2} + A_2' z^{-3} + A_3' z^{-4} + MH(z) \qquad (3.9)$$

Where M is [20]

$$M = \frac{\varepsilon_r - 1}{\varepsilon_r + 1}\frac{\pi \varepsilon_0 w^4 E_0^2}{16} \qquad (3.10)$$

and $H(z)$ is [20]

$$H(z) = \frac{1}{2z^3} + \frac{2w^2 - 16z^2}{(4z^2 + w^2)^{5/2}} \qquad (3.11)$$

By measuring the force curves without microwave and fitting the force curves with

Eqs. (3.7), (3.9) and (3.10). The parameter A_1', A_2' and A_3' can be obtained. Then, M is calculated by measuring the force curves with microwave and fitting the measured force curves with Eq. (3.10). By measuring the force curve of Si substrate with a known relative permittivity ε_{r1}, the relative permittivity ε_{r2} of an unknown sample is represented as below.

$$\frac{M1}{M2} = \frac{\varepsilon_{r1}-1}{\varepsilon_{r1}+1} \cdot \frac{\varepsilon_{r2}+1}{\varepsilon_{r2}-1} \qquad (3.12)$$

3.3 Fabrication of Sample

The studies of one-dimensional nanostructures have focused primarily on lithographically and epitaxially defined quantum wires embedded in a semiconductor medium such as nanowire fasteners and nanowire solar cells. Free-standing nanowires have several attractive differences from these systems, including a large variation in the relative permittivity of the surrounding medias. Here in order to study the relative permittivity of individual free-standing metal oxide nanomaterials, the nanomaterials should be dispersed on a substrate. First of all, the CuO nanowires were synthesized by thermal oxidation [23]. The ZnO nanowires and SnO_2 nanobelts were synthesized by thermal sublimation [24]. Scanning electron microscopy show that individual and well-isolated nanowires are readily produced by this method (Fig. 3.2). In order to increase the difference of reflectivity between the substrate and nanowires, the silicon wafer substrates coated with a 100 nm Au film by EBPVD, was used in the experiment. The

suspension of each kind of nanowires in ethyl alcohol was prepared by ultrasonic dispersion. Several drops of the suspension were dispersed onto the Au film and dried at room temperature.

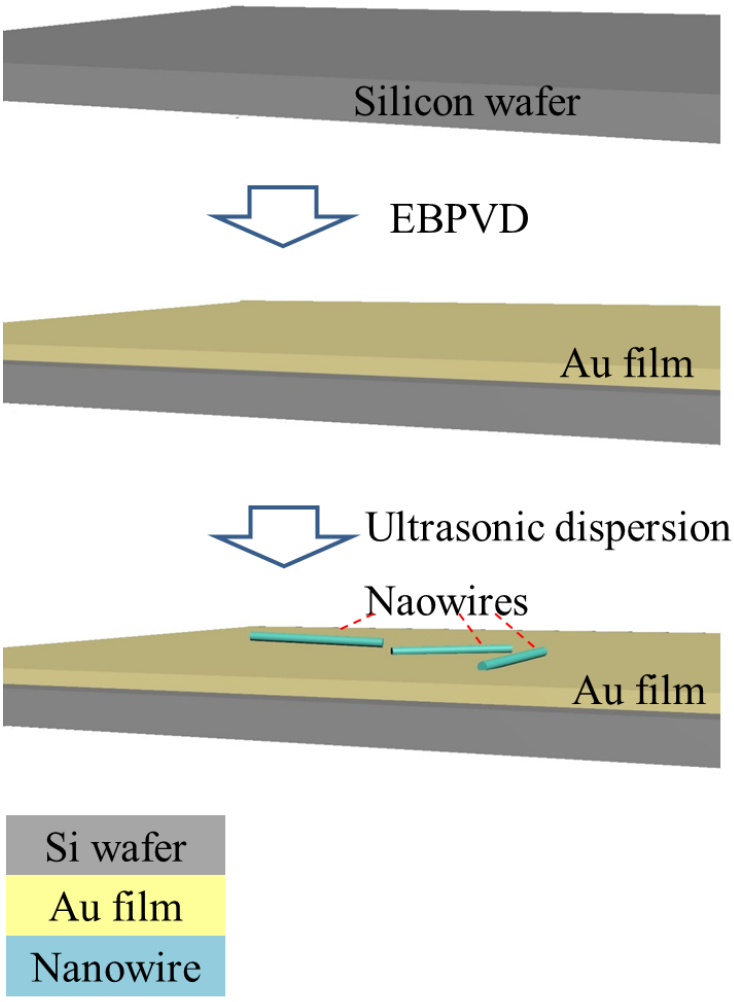

Fig. 3.2 Fabrication of the nanowire sample

After dispersing the nanowires onto the Au film, the scanning electron microscopy (SEM) were used to characterize the morphological features of nanowires as shown in Fig. 3.3. Fig. 3.3 (a) displays the SEM result of ZnO nanowires. Fig. 3.3 (b) displays the SEM result of CuO nanowires. And Fig. 3.3 (c) displays the SnO_2 nanobelts.

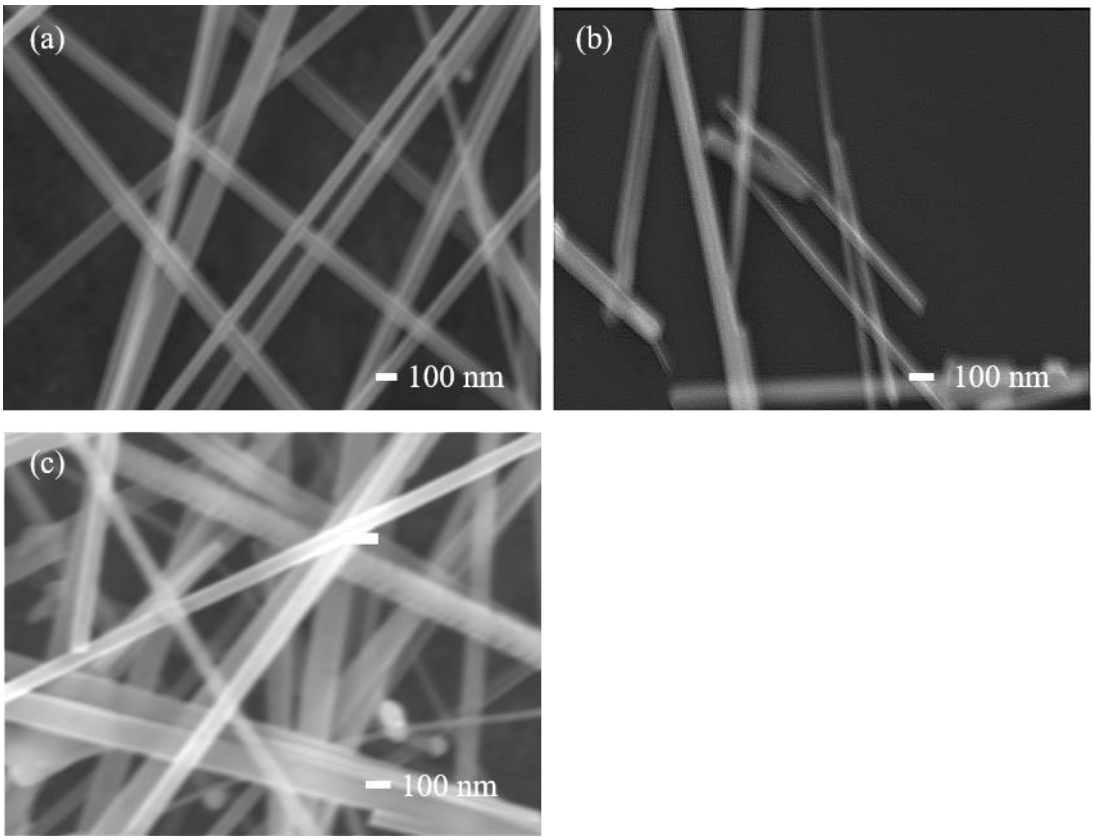

Fig. 3.3 SEM images of (a) ZnO nanowires, (b) CuO nanowires and (c) SnO_2 nanobelts that are dispersed on the Au film. The diameter of each nanowire can be estimated.

3.4 Microwave Images and Force Distance Curves of Metal Oxide Nanomaterials

The measurements of CuO, ZnO nanowires and SnO_2 nanobelt were carried out by M-AFM with the scanning speed of 1 μm/s and the amplitude of microwave of 15 dbm. A commercial silicon wafer is measured by M-AFM for calibration when evaluating the relative permittivity of the one-dimensional nanomaterials. The experimental setup is illustrated in Fig. 3.4.

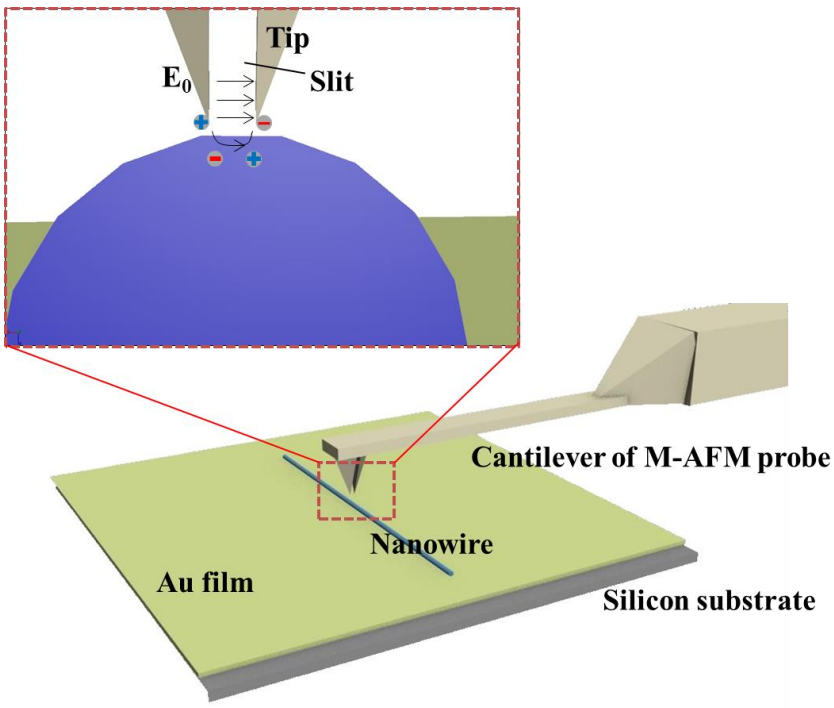

Fig. 3.4 Schematic diagram of interaction induced by microwave between M-AFM tip and nanowire

The silicon wafer also measured in the same condition with the one-dimensional nanomaterials by M-AFM. After the morphology and microwave images of each one-dimensional nanomaterial and the silicon wafer were measured by M-AFM, the morphology and microwave images of one-dimensional nanomaterials were evaluated as shown in Fig. 3.5. The force curves on the one-dimensional nanomaterial and the silicon wafer were measured at four conditions: without microwave, 5 dbm, 10 dbm, and 15 dbm microwave.

Fig. 3.3 displays the morphology of nanowires observed with the SEM. The diameters of ZnO nanowires and CuO nanowires are approximately 155 nm and 100 nm, respectively, while the width and thickness of SnO_2 nanobelts are approximately 150 nm and 100 nm, respectively. These results are in agreement with the morphology measured by M-AFM. As depicted in the measurement results of M-AFM as shown in Fig. 3.5, the diameter of the ZnO nanowires is approximately 140 nm on average, while that of the CuO nanowires is approximately 130 nm. The width and the thickness of SnO_2 nanobelts are approximately 165 nm and 110 nm respectively. As shown in Fig. 3.5, the microwave images were measured for each of the one-dimensional nanomaterials and the silicon wafer. Since the reflectivity of the one-dimensional nanomaterials and the Au film substrate is different, microwave images can distinguish these one-dimensional nanomaterials. These results indicated that M-AFM has the ability to visualize the measured nanowires with high accuracy.

(a)

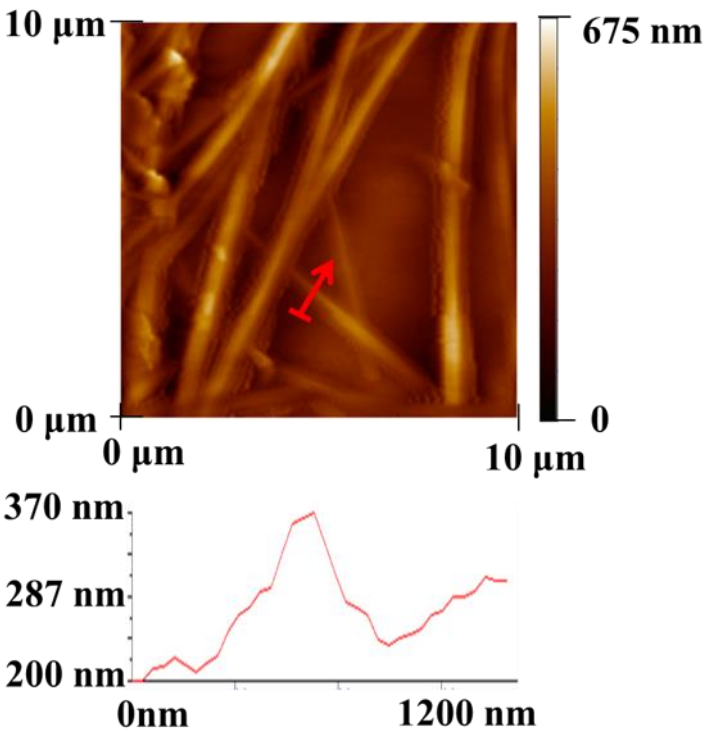
10 µm
675 nm
0 µm
0
0 µm
10 µm
370 nm
287 nm
200 nm
0nm
1200 nm

(b)

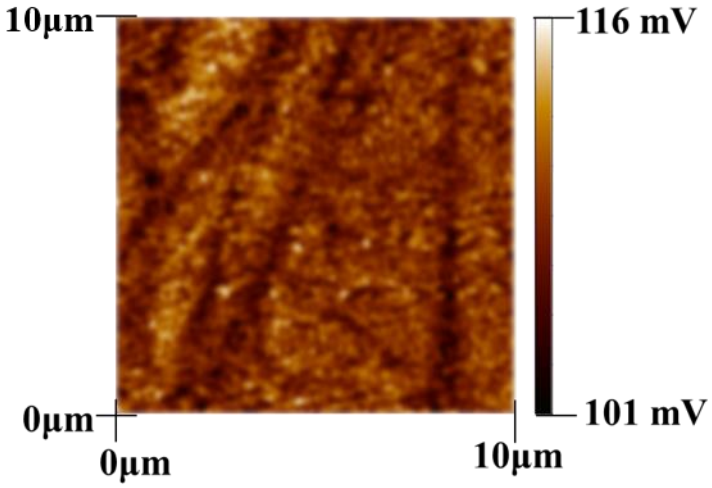
10µm
116 mV
0µm
101 mV
0µm
10µm

(c)

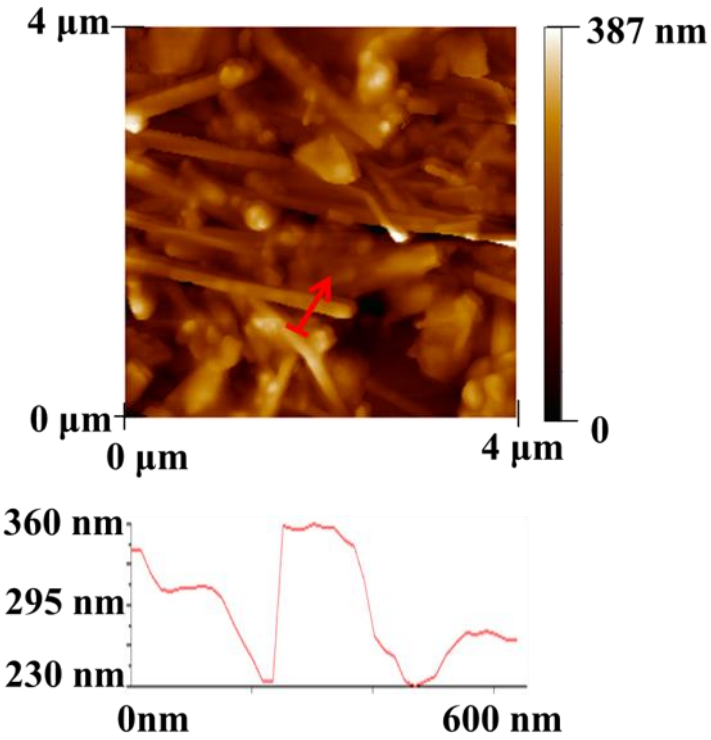
4 µm
387 nm
0 µm
0
0 µm
4 µm
360 nm
295 nm
230 nm
0nm
600 nm

(d)

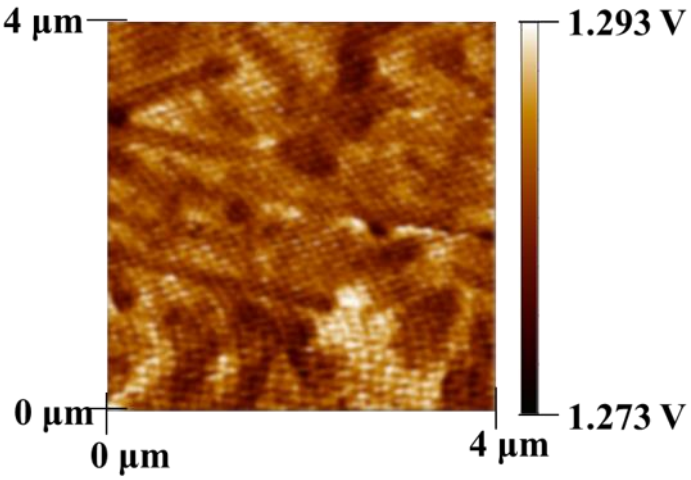
4 µm
1.293 V
0 µm
1.273 V
0 µm
4 µm

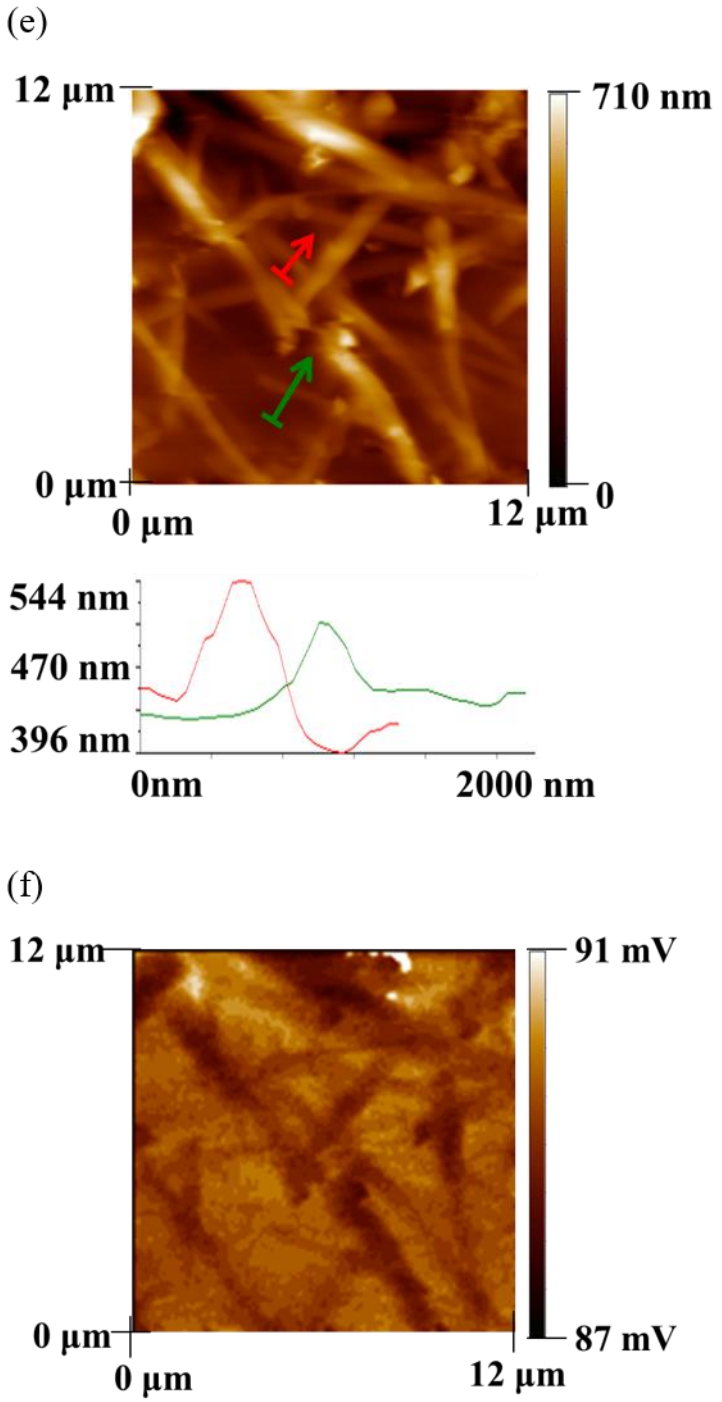

Fig. 3.5 The experimental result measured by M-AFM: (a) the topography of the ZnO nanowire; (b) the microwave image of the ZnO nanowire; (c) the topography of the CuO nanowire; (d) the microwave image of the CuO nanowire; (e) the topography of the SnO_2 nanobelt; (f) the microwave image of the SnO_2 nanobelt.

3.5 Quantitative Evaluation of Local Permittivity of Metal Oxide Nanomaterials

After the microwave image and topography of the CuO, ZnO nanowires and SnO_2 nanobelt are measured by M-AFM, several points are selected on the sample to measure the force curve of each sample in order to evaluate the relative permittivity of these nanomaterials. The diagram of force curve measurement is illustrated in Fig.3.6.

In the force curve measurement, the probe is measure on one point of the sample surface as shown in Fig. 3.6. Different from the scanning mode, the force distance curve measurement method is utilized to study the interatomic force.

In Fig. 3.6, the M-AFM probe stays at the standoff distance above the sample and keeps vibrating. When standoff distance equals to zero, the vibration frequency begins to decrease. Once the standoff distance is less than 0 nm, the tip of the M-AFM will receive the impact from the sample’s atomic force.

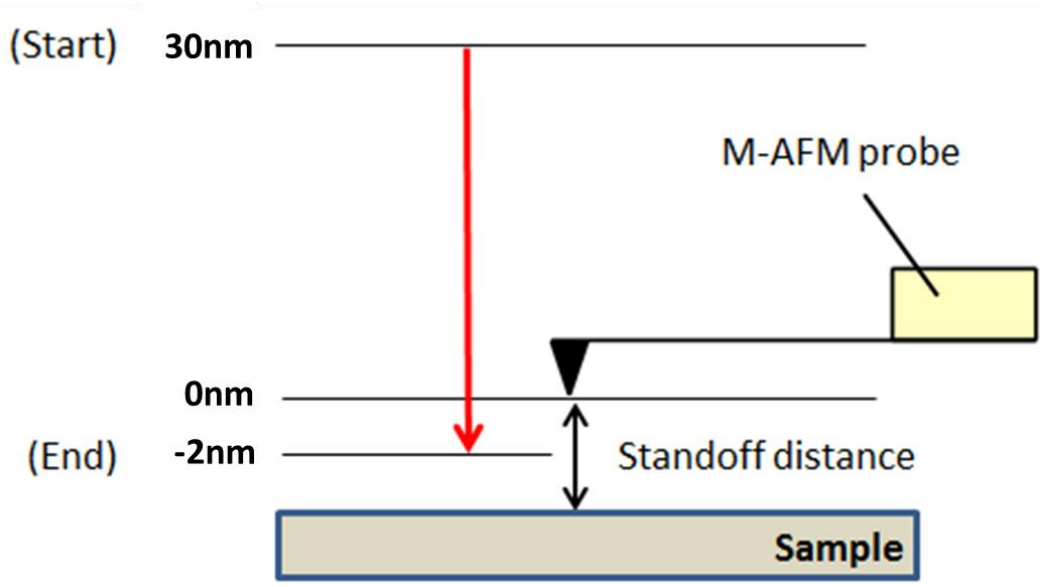

Fig. 3.6 The force curve measurement method.

While measuring the force curves, the piezo of the probe is ramped while the sample stage is moving vertically. In the non-contact mode, the cantilever of M-AFM probe keeps vibrating with an additional piezoelectric signal when approaching the sample. Meanwhile M-AFM records the change of the resonance frequency along the moving track. As a result, the force curve that shows the relationship between the change of the resonance frequency and the distance between the tip and sample can be obtained.

During force curve the change of the frequency of the probe can be measured, and by applying Eq. (3.6), the connection between the change of the frequency and force differential can be calculated.

Here the silicon is implemented as a sample and the force curve measurement is applied on the silicon wafer. In the force curve measurement, the silicon wafer is N type. The orientation is (100) with edge (110). The electrical resistance is over 1000 Ω·cm. The force distance curve is measured without microwave and in the condition

with microwave. The frequency of microwave is 94 GHz and the amplitudes of the microwave 0 dbm, 5 dbm and 10 dbm. The force curves under different amplitudes are measured separately. According to the function, the force curve data without microwave and that with 10 dbm microwave is enough to calculate the relative permittivity. So only the force curve data without microwave and that with microwave at 10 dbm are processed by nonlinear fitting.

As shown in Fig. 3.7, the respective force curves of ZnO, CuO nanowires and SnO_2 nanobelts are illustrated for the measurement under the condition without microwave, and with 5 dbm, 10 dbm and 15 dbm microwaves, respectively. When there is no microwave, the resonance frequency decrease with the decrease of the distance between the tip and the sample, which means that the atomic force is an attractive force. When microwave was applied, the curves declined in a sheer amount. With the increase of the amplitude of microwave, the curves further plummeted. This indicated that microwave induced an attractive force between the tip and sample, and this force increase with the increase of amplitude of microwave, which is in agreement with the theoretical analysis. By fitting the force curves with Eqs. (3.7) and (3.9), the parameters M of silicon wafer was obtained. With similar calculation, the parameters M of ZnO and CuO nanowires as well as SnO_2 nanobelts were obtained. Using the nominal permittivity of silicon wafer as 11 to calibrate and combine Eq. (3.11), the relative permittivity of each nanowire was calculated. The evaluated results of the nanowires versus their reference values are shown in Fig. 3.8. These results are average values of five measurements.

(a)

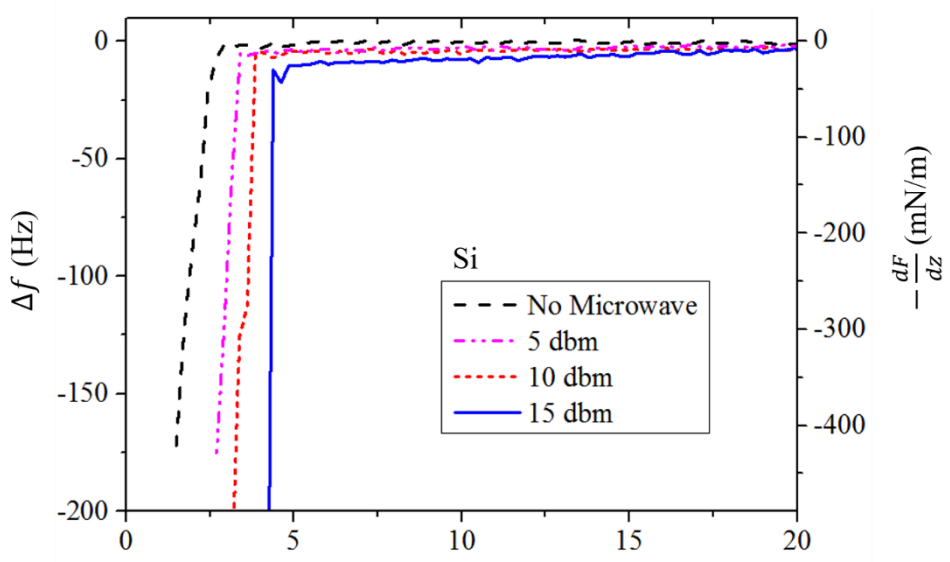
Si
No Microwave
5 dbm
10 dbm
15 dbm
Δf (Hz)
$-\frac{dF}{dz}$ (mN/m)

(b)

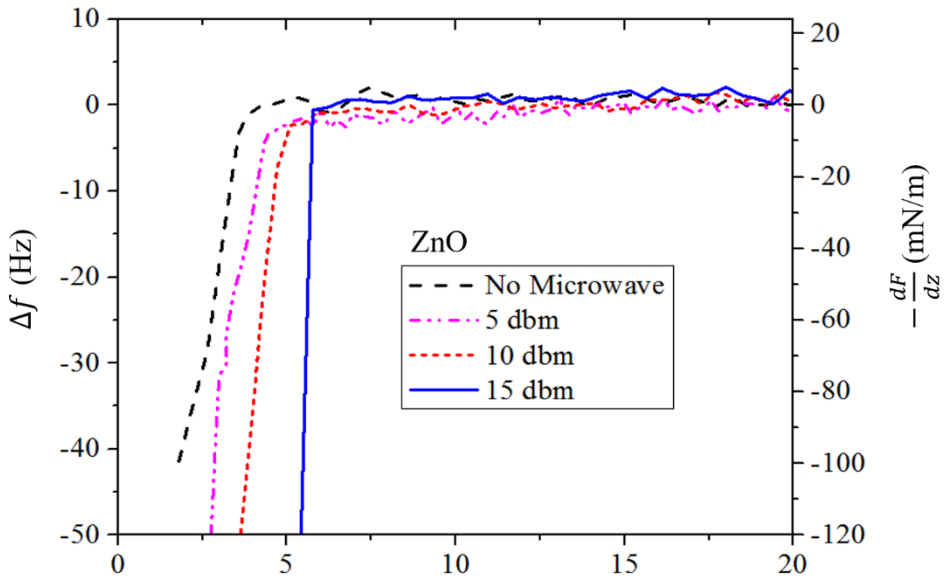
ZnO
No Microwave
5 dbm
10 dbm
15 dbm
Δf (Hz)
$-\frac{dF}{dz}$ (mN/m)

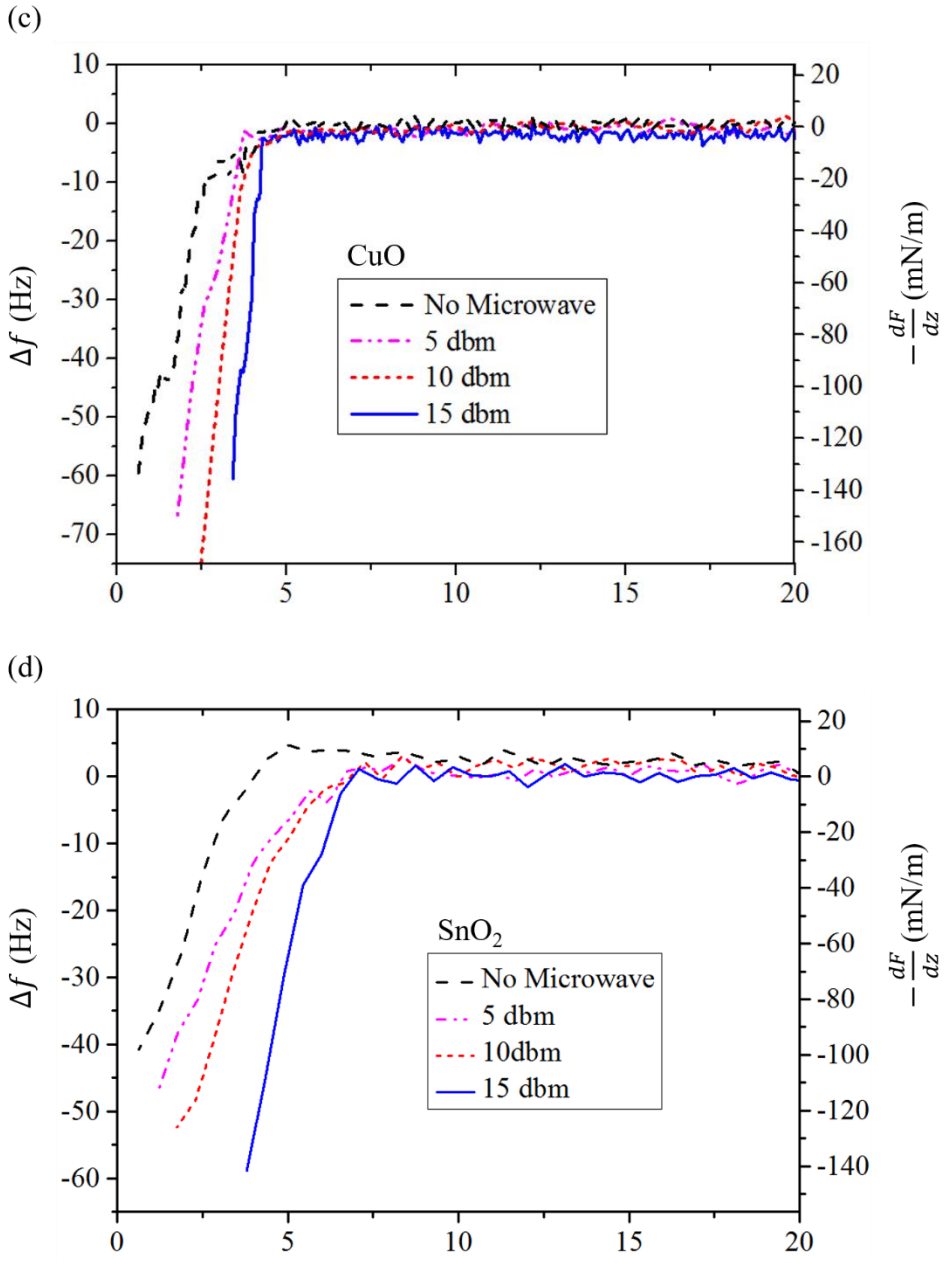

Fig. 3.7 The force distance curves measured by M-AFM without microwave and with 5 dbm 10 dbm and 15 dbm microwave: (a) the force distance curves of Si wafer; (b) the force distance curves of ZnO nanowires microwave; (c) the force distance curves of CuO wafer; (d) the force distance curves of SnO_2 nanobelts.

As listed in Table 3.1, the relative permittivity of ZnO nanowires was evaluated to be 3.82, 4.02, 3.86, respectively under the condition of 5, 10 and 15 dbm microwave.

The nominal value of bulk ZnO material is 8.1 [25]. The relative permittivity measured on a ZnO nanowire was ranging from 2.4 to 6.4 [26]. The relative permittivity of ZnO nanoparticle was 6 which was measured at 10 MHz [27].

Table 3.1 Results calculated from the measured force curves and nominal values including parameter M, evaluated relative permittivities with 5 dbm, 10 dbm and 15 dbm microwave.

Measured materials	CuO nanowire	ZnO nanowire	SnO_2 nanobelt
Nominal value	18.1	8.1	13.5
Evaluated value (15 dbm)	17.97	3.82	11.54
Evaluated value (10 dbm)	16.07	4.02	11.64
Evaluated value (5 dbm)	18.62	3.86	11.37

The relative permittivity of CuO nanowires was 18.62, 16.07, 17.97, measured with 5 dbm, 10 dbm and 15 dbm, respectively. The nominal value of CuO bulk material is 18.1 [25]. In the study of Das, different CuO nanoknife arrays are fabricated [28]. Besides, they found that the relative permittivity of fabricated CuO nanomaterials is the same as that of CuO bulk material, which is 18.1. The relative permittivity of SnO_2 nanobelts was 11.37, 11.64, 11.54, measured with 5 dbm, 10 dbm and 15 dbm, respectively. The relative the static relative permittivity of SnO_2 bulk material is 13.5 [25]. Li. [29] synthesize the SnO_2 nanowires and evaluated the relative permittivity of

SnO_2. In 10 MHz frequency, the measured result of Li was approximately 13, which is close to our result. Therefore, the dielectric properties of ZnO, CuO, and SnO_2 nanowires measured by M-AFM are in agreement with nominal values and previous studies. However, errors still exist. With respect to the relative permittivity of ZnO nanowires, our result was different from the nominal value [25] but agree with the values in the researches of Yang [26]. The high frequency of microwave (94 GHz) on M-AFM induced the difference between our result and that of nominal value. Because of the frequency dependence of the relative permittivity, the relative permittivity will be lower when the frequency increases. This deviation was caused by the frequency of our experiment which is 94 GHz. Similarly, the evaluated relative permittivity of CuO nanowires is lower than the nominal value [25], the deviation of the evaluated relative permittivity is caused by the different frequency between the researchers. The static relative permittivity of SnO_2 bulk material is 9.86 while the electrical field vector is parallel to the crystal c-axis and 13.5 while it is perpendicular to the crystal c-axis [25]. However, SnO_2 nanobelt crystal grew along in the crystallographic direction [1, 0, 1], which caused a deviation of SnO_2 nanobelt because of different crystallographic surface. Besides the difference of frequency, the shape of the sample was another influential factor. Theoretically, the sample was flat [20], while it was not in our research. However, this assumption may not be strictly accurate when the distance between the tip and sample was less than 10 nm. To sum up, the contribution of this study is to evaluate the local relative permittivity of one-dimensional nanomaterials in a non-contact mode based on M-AFM technology by a quantitative and non-destructive

measurement.

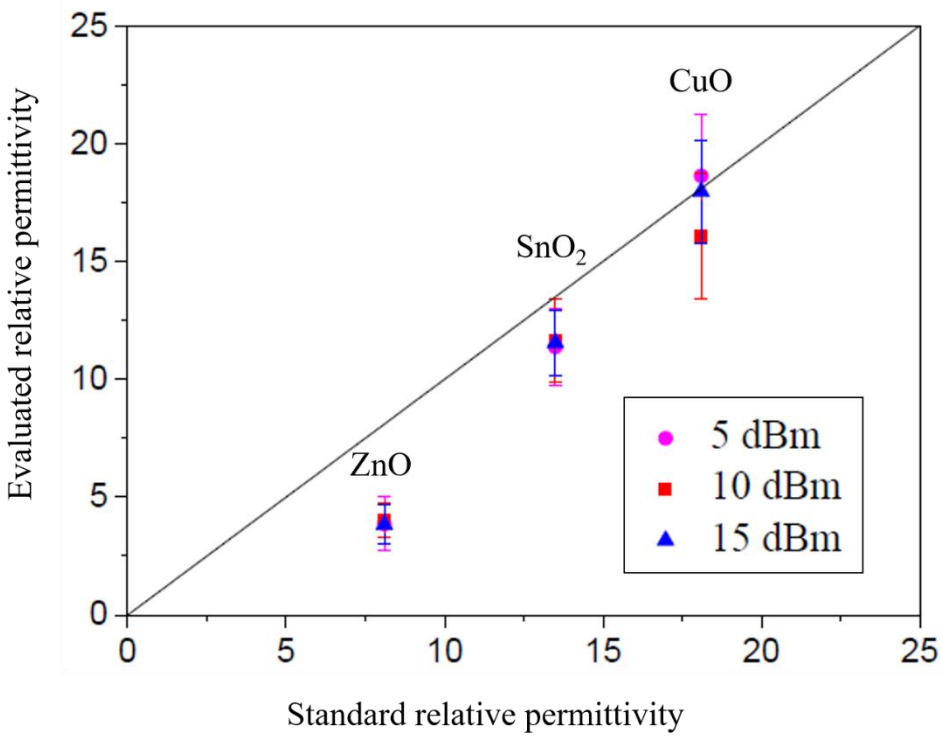

Fig. 3.8 The nominal relative permittivity from reference compared with the relative permittivity evaluated with force distance curve by M-AFM under 5 dbm, 10 dbm and 15 dbm microwave.

3.6 Discussion

The evaluated relative permittivity of the nanomaterial by M-AFM is different from the static relative permittivity of bulk material. The error may be caused by the following two reasons.

Firstly, the relative permittivity of one-dimensional nanomaterials could be different from that of bulk materials. The one-dimensional nanomaterials have a higher surface to volume ratio and more surface defects when compared with bulk materials. Thus, the arrangement of atoms between nanomaterial and bulk material are different, which resulting in a difference in the relative permittivity.

Secondly, the evaluated relative permittivity will change if the frequency of the electromagnetic wave changes. Several kinds of the polarization effects contribute to the overall relative permittivity as illustrated in Fig. 3.9 [30]. If the frequency of microwave affects the evaluated relative permittivity, it's necessary to discuss that the evaluated relative permittivity is measured in a high or low frequency.

More specifically, the frequency of the microwave is 94 GHz in this research, which is between the dipolar and the atomic polarization, according to Fig. 3.9. Thus, it is significant to discuss that the polarized atoms on the surface of the evaluated nanomaterial are mainly dipolar polarization or atomic polarization.

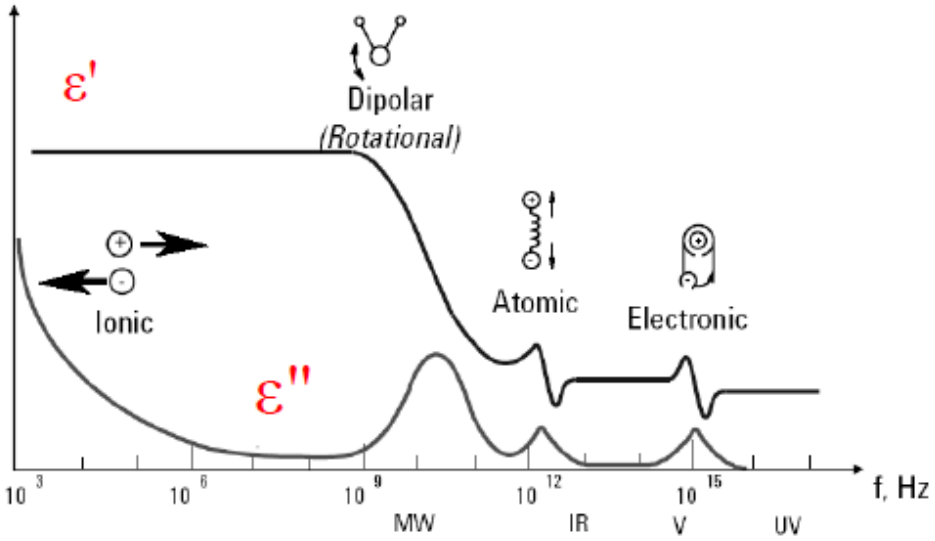

Fig. 3.9 Frequency response of dielectric mechanisms [30]

When applying high frequency evaluation techniques such as terahertz time-domain spectroscopy to measure the sample [31], the whole sample is polarized and evaluated. Specifically, the applied electric field is approximately equal to that of each atom in the evaluated sample, and the response of the atomic electrons can be modeled as harmonics. Thus, the relative permittivity under high frequency conditions and the influence of atomic polarization can be evaluated. However, in this study, the polarized area of microwave radiation under the M-AFM probe is in an area about 100 * 100 nm. The electric field of the atoms in the center of this area is equal to the applied electric field of microwave. As the distance from the center increases, the frequency of the electric field of the atoms remains unchanged, but the amplitude of the electric field becomes smaller, and the direction of the electrical field also changed. Thus, when building the theoretical model, two approximations are made. First of all, the electric field of microwave radiation is based on a near-field approximation. Secondly, the

dipoles are caused by the microwave in the polarized area and only the dipolar polarization is considered in the theoretical model.

In Tong's research [20], this approximated model and evaluation method proved to be able to accurately evaluate the relative permittivity of the measured bulk dielectric materials.

In Table 3.2, the measured relative permittivity is compared with the nominal values. Nominal value in low frequency is investigated from Shannon's result [25]. Nominal values at 200 GHz are experimentally evaluated data by terahertz time-domain spectroscopy [32] [33] [34]. Nominal value in high frequency that is more than 20 THz is calculated by first principle [35]. In this study, the measured permittivity also agrees with the nominal value at low frequency.

To sum up, the polarization of the sample measured by M-AFM is a dipolar polarization, and M-AFM measures the relative permittivity in low frequency. Thus, the microwave influence from M-AFM on the relative permittivity of the one-dimensional nanomaterial evaluated in this experiment is negligible.

Table 3.2 Nominal values compared with evaluated relative permittivities with 5 dbm, 10 dbm and 15 dbm microwave.

Measured materials	CuO nanowire	ZnO nanowire	SnO_2 nanobelt
Nominal value (static relative permittivity)	18.1	8.1	13.5
Evaluated value (15 dbm)	17.97	3.82	11.54
Evaluated value (10 dbm)	16.07	4.02	11.64
Evaluated value (5 dbm)	18.62	3.86	11.37
Nominal value (at $2*10^{11}$ Hz)	6.0	7.9	2.3
Nominal value (above $2*10^{13}$ Hz)	7.2	3.7	3.8

3.7 Summary

In this research, the main results are summarized as follows: first, the morphology and microwave image of several metal oxide semiconductor nanomaterials were obtained by M-AFM, which were in agreement with the SEM observation results. Secondly, based on the force curves of M-AFM, a method to evaluate the local relative permittivity of metal oxide nanostructures was introduced. At last, by measuring the force curves by M-AFM on the one-dimensional nanomaterials, quantification of the local relative permittivity of the nanowires was developed based on the M-AFM. The

topography as well as microwave images measured by M-AFM were highly reproducible. This measurement method of local relative permittivity is significant since it is experimentally revealed that the dielectric properties of semiconductor nanomaterials are different from those of bulk materials [26,27]. Moreover, compared with the result measured ZnO nanowires in the research of Yang [26] and the research of P.G.Li [29] measured SnO_2 nanowires, M-AFM can visualize the morphology and reflected microwave signals with high resolution and accuracy, which indicated that M-AFM could be more suitable to locate and measure the local relative permittivity when compared with other means. Compare with other AFM techniques, this study succeeded measuring the local relative permittivity of one-dimensional nanomaterials quantitatively and non-destructively using a non-contact mode based on M-AFM technology. Therefore, the high spatial resolution and this evaluation method of relative permittivity based on the M-AFM can fulfill the need of evaluating local electrical properties of nanomaterials.

Reference

[1] Y. W. Heo, D. P. Nortona, L. C. Tiena, Y. Kwona, B. S. Kang, F. Ren, S. J. Peartona, J. R. LaRoche, ZnO nanowire growth and devices, Materials Science and Engineering: R: Reports, **47**, 1 (2004).

[2] T. Ha, and V. Nguyen, Copper oxide nanomaterials prepared by solution methods, some properties, and potential applications: a brief review, International scholarly research notices, **2014** (2014).

[3] Dai, Z. R., et al., Tin oxide nanowires, nanoribbons, and nanotubes, The Journal of Physical Chemistry B, **106**, 1274 (2002).

[4] T. Zhai, X. Fang, M. Liao, X. Xu, H. Zeng, B. Yoshio, and D. Golberg, A comprehensive review of one-dimensional metal-oxide nanostructure photodetectors, Sensors, **9** [8], 6504 (2009).

[5] S. Liu, X. Guo, M. Li, W. Zhang, X. Liu, and C. Li, Solution‐phase synthesis and characterization of single‐crystalline SnSe nanowires, Angewandte Chemie International Edition, **50** [50], 12050 (2011).

[6] Shankar, K. Shantha, and A. K. Raychaudhuri, Fabrication of nanowires of multicomponent oxides: Review of recent advances, Materials Science and Engineering: C, **25**, 738 (2005).

[7] S. Gubbala, V. Chakrapani, V. Kumar, and M. K. Sunkara, Band-Edge Engineered Hybrid Structures for Dye-Sensitized Solar Cells Based on SnO2 Nanowires, Advanced Functional Materials, **18** [16], 2411 (2008).

[8] X. Li, Metal assisted chemical etching for high aspect ratio nanostructures: A review

of characteristics and applications in photovoltaics, Current Opinion in Solid State and Materials Science, **16** [2], 71 (2012).

[9] Y. Yu, P. V. Kamat, and M. Kuno, A CdSe nanowire/quantum dot hybrid architecture for improving solar cell performance, Advanced Functional Materials, **20** [9], 1464 (2010).

[10] S. Ko, D. Lee, H. Kang, K. Nam, J. Yeo, S. Hong, C. Grigoropoulos, and H. Sung, Nanoforest of hydrothermally grown hierarchical ZnO nanowires for a high efficiency dye-sensitized solar cell, Nano letters, **11** [2], 666 (2011).

[11] R. R LaPierre, M. Robson, K. M. Azizur-Rahman, and P. Kuyanov, A review of III–V nanowire infrared photodetectors and sensors, Journal of Physics D: Applied Physics, **50** [12], 123001 (2017).

[12] Y. Sun,S. Liu, F. Meng, J. Liu, Z. Jin, L. Kong, and J. Liu, Metal oxide nanostructures and their gas sensing properties: a review, Sensors, **12** [3], 2610 (2012).

[13] R. Kumar, O. Al-Dossary, G. Kumar, and A. Umar, Zinc oxide nanostructures for NO2 gas–sensor applications: A review, Nano-Micro Letters, **7** [2], 97 (2015).

[14] S. Bagga, J. Akhtar, and S. Mishra, Synthesis and applications of ZnO nanowire: A review, AIP Conference Proceedings. AIP Publishing LLC, **1989** [1], 020004 (2018).

[15] A. S. Al-Asadi, L. A. Henley, M. Wasala, B. Muchharla, N. Perea-Lopez, V. Carozo, Z. Lin, M. Terrones, K. Mondal, K. Kordas, and S. Talapatra, Aligned carbon nanotube/zinc oxide nanowire hybrids as high performance electrodes for supercapacitor applications, Journal of Applied Physics, **121 [**12], 124303 (2017).

[16] L. Zhang, Y. Ju, A. Hosoi, and A. Fujimoto, Microwave atomic force microscopy

imaging for nanometer-scale electrical property characterization, Review of Scientific Instruments, **81** [12], 123708 (2010).

[17] L. Zhang, Y. Ju, A. Hosoi, and A. Fujimoto, Microwave atomic force microscopy: quantitative measurement and characterization of electrical properties on the nanometer scale, Applied Physics Express, **5** [1], 016602 (2011).

[18] X. Wu, Z. Hao, D. Wu, L. Zheng, Z. Jiang, V. Ganesan, Y. Wang, and K. Lai, Quantitative measurements of nanoscale permittivity and conductivity using tuning-fork-based microwave impedance microscopy, Review of Scientific Instruments, **89** [4], 043704 (2018).

[19] Y. Dufrêne1, T. Ando, R. Garcia, D. Alsteens, D. Martinez-Martin, A. Engel, C. Gerber, and D. Müller, Imaging modes of atomic force microscopy for application in molecular and cell biology, Nature nanotechnology, **12** [4], 295 (2017).

[20] B. Tong, M. Zhao, Y. Toku, Y. Morita, and Y. Ju, Local permittivity measurement of dielectric materials based on the non-contact force curve of microwave atomic force microscopy, Review of Scientific Instruments, **90** [3], 033706 (2019).

[21] S. Zanette, A. Caride, V. Nunes, G. Klimchitskaya, F. Freire, and R. Prioli, Theoretical and experimental investigation of the force–distance relation for an atomic force microscope with a pyramidal tip, Surface science, **453** [1], 75 (2000).

[22] H. J. Butt, B. Cappella, and M. Kappl, Force measurements with the atomic force microscope: Technique, interpretation and applications, Surface science reports, **59** [1], 1 (2005).

[23] X. Jiang, T. Herricks, and Y. Xia, CuO nanowires can be synthesized by heating

copper substrates in air, Nano letters, **2** [12], 1333 (2002).

[24] E. Comini, G.Faglia, G. Sberveglieri, D. Calestani, L. Zanotti, M. Zha, Tin oxide nanobelts electrical and sensing properties, Sensors and Actuators B: Chemical, **111**, 2 (2005).

[25] R. D. Shannon, Dielectric polarizabilities of ions in oxides and fluorides, Journal of Applied physics, **73**, 348 (1993).

[26] Y. Yang, W. Guo, X. Wang, Z. Wang, J. Qi and Y. Zhang, Size dependence of dielectric constant in a single pencil-like ZnO nanowire, Nano letters **12**, 1919 (2012).

[27] A. S. Lanje, S. J. Sharma, R. S. Ningthoujam, J. S. Ahn, and R. B. Pode, Low temperature dielectric studies of zinc oxide (ZnO) nanoparticles prepared by precipitation method, Advanced Powder Technology **24**, 331 (2013).

[28] S. Das, S. Saha, D. Sen, U. K. Ghorai, D. Banerjee, and K. K. Chattopadhyay, Highly oriented cupric oxide nanoknife arrays on flexible carbon fabric as high performing cold cathode emitter, Journal of Materials Chemistry C, **2**, 1321 (2014).

[29] P. G. Li, M. Lei, X. Wang, and W. Tang, Large-scale SnO2 nanowires synthesized by direct sublimation method and their enhanced dielectric responses, Materials Letters, **63**, 357 (2009).

[30] A. Ward, Dielectric materials for advanced applications, NRC, pp 10, 2015. DOI: 10.13140/RG.2.1.3481.5600

[31] H. J. Joyce, J. L. Boland, C. L. Davies, S. A. Baig, and M. B. Johnston, A review of the electrical properties of semiconductor nanowires: insights gained from terahertz conductivity spectroscopy, Semiconductor Science and Technology, **31** [10], 103003

(2016).

[32] F. Kernan, Material Characterization of Zinc Oxide in Bulk and Nanowire Form at Terahertz Frequencies[M]. Portland State University, 2012.

[33] K. P. Regan, J. R. Swierk, J. Neu, and C. A. Schumutternater, Frequency-dependent terahertz transient photoconductivity of mesoporous SnO2 films, The Journal of Physical Chemistry C, **121** [29], 15949 (2017).

[34] J. C. Rosa, A. Locquet, D. Bouscaud, S. Berveiller, and D. S. Citrin, Optical constants of CuO and ZnO particles in the terahertz frequency range, Ceramics International, **46** [15], 24110 (2020).

[35] J. A. Spencer, A. L. Mock, A. G. Jacobs, M. Schubert, Y. Zhang, and M. J. Tadjer, A review of band structure and material properties of transparent conducting and semiconducting oxides: Ga2O3, Al2O3, In2O3, ZnO, SnO2, CdO, NiO, CuO, and Sc2O3, Applied Physics Reviews, **9** [1], 011315 (2022).

Chapter 4 Quantitative Measurement of Local Conductivity of SnO_2 Nanobelt Field Effect Transistor Utilizing Microwave Atomic Force Microscopy

4.1 Introduction

Semiconductor nanomaterials such as nanowires and nanotubes have gained large popularity in recent years and become building blocks for the next generation of electronic devices because of their high surface-volume ratio, high-performance electronic properties, and easy to realize high-density-integration [1].

As an independent field of nanomaterials, nanobelts are considered as the ideal material to study dimensionally confined transport phenomena owing to their unique size-dependent properties and well-defined geometry [2]. Nanobelts have been regarded as model materials for a systematic experimental and theoretical understanding of the fundamental electrical, optical, and ionic transport processes of nanodevices [3].

Alternatively, field-effect transistors (FETs) have significantly contributed to electronics industry since the middle of the 20th century. Recently, nanomaterial FETs have been one of the most researched nanomaterial-based devices due to their exciting properties, such as favorable electronic properties [4], ultra-small dimensions [5], and

high sensitivity [6,7]. With these advantages, nanomaterial FETs have exhibited a broad range of applications in high-performance devices, such as gas sensors [8-10], biosensors [11-13], and optoelectronic devices [14-16].

To obtain the functions of nanomaterial FETs, it is vital to adjust the electrical conductivity of the nanomaterials is most important. Recently, from the utmost search for new nanomaterials with applicable properties in nanoelectronic devices, a variety of nanomaterials have been fabricated for nanomaterial FETs with different electrical conductivities that stem from the arrangement of the density of dopants, to reach different carrier densities and mobilities [17-19]. Therefore, the evaluation of the electrical conductivity of nanomaterial FETs is vital to understand the nature of the nanomaterials and pave the path to optimize different nano-electronic devices [20-22].

In this study, a non-doped SnO_2 nanobelt-based FET device was fabricated, and the local conductivity of the SnO_2 nanobelt affected by gate voltages was evaluated. With a wide bandgap (3.6 eV at 300 K), and low resistivity, SnO_2 is a typical semiconductor material used for nanomaterial FETs [1,3]. M-AFM measures the topography and microwave image of the SnO_2 nanobelt with a non-contact mode with high resolution. Based on the measured microwave image, the electrical conductivity of the single SnO_2 nanobelt was determined, which is significant for understanding the function and performance of nanomaterial FETs.

4.2 Principle of Microwave Measurement for Electrical Properties

The microwave measurement method in this study is based on the microwave surface reflection method. When microwave irradiates over the sample, the microwave reflects at the top and bottom surfaces of the sample. And the microwave signal reflected from the wafer will be the sum of the reflections from both the top and bottom surfaces. Therefore, the measured reflection coefficient depends on the electromagnetic parameters and the thickness of the wafer. According to our former research [23], the microwave frequency is set at 94 GHz. The size of the slit on the M-AFM probe is approximately 100 nm. The electric field of incident microwave on the sample surface should be about 100 nm as well. Therefore, the reflected microwave signal from the bottom of the sample is negligible and only that reflected from the top should be considered if the thickness of the evaluated sample is thicker than 100 nm [23]. When the M-AFM probe keeps a fixed distance from the evaluated material, the output reflected voltage *V* can be represented as the equation below [24]:

$$V = k_0|\Gamma|^2 + b_0 \qquad (4.1)$$

When the thickness of the wafer is large enough, $|\Gamma|^2$ can be replaced by $|\Gamma_s|^2$ which is the absolute value of the top surface reflection coefficient. Eq. (4.1) can be converted as [24]

$$|\Gamma_s| = \sqrt{(V - b_0)/k_0} \qquad (4.2)$$

On the other hand, the reflection coefficient $|\Gamma_s|$ can be calculated as [24]

$$|\Gamma_s| = \left|\frac{\eta_1-\eta_2}{\eta_1+\eta_2}\right| \qquad (4.3)$$

Where

$$\eta_1 = \sqrt{\mu_0/\varepsilon_0}$$

And

$$\eta_2 = \sqrt{\mu/\varepsilon}/\sqrt{1-j\sigma/(\omega\varepsilon)}$$

η_1 and η_2 are the intrinsic impedance of vacuum and the SnO_2 nanobelts respectively. σ and μ are the conductivity and permeability of the measured SnO_2 nanobelts. ω is the angular frequency of the microwave. The permittivity can be expressed as $\varepsilon = \varepsilon_0\varepsilon_r$, where ε_0 is the permittivity of the vacuum and ε_r is the relative permittivity. Because of the nonmagnetic performance of the SnO_2 nanobelts, the permeability μ is equal to the permeability of vacuum μ_0. Thus, the intrinsic impedance of the sample can be written as [24]

$$\eta_2 = \eta_1/\sqrt{\varepsilon_r - j\sigma/(\omega\varepsilon)} \qquad (4.4)$$

Based on Eqs. (4.3) and (4.4), $|\Gamma_s|$ can be calculated by [24]

$$|\Gamma_s| = \left|\frac{1-\sqrt{\varepsilon_r - j\sigma/(\omega\varepsilon_0)}}{1+\sqrt{\varepsilon_r - j\sigma/(\omega\varepsilon_0)}}\right| \qquad (4.5)$$

To evaluate the conductivity of the SnO_2 nanobelts, σ can be solved from Eq. (4.5)

$$\sigma = (\omega\varepsilon_0)\sqrt{1-(y\varepsilon_r)^2/y} \qquad (4.6)$$

where

$$y = \frac{(|\Gamma_s|^2+1)\sqrt{(2\varepsilon_r-1)(|\Gamma_s|^2-1)^2+4|\Gamma_s|^2}-4|\Gamma_s|^2}{(2\varepsilon_r-1)(|\Gamma_s|^2+1)^2+4|\Gamma_s|^2} \qquad (4.7)$$

In order to calculate k_0 and b_0 in Eq. (4.1), two kinds of materials with investigated electrical conductivities are applied for calibration. The electrical conductivity of the measured sample can be determined by Eq. (4.1), (4.6) and (4.7).

To determine k_0 and b_0 in Eq. (4.1), a Ge wafer and Si wafer with known conductivities were used for calibration. The σ values of the Ge and Si wafers were 2 S/m and 10 S/m, and their ε_r were 16.2 and 11.9, respectively. Thus, their $\left|\Gamma_s\right|$ can be calculated using Eq. (4.6). In this study, the measured output voltages of M-AFM for Ge and Si wafers are 18.3 mV and 14.9 mV, respectively. Finally, from Eq. (4.1), k_0 and b_0 were determined to be 65.6 and -5.7, respectively.

4.3 SnO_2 Material

Before the experiment, it is necessary to investigate the nature of the SnO_2 nanomaterial. In this section, firstly, the crystal structure of the SnO_2 bulk material and the surface atomic alignment are investigated. Then the corresponding energy bands structure are respectively inquired. Finally, the influence of the lattice defect is analyzed.

Generally, the SnO_2 bulk material crystallizes in the rutile structure as shown in Fig. 4.1 [25]. With pressure induced transition, the rutile structure can also crystallize in other different types [25].

Based on the rutile structure, the band gap of SnO_2 bulk material is studied as below [26]. As a typical metal oxide material, O-2s contributes most of the density of states below -15 eV, while O-2p contributes the whole upper valence band which higher than -15 eV. Sn contributes the valence band that below -5 eV or above 5 eV. At the bottom of conduction band, the dispersion is relatively high and the band gap is 3.6 eV.

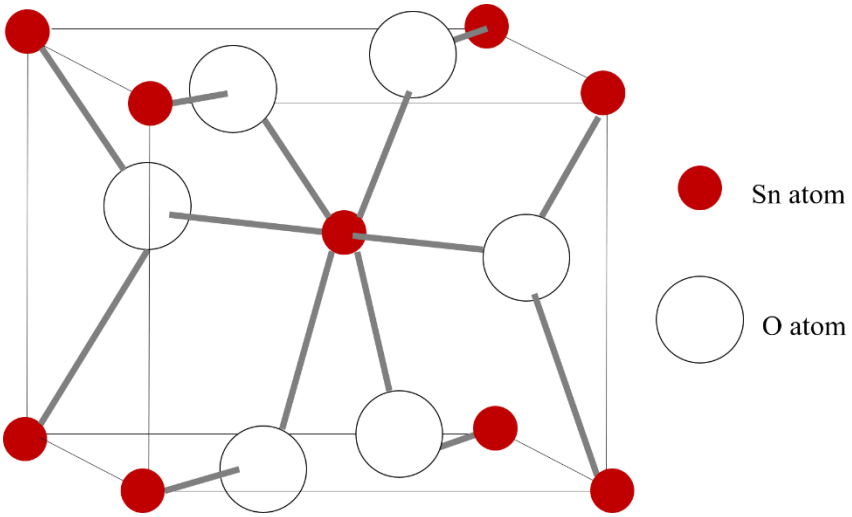

Fig. 4.1 The crystal structure of rutile SnO_2

The SnO_2 nanobelt has high surface to volume ratio. In the surface of the SnO_2 material, the atomic alignment is different from that of bulk material. Meanwhile the band gap is considerably decreasing because of the surface effect. The band structure of reduced surface and stoichiometric surface are investigated [26]. In the reduced surface in which a large number of unbonded Sn atoms are formed, a large number of electrons occupy the band gap states that has higher energy level than the bulk valence band maximum. Thus, in the reduced surface of SnO_2 material, the majority carrier is electron.

The lattice defect is another case that determine the carrier density and the type of majority carrier. To understand how the lattice defect affect the electrical conductivity in SnO_2, a research based on first principle calculations considered the formation energies and electrical (donor, acceptor) levels studied a variety of lattice defects such as O vacancy, Sn interstitial, Sn antistites, Sn vacancy and O interstitial phenomenon under different conditions [27]. This research reveals that Sn interstitial phenomenon

and O vacancy are the major surface defect type in SnO_2. Because of these surface defects, the majority carrier of the undoped SnO_2 is electron [27,28]. Thus, the SnO_2 nanobelt is a pronounced n-type semiconductor material.

4.4 Fabrication of SnO_2 FET

At the beginning of the experiment, the SnO_2 FET is fabricated. Fig.4.2 illustrates the fabrication of the SnO_2 nanobelt FET. By using EBPVD, a 200 nm Au film was fabricated on the back side of an n-type Si substrate. A 500 nm SiO_2 film was fabricated on the n-type Si substrate. The SnO_2 nanobelts were synthesized by thermal sublimation method with average widths and thicknesses of 118 nm and 96 nm, respectively. The suspension of SnO_2 nanobelts in ethanol was prepared by ultrasonic dispersion. Several drops of the suspension were dispersed onto a SiO_2 film and dried at 25 ℃. An SiO_2 film with a thickness of 500 nm was fabricated on an n-type Si substrate with a thickness of 500 μm and an electrical resistivity of 9–11 Ω cm. Using photolithography and EBPVD, the Au electrodes of the FET, which are 100 nm thick terminals were fabricated to connect the SnO_2 nanobelts. Four pairs of main terminals were formed on the left and right sides of the substrate and worked as drain-source electrodes of the FETs. Each main terminal has a comb-like structure with multiple small terminals. The width and length of the small terminals were 15 μm and 250 μm, respectively. The distance between the two small terminals is 15 μm.

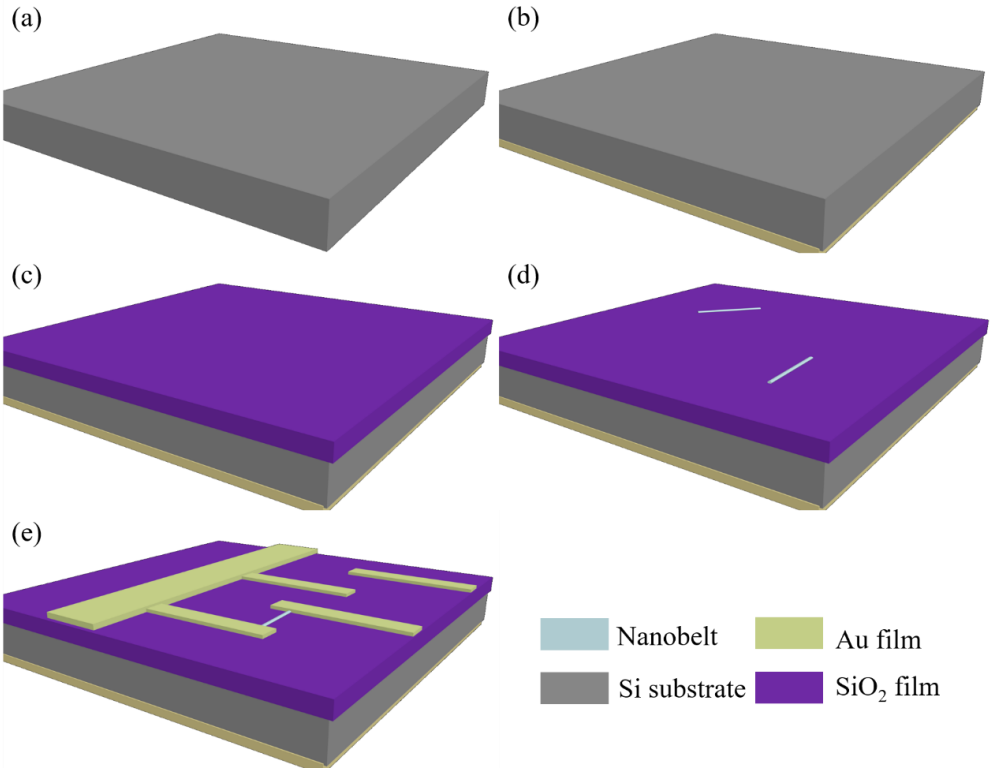

Fig. 4.2 Fabrication of SnO_2 nanobelt FET

Fig. 4.2 shows the sample during fabrication during different steps. Fig. 4. 3 shows the size of structure of the SnO2 nanobelt FET and the SEM observation results. The SEM observation results of the main terminals, small comb-like terminals, and a typical SnO_2 nanobelt connected with two small terminals are shown in Fig. 4.3 (b), (c) and (d), respectively.

After the SnO_2 nanobelt FET is fabricated. A wire bonder (Westbond model 7476D) device is applied to fabricate the bonding part on the drain, gate and source terminals.

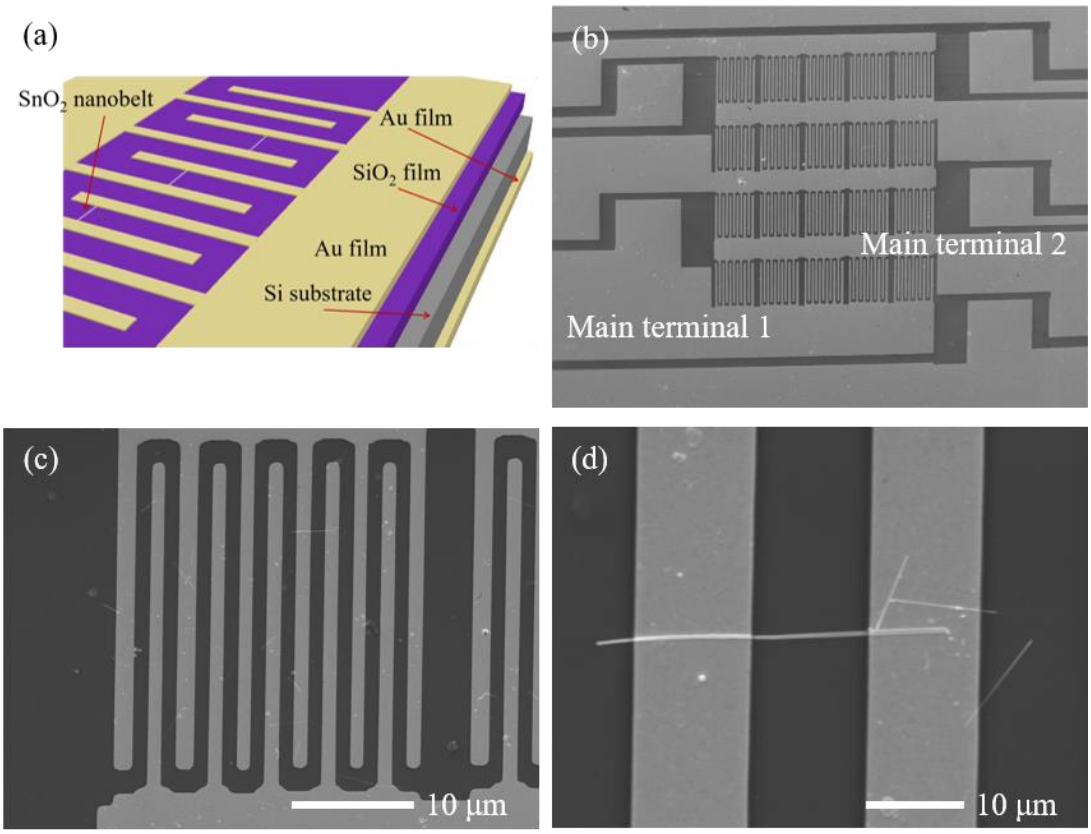

Fig. 4.3 Schematic diagram and SEM images of fabricated SnO_2 nanobelt FET. (a) The schematic diagram of the SnO_2 nanobelt FET. The terminals of the sample connect with a voltage source and function as drain and source terminals. (b) The terminals and electrode are observed by SEM image. (c) and (d) illustrate the electrodes and nanowires in different magnification.

4.5 Operation Principle of SnO_2 nanobelt FET

In this section, the operation principle of the SnO_2 nanobelt FET is investigated. Specifically, it is necessary to discussed how the carrier density and the electrical conductivity of the SnO_2 nanobelt are changed when the gate voltage is changing.

In Fig.4.4 (a), the structure of the FET is shown. In Fig 4.4 (b), when $V_{gs} < 0$ and $V_{ds} = 0$, the electrical potential of drain and source terminal are 0 V, while that of gate terminal is -12V. Thus, the drain and source terminal attracted positive charge and gate terminal has negative charge. The thermal excited electrons in SnO_2 nanobelt near drain or source are attracted by positive charge forming the depletion regions. When $V_{ds} = 20$ V, the schematic diagram is shown in Fig 4.4 (c). The electrons move from source to drain on the surface of SnO_2 nanobelt due to the electrical potential difference. Because of the depletion regions, the conductivity is low and the current is weak. When the $V_{gs} = 0$ V, $V_{ds} = 20$ V, the diagram is illustrated in Fig 4.4 (d). The depletion regions between the nanobelt and the drain and source terminal respectively decrease. Thus, the carrier in the nanobelt increase and the current from source to drain increase as well. When the $V_{gs} = 12$ V, $V_{ds} = 20$ V, the diagram is illustrated in Fig 4.4 (e). The depletion regions between the nanobelt and the source terminal disappear since $V_{gs} > 0$. The depletion between the nanobelt and the drain terminal considerably decreases, since the potential difference between gate and drain decrease further. Since the depletion region on drain and source decrease, the carrier in the nanobelt increases. The electrical current is also attracted at the bottom of the nanobelt.

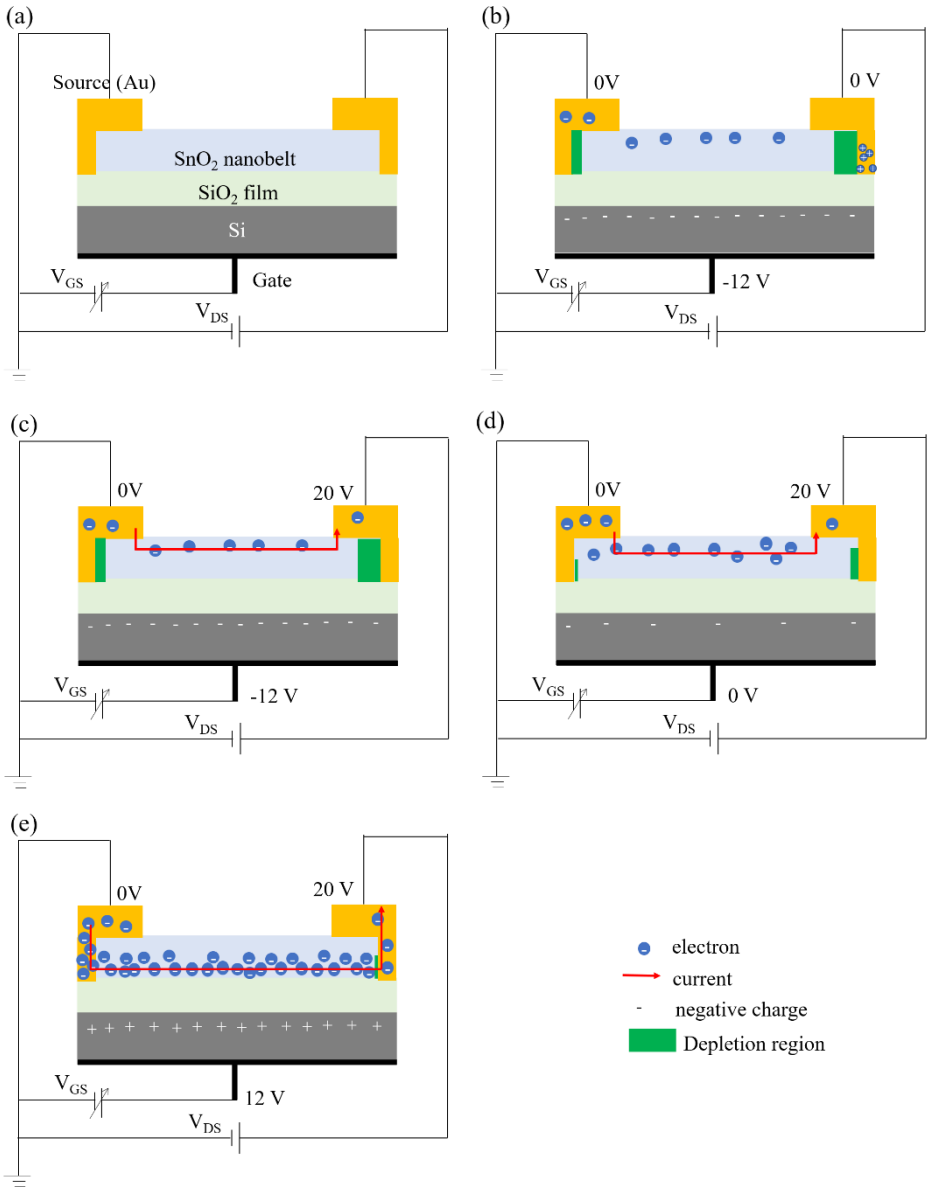

Fig. 4.4 Operation principle of SnO_2 nanobelt FET

4.6 Output characteristics of SnO_2 field effect transistors

By using the two-terminal measurement method, the output characteristic of the SnO_2 nanobelt FET is measured by a test fixture (Agilent Technologies U2941A) in Fig.4.5. Fig. 4. 5 displayed the I_{ds} vs. V_{ds} the output characteristic of the SnO_2 nanobelt

FET. The gate-source voltage V_{gs} is fixed at 12 V, 4 V, 0 V, -4 V and -12 V respectively and the drain-source voltage V_{ds} is fixed at 20 V. Based on the measured I_{ds} - V_{ds} diagram, the conductivity of SnO_2 nanobelt FET at different gate-source voltage is obtained. When V_{gs} was increased, I_{ds} increased correspondingly, which indicates the FET working well. The I_{ds} - V_{ds} curve has a well-defined ohmic region at low biases. As the bias increases, the drain-source current saturates due to the local depletion of carriers around the drain electrode. There is an ohmic region below V_{ds} =10 V, and a saturation region is from V_{ds} being higher than 10 V. Cutoff region is around at V_{gs} having a negative value. The I_{ds} - V_{ds} curve exhibits excellent linearity and saturation characteristics, indicating that the fabricated SnO_2 FET is an n-type semiconductor FET and available for further evaluation by M-AFM.

For comparison with the M-AFM measurements, the average conductivity, σ_T, of a single SnO_2 nanobelt FET under different gate-source voltages was calculated from the measured I_{ds} - V_{ds} results using Eq. (4.8).

$$\sigma_T = I_{ds} V_{ds}^{-1} S^{-1} \left(\frac{1}{l_1} + \frac{1}{l_2} + \frac{1}{l_3} + \frac{1}{l_4}\right)^{-1} , \qquad (4.8)$$

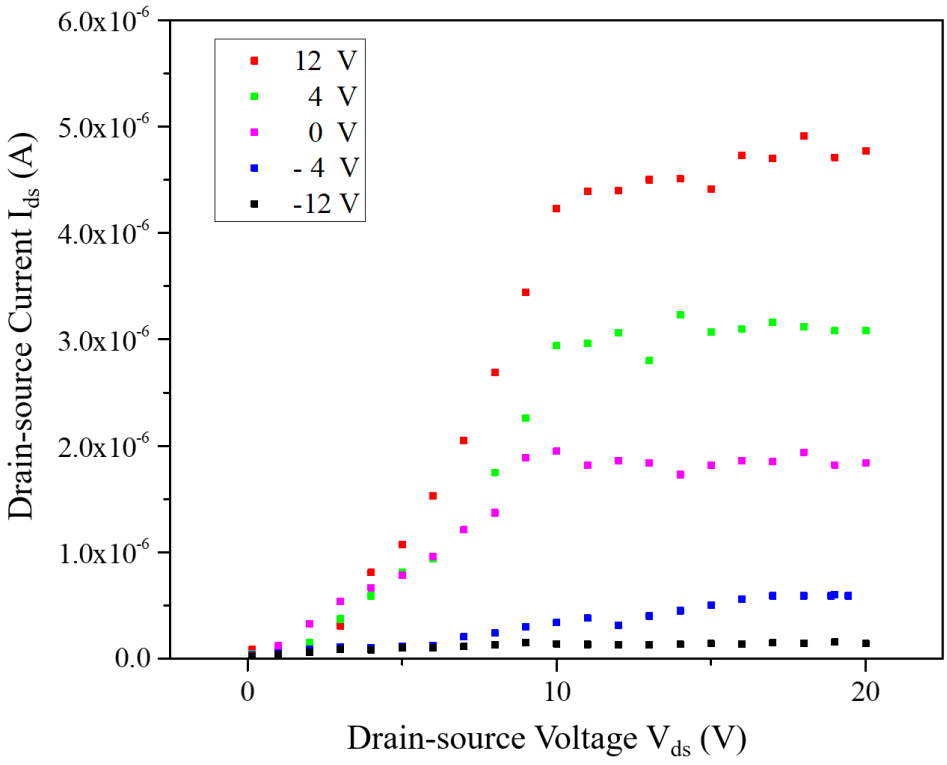

Fig. 4.5 Output characteristics of the SnO_2 nanobelt FETs measured under different back-gate voltages.

4.7 Microwave Images of SnO_2 Nanobelt on the FET

By applying M-AFM, the topographies as well as the microwave image of the nanobelt of the SnO_2 are under the gate-source voltage at -12 V, -4 V, 0 V, 4 V, 12 V, respectively. The drain-source voltage is fixed at 20 V. The average reflected microwave signal of the SnO_2 nanobelt are 13.8 mV, 14.5 mV, 19.4 mV, 21.2 mV, 27.3 mV under -12 V, -4 V, 0 V, 4 V, 12 V respectively according to Fig. 4.6 (a)-(e). In Fig. 4.6, the difference of the reflected microwave signal between the SnO_2 and the SiO_2 film is clearly distinguished by M-AFM. M-AFM can measure the nanomaterials with

high resolution and distinguish the difference of the electrical conductivity of SnO_2 nanobelt between different gate-source voltages. The reflected microwave signals are applied to calculate the conductivity of the SnO_2 nanobelt in different gate-source voltage. By using the theoretical model, the conductivity of the SnO_2 nanobelt under different gate-source voltage are evaluated. The output voltages of the locally reflected microwave signals were obtained from data of the crossed lines (points A to B) through the SnO_2 nanobelt, as illustrated in the microwave images in Fig. 4.7. Based on the output voltages measured at each point, $\left|\Gamma_s\right|$ was determined using Eq. 4.2, and the conductivity of the SnO_2 nanobelt was evaluated using Eq. 4.4 and Eq. 4.5. Here, the relative permittivity of the SnO_2 nanobelt was 11.5. Fig.4.7 compares results from two-terminal measurement method and M-AFM. The conductivities of SnO_2 nanobelt evaluated by M-AFM under -12 V, -4 V, 0 V, 4 V, 12 V are 2.6 S/m, 16.4 S/m, 53.6 S/m, 65.7 S/m, 114.3 S/m, respectively, while results from two-terminal measurement method under -12 V, -4 V, 0 V, 4 V, 12 V are 2.8 S/m, 11.9 S/m, 36.1 S/m, 60.4 S/m, 93.6 S/m, respectively. Displayed in Fig. 4.7, the two results have a similar tendency in that the conductivity increases as V_{gs} increases, because an increased V_{gs} can cause an increase in the carrier density in the SnO_2 nanobelts. These differences could be attributed to the fact that the two-probe method measured four SnO_2 nanobelts, whereas M-AFM measured a single SnO_2 nanobelt. Moreover, that the error bar was relatively large for V_{gs} = 12 V, which may be due to the increased conductivity of the nanobelt and the system noise of the microwave measurement.

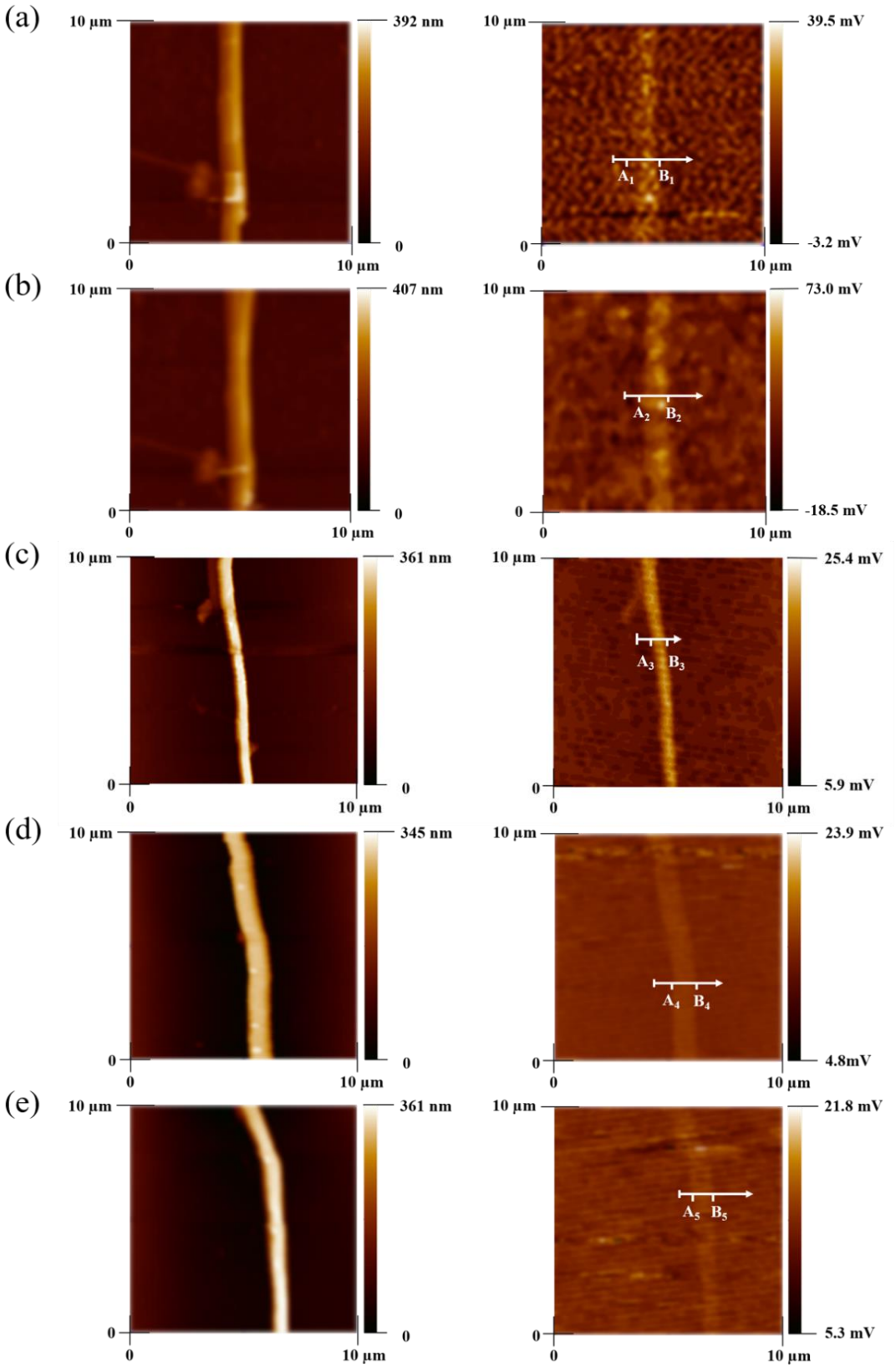

Fig. 4.6 Morphology and microwave images of SnO_2 nanobelt FET scanned by M-AFM. (a) morphology and microwave images measured at V_{gs} = 12 V. (b)

morphology and microwave images measured at V_{gs} = 4 V. (c) morphology and microwave images measured at V_{gs} = 0 V. (d) morphology and microwave images measured at V_{gs} = - 4 V. (e) morphology and microwave images measured at V_{gs} = - 12 V.

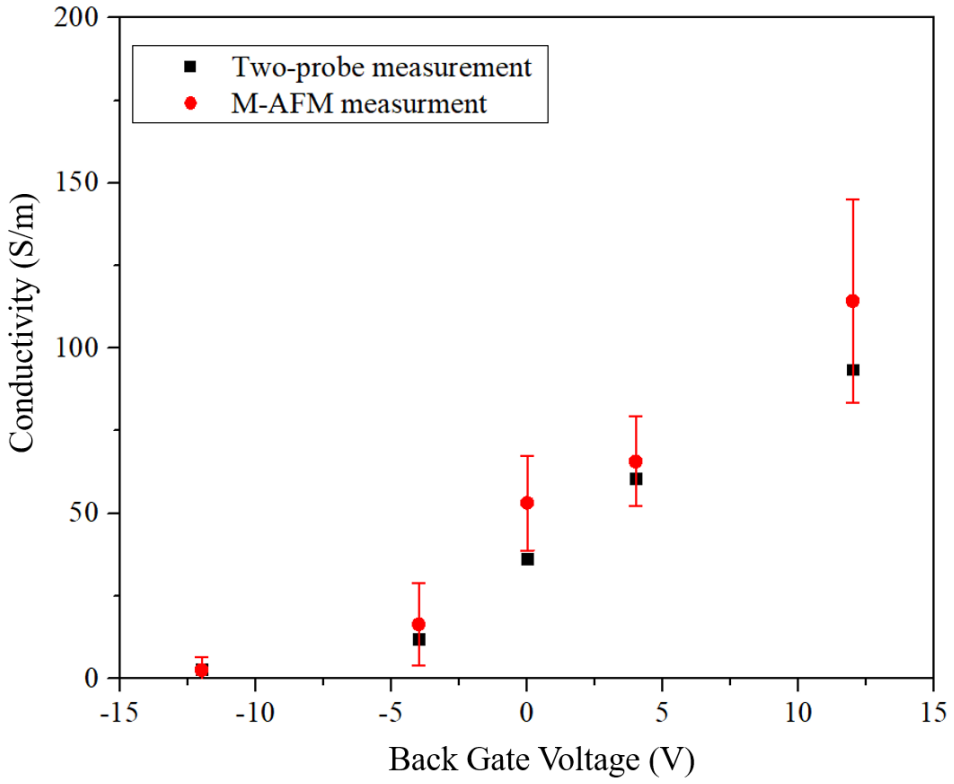

Fig. 4.7 Evaluation values of conductivity measured by M-AFM compared with that measured by two-terminal measurement method.

4.8 Discussion

4.8.1 The interaction between the M-AFM probe and SnO_2 nanobelt FET

However, the error still exists. Morphologically, the nanobelt becomes wider when the value of V_{gs} changes, either positive or negative. In Fig.4.8, the evaluated width and reflected microwave signal of SnO_2 nanobelt are illustrated. The widths of SnO_2 nanobelt evaluated by M-AFM in microwave images are in agreement with those measured in topography images. However, the widths of SnO_2 nanobelt evaluated by M-AFM in topography images under -12 V, -4 V, 0 V, 4 V, 12 V are 1190 nm, 1058 nm, 508 nm, 1063 nm, and 780 nm, respectively. Thus, it is necessary to discuss the reason why the evaluated width of the SnO_2 nanobelt changes when the V_{gs} changes.

This may be due to the edge effect of charges induced by V_{gs} under the nanobelt. These charges could impact the tip of the probe, thereby causing errors during the measurement. In the microwave image, the nanobelt was observed to be homogeneous in its length direction, because the edge effect of the carrier distribution near the drain and source electrodes was limited, and the measurement area was located at the center of the nanobelt. Here, the influence of the back-gate voltage and carrier in nanobelt to the probe are analyzed.

When $V_{gs} \neq 0$, the nanobelt measured by M-AFM is getting wider. This phenomenon is caused by the current flowed through the SnO_2 nanobelt and the gate

voltage.

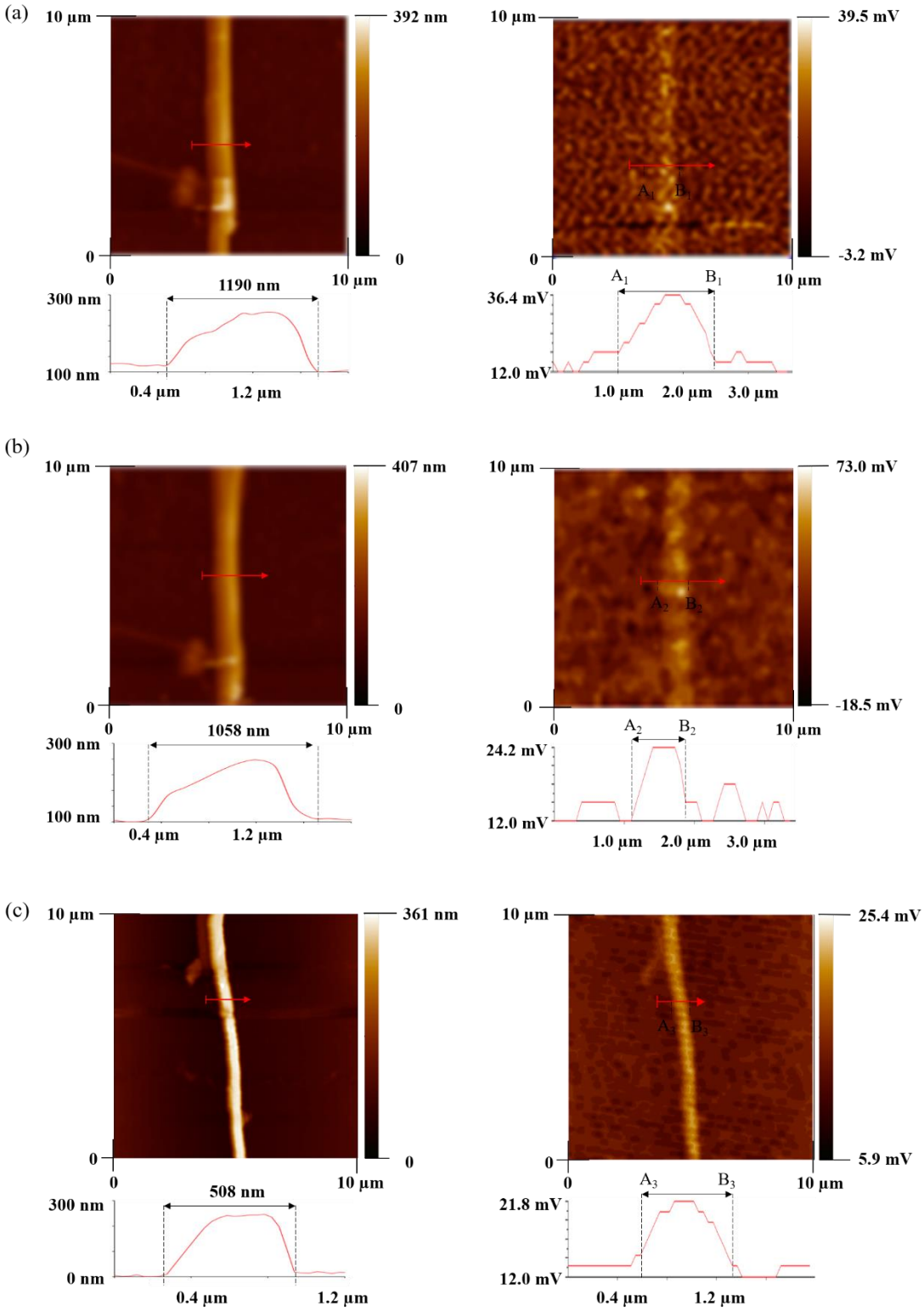
(a)
10 μm
392 nm
0
0
0
10 μm
1190 nm
300 nm
100 nm
0.4 μm
1.2 μm
10 μm
39.5 mV
-3.2 mV
A1
B1
36.4 mV
12.0 mV
1.0 μm
2.0 μm
3.0 μm
(b)
10 μm
407 nm
1058 nm
300 nm
100 nm
0.4 μm
1.2 μm
73.0 mV
-18.5 mV
A2
B2
24.2 mV
12.0 mV
(c)
10 μm
361 nm
508 nm
300 nm
0 nm
0.4 μm
1.2 μm
25.4 mV
5.9 mV
A3
B3
21.8 mV
12.0 mV

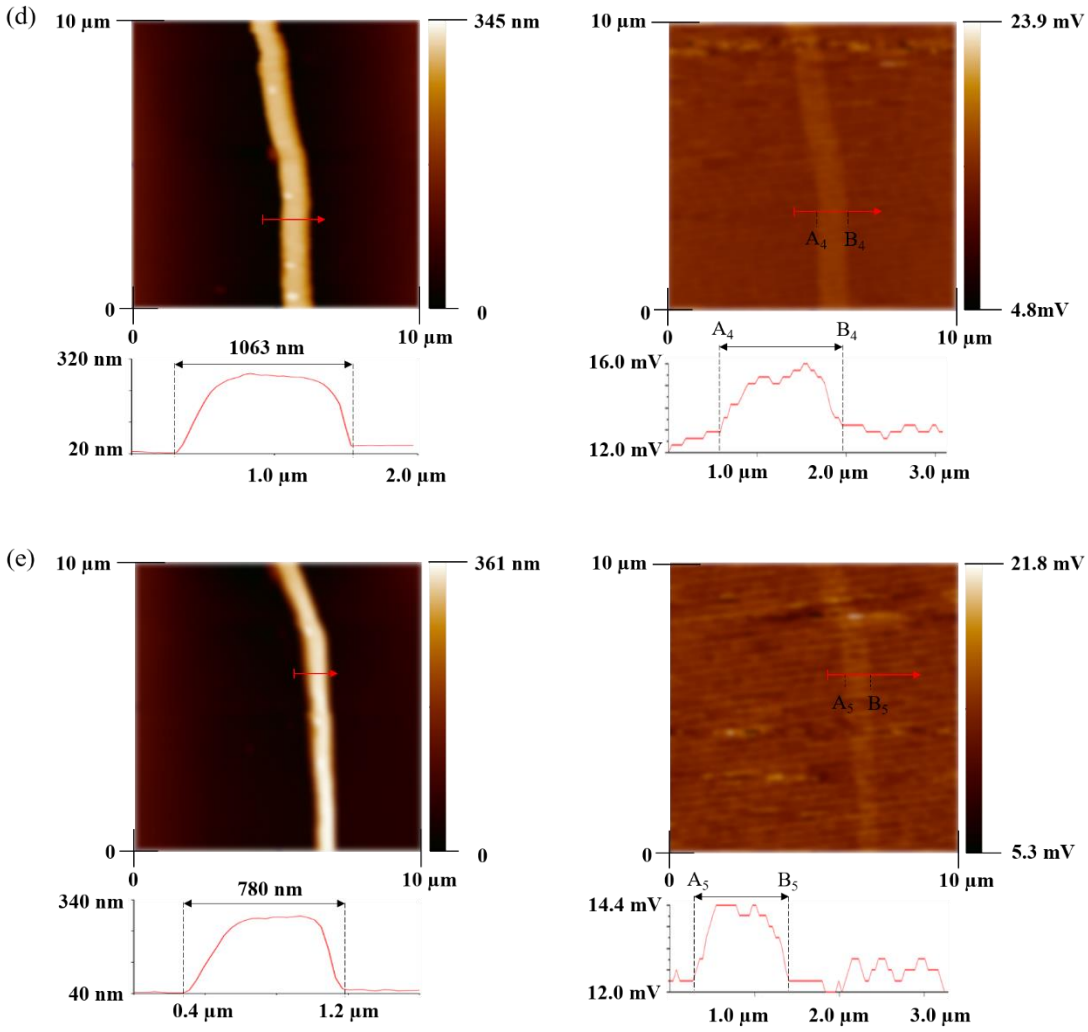

Fig. 4.8 The evaluated width and reflected microwave signal of SnO_2 nanobelt.

When M-AFM is working, half of the probe tip interacts with atoms on the nanobelt as it approaches the edge of the nanobelt. This interaction changes the resonant frequency of the probe during vibration. When the resonant frequency of the probe is changed, the probe lifts as well. The resonant frequency is given by the following equation.

$$\Delta f = \frac{f_0}{2k} k_{ts} \qquad (4.9)$$

Where,

$$k_{ts} = \frac{\partial^2 V_{ts}}{\partial z^2} \qquad (4.10)$$

$\frac{\partial^2 V_{ts}}{\partial z^2}$ is the deviation of the interatomic force between the M-AFM tip and sample.

In Fig. 4.9, the interaction between the tip and SnO_2 nanobelt FET is illustrated.

The structures of the M-AFM probe and SnO_2 nanobelt FET are respectively introduced in Fig. 4. 9 (I). As shown in Fig. 4. 9 (I), the probe is scanning across the nanobelt. The SiO_2 film is 500 nm, and N type silicon substrate under the SiO_2 film is 500 μm. An Au film that is under the silicon substrate is connected to the back gate voltage and fabricated.

When the probe is scanning over the doped Si-substrate that is uniformly charged with positive charge, an electrical field is formed from the bottom to the top of the SiO_2 film, as shown in Fig. 4. 9 (II). When M-AFM is working, the two halves of the probe tips have different charge. The charges from the Si-substrate interact simultaneously with the charge on the M-AFM tips. Since the force has same intensity but opposite direction. Thus, the V_{ts} is the Van der Waals potential which only depend on the intermolecular force.

Shown in Fig. 4. 9 (III), the probe is scanning over the Si-substrate which is uniformly charged with negative charge. An electrical field is formed from the top to the bottom of the SiO_2 film. The interaction between tip and sample is the intermolecular force which has the same amplitude and opposite direction compared

with that in Fig. 4. 9 (II).

As shown in Fig. 4. 9 (IV), the probe is scanning across the SnO_2 nanobelt when $V_{gs} = 0$ V. The electrons that are evenly distributed in the nanobelt flow through the nanobelt. And the interaction between tip and sample is the intermolecular force as well. Thus, V_{ts} can be write in the following equation in the Fig. 4. 9 (I)-(IV).

$$V_{ts} = V_{VDW} \qquad (4.11)$$

Where V_{VDW} is the potential of Van Der Waals force.

When $V_{gs} > 0$ V, positive charges are formed on the Si-substrate as shown in Fig. 4. 9 (V). The current in the nanobelt will change the distribution of the positive charge in the Si-substrate. Specifically, the positive charges are attracted and approaches to the area under the SnO_2 nanobelt because of the electrical current in the nanobelt. Thus, a small area on the Si substrate on the both sides of the nanobelt will contain less positive charge. When the tip is far from the sample, the potential between tip and sample can be represented by Eq. (4.11). When the tip is approaching the sample, the tip-sample potential V_{ts} is consist of 2 interactions. One is the intermolecular force potential. Another one is contributed by the electrical potential due to the asymmetric distribution of positive charges on the Si substrate surface. More specifically, the half of the M-AFM tip on the right side has electrical interaction with the positive charges while that on the left side is scanning the area without positive charges, in Fig. 4. 9 (V). Thus, V_{ts} is changed as the following equation.

$$V_{ts} = V_{VDW} + V_E \qquad (4.12)$$

where V_E is the potential from the electrical charge. When the force from the electric field is larger than the threshold of AFM, the M-AFM probe lifts no matter whether the probe is directly over the nanobelt or not, which results in a wider nanobelt measured by M-AFM.

When $V_{gs} < 0$ V, negative charges are formed on the Si-substrate as shown in Fig. 4. 9 (VI). The current in the nanobelt will repel the distributed negative charge on the Si-substrate. More specifically, the negative charges are repelled and leave the area under the SnO_2 nanobelt because of the electrical current in the nanobelt. The area on the Si substrate near the nanobelt will contain more negative charges that are repelled by the electron current of the SnO_2 nanobelt. Thus, the negative charge near the SnO_2 nanobelt is distributed unevenly. The side that is close to the nanobelt has fewer negative charges while the one that is far from the nanobelt has more. When the tip is approaching the sample, the tip-sample potential V_{ts} is also consist of the intermolecular force potential and the electrical potential of negative charges on the Si substrate surface. The two halves of the M-AFM tips receive the electrical interaction from the sample, as shown in Fig. 4. 9 (VI). The half tip on the right side has a stronger electrical interaction with the negative charges while the one on the left side is weaker. Because of the different interactions on the two halves of the M-AFM tip, V_{ts} should be represented by Eq. (4.12). Thus, the nanobelt measured become

wider When $V_{gs} < 0$ V.

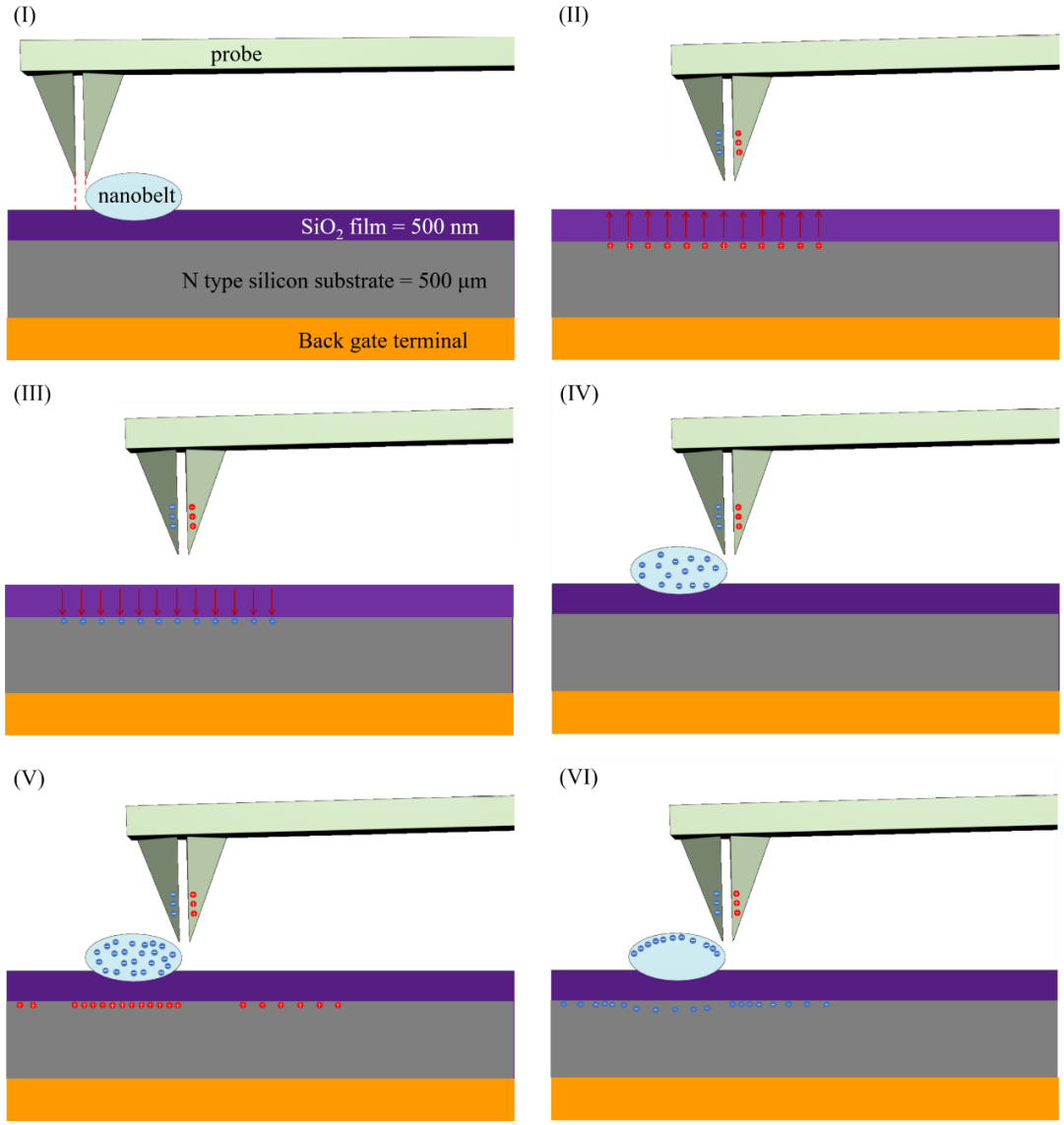

Fig. 4.9 Charge influence during the evaluation of nanobelt FET.

4.8.2 Frequency dependance of conductivity and the influence of the different frequency between M-AFM and two-terminal method

Electrical conductivity is defined with the relationship between current density and electric field amplitude by the following equation:

$$J = \sigma E \qquad (4.13)$$

Where J is current density, σ is electrical conductivity, E is electric field amplitude.

When a conductor is exposed at an altering electrical field, the charge carriers in the conductor response to the change of the electric field. And the electrical conductivity is represented as below [29]:

$$\sigma(\omega) = \sigma_{dc} + \sigma_{ac} \qquad (4.14)$$

Where $\sigma(\omega)$ is the electrical conductivity, σ_{dc} is the dc conductivity. And σ_{ac} is the ac conductivity. When frequency increase, σ_{ac} rises monotonously according to the frequency power [29]. Meanwhile, σ_{ac} is a complex value. The imaginary part represents the phase lag between the electric field and current density.

More specifically, the electrical conductivity of a semiconductor in an alternating electrical field can be represent as follows [30][31] according to the Drude-Smith model:

$$\sigma(\omega) = \frac{Ne^2\tau}{m^*(1-i\omega\tau)}\left[1 + \sum_{j=1}^{\infty}\frac{c_j}{(1-i\omega\tau)^j}\right] \qquad (4.15)$$

Where ω is the frequency of the electrical field, e is the electron charge, m^* is the effective electron mass, τ is the scattering time that is an average time before a random electron makes it next collision, c_j is the velocity of the electron after collision with positive ion after a number of j collision.

In our experiment, the SnO_2 nanobelt FET is connected in a direct current circuit during both of the evaluations by M-AFM and two-terminal measurement method. Thus, the electrical conductivity of SnO_2 nanobelt FET evaluated by M-AFM is the same with that evaluated by two-terminal measurement method when external altering electrical field is not induced.

When the SnO_2 nanobelt FET is measured by M-AFM, part of the SnO_2 nanobelt is exposed at the 94 GHz microwave that is high frequency alternating electrical field. Thus, the influence of the microwave on the conductivity should be discussed.

In the discussion part of Chapter 3, it is demonstrated that the polarization of the atoms on the sample surface is dipolar polarization when measured by M-AFM, and the change of the relative permittivity of the one-dimensional nanomaterials are negligible. Since the σ_{ac} is caused by the change of real and imaginary part of relative permittivity. Thus, the influence of 94 GHz microwave on the conductivity of SnO_2 nanobelt is negligible.

Moreover, the conductivity of SnO_2 nanowire is quantitatively investigated by a time resolved terahertz spectroscopy in terahertz frequency range [31]. When the frequency is 250 GHz (0.25 THZ), the real part of the conductivity of SnO_2 nanowire is 55.6 S/m and the imaginary part is -9.6 S/m [31]. The study indicated the following 2 points.

Firstly, the σ_{dc} is much more significant than σ_{ac} when the microwave frequency of M-AFM is around 100 GHz for the SnO_2 material. Secondly, phase lag between the electric field and current density is small and can be negligible at 100 GHz.

As a result, the influence of 94 GHz microwave on the conductivity of SnO_2 nanobelt is negligible.

4.9 Summary

The main results of this research are summarized as follows: In this study, SnO_2 nanobelt FETs were fabricated and their output characteristics were measured. The topography and microwave images of a SnO_2 nanobelt FET were simultaneously analyzed by M-AFM, and the local conductivity of the nanobelt was quantitatively evaluated. The proposed method has prospects in the local conductivity measurement of nanomaterial FETs, as well as FET-based sensors, regarding carrier density changes caused by gas, biomolecules, chemicals, and ions on the surface of the nanomaterials.

Reference

[1] L. Villamagua, A. Stashans, P. Lee, Y. Liu, C. Liu, and M. Carini, Change in the electrical conductivity of SnO2 crystal from n-type to p-type conductivity, Chemical Physics, **452**, 71 (2015).

[2] J. Pan, H. Shen, and S. Mathur, One-dimensional SnO2 nanostructures: synthesis and applications, Journal of nanotechnology, **2012** (2012).

[3] Z. Pan, Z. Dai and Z. Wang, Nanobelts of semiconducting oxides, Science, **291** [5510], 1947 (2001).

[4] C. Lieber, Nanoscale science and technology: building a big future from small things, MRS bulletin, **28** [7], 486 (2003).

[5] A. Nehra and K. S, Current trends in nanomaterial embedded field effect transistor-based biosensor, Biosensors Bioelectronics, **74**, 731 (2015).

[6] A. Zhang and C. Lieber, Nano-bioelectronics, Chemical reviews, **116** [1], 215 (2016).

[7] L. Syedmoradi, A. Ahmadi, M. Norton, and K. Omidfar, A review on nanomaterial-based field effect transistor technology for biomarker detection, Microchimica Acta, **186** [11], 1 (2019).

[8] G. Shin, M. Bae, H. Lee, S. Hong, C. Yoon, G. Zi, J. Rogers, and J. Ha, SnO2 nanowire logic devices on deformable nonplanar substrates, ACS nano **5** [12], 10009 (2011).

[9] Y. Huang, X. Duan, Y. Cui, L. Lauhon, K. Kim and C. Lieber, Logic gates and computation from assembled nanowire building blocks, Science, **294** [5545], 131

(2001).

[10] E. Comini, G. Faglia and G. Sberveglieri, Stable and highly sensitive gas sensors based on semiconducting oxide nanobelts, Applied Physics Letters **81** [10], 1869 (2002).

[11] M. Zhuo, Y. Chen, J. Sun, H. Zhang, D. Guo, H. Zhang, Q. Li, T. Wang, and Q. Wan, Humidity sensing properties of a single Sb doped SnO2 nanowire field effect transistor, Sensors and Actuators B: Chemical, **186**, 78 (2013).

[12] K. Choi, and H. Jang, One-dimensional oxide nanostructures as gas-sensing materials: review and issues, Sensors, **10** [4], 4083 (2010).

[13] Y. Cheng and P. Xiong, Mechanism and optimization of pH sensing using SnO2 nanobelt field effect transistors, Nano letters **8** [12], 4179 (2008).

[14] Y. Cheng, K. Chen, N. Meyer, J. Yuan, L. Hirst, P. Chase, and P. Xiong, Functionalized SnO2 nanobelt field-effect transistor sensors for label-free detection of cardiac troponin, Biosensors and Bioelectronics **26** [11], 4538 (2011).

[15] X. Duan, Y. Huang, Y. Cui, J. Wang, and C. Lieber, Indium phosphide nanowires as building blocks for nanoscale electronic and optoelectronic devices, Nature, **409** [6816], 66 (2001).

[16] F. Qian, S. Gradecak, Y. Li, C. Wen, and C. Lieber, Core/multishell nanowire heterostructures as multicolor, high-efficiency light-emitting diodes, Nano letters, **5** [11], 2287 (2005).

[17] D. Gupta, N. Goktas, A. Rao, R. Lapierre, and O. Rubel, Stacking defects in GaP nanowires: Electronic structure and optical properties, Journal of Applied Physics, **126**

[8], 084306 (2019).

[18] B. Wang, T. Stelzner, R. Dirawi, O. Assad, N. Shehada, Silke Christansen, and H. Haick, Field-effect transistors based on silicon nanowire arrays: effect of the good and the bad silicon nanowires, ACS Applied Materials & Interfaces, **4** [8], 4251 (2012).

[19] O. Gunawan, L. Sekaric, A. Majumdar, M. Rooks, J. Appenzeller, J. Sleight, S. Guha, and W. Haensch, Measurement of carrier mobility in silicon nanowires, Nano letters, **8** [6], 1566 (2008).

[20] M. Kim, H. Park, H. Lee, K. Nam, S. Jeong, I. Omkaram, D. Yoon, S. Lee, S. Kim, and S. Lee, Research Update: Nanoscale surface potential analysis of MoS2 field-effect transistors for biomolecular detection using Kelvin probe force microscopy, APL Materials, **4** [10], 100701 (2016).

[21] X. Gao, G. Zheng and C. M. Lieber, Subthreshold regime has the optimal sensitivity for nanowire FET biosensors, Nano letters, **10** [2], 547 (2010).

[22] M. Bashouti, R. Tung and H. Haick, Tuning the electrical properties of Si nanowire field‐effect transistors by molecular engineering, Small **5** [23], 2761 (2009).

[23] L. Zhang, Y. Ju, A. Hosoi, and A. Fujimoto, Microwave atomic force microscopy: quantitative measurement and characterization of electrical properties on the nanometer scale, Applied Physics Express **5** [1], 016602 (2011).

[24] L. Liu and Y. Ju, Nondestructive measurement and high-precision evaluation of the electrical conductivity of doped GaAs wafers using microwaves, Review of Scientific Instruments **81** [12], 124701 (2010).

[25] S. Das, and V. Jayarama, SnO2: A comprehensive review on structures and gas

sensors, Progress in Materials Science, **66**, 112 (2014).

[26] M. A. Mäki-Jaskari, and T. T. Rantala, Band structure and optical parameters of the SnO2 (110) surface, Physical Review B, **64** [7], 075407 (2001).

[27] C. Kılıc, and A. Zunge, Origins of coexistence of conductivity and transparency in SnO2, Physical review letters, **88** [9], 095501 (2002).

[28] Z. Zhou, Y. Min, X. Liu, J. Ding, J. Guo, F. Hu, and L. Liu, Regulation of oxygen vacancy types on SnO2 (110) surface by external strain, AIP Advances, **6** [5], 055102 (2016).

[29] S. R. Elliott, Ac conduction in amorphous chalcogenide and pnictide semiconductors, Advances in physics, 36 **[2]**, 135 (1987).

[30] N. V. Smith, Classical generalization of the Drude formula for the optical conductivity, Physical Review B, **64** [15], 155106 (2001).

[31] D. Tsokkou, A. Othonos, M. Zervos, Carrier dynamics and conductivity of SnO2 nanowires investigated by time-resolved terahertz spectroscopy, Applied physics letters, **100** [13], 133101 (2012).

Chapter 5 Conclusions

The nanomaterials, including nanowires, nanotubes, nanobelts, etc., have been attracting considerable attention during the past decade, because the high surface to volume ratio, surface effect and good electrical property make them promising as building blocks for electrical devices, biological sensors, light-emitting diodes, field effect transistors, solar cells, and so on. The corresponding evaluation method for the electrical property of nanomaterials is in great need. On the other hand, the M-AFM combined with the merit of non-contact AFM and microwave measurement is the promising candidate for the local electrical property evaluation.

In this study, the microwave measurement system and AFM system were respectively investigated. Then, the M-AFM probes were fabricated. To verify the reliability of the M-AFM probes, the fabricated probes were evaluated by M-AFM system.

The method of evaluating the relative permittivity by force-curve based on M-AFM was established to evaluate one-dimensional nanomaterials. As the first step of this research, the morphology and microwave images of ZnO, CuO nanowires and SnO_2 nanobelts are measured by the M-AFM. Then, the quantitative evaluation of the relative permittivity of the metal oxide nanomaterials was succeeded based on the force curves measurement of M-AFM. The evaluated relative permittivity based on the force curves by M-AFM agrees with the nominal value with high reproducibility. The experimental result reflects that the M-AFM is a favorable technique to evaluate the relative

permittivity of the one-dimensional nanomaterial.

The electrical conductivity of a SnO_2 nanobelt FET was evaluated by M-AFM. In the experiment, a SnO_2 nanobelt-based FET device was fabricated, and the local conductivity of the SnO_2 nanobelt affected by gate voltages was evaluated. M-AFM measures the topography and microwave image of the SnO_2 nanobelt in the non-contact mode with high resolution. Based on the measured microwave image, the electrical conductivities of the single SnO_2 nanobelt under different gate voltages were obtained, which is significant for understanding the function and performance of the SnO_2 nanobelt FET.

In summary, there are two main findings in this study. Firstly, it is proved that the M-AFM technique can evaluate the in-situ relative permittivity of the one-dimensional nanomaterials. Next, the electrical conductivity of the SnO_2 nanobelt FET was determined successfully. These results indicate that the M-AFM is a promising candidate to evaluate the electrical properties of one-dimensional nanomaterials.

Acknowledgments

To begin with, I'd like to give my hearty thankfulness to my supervisor, professor Y. Ju, for allowing me to study under his research team. His original perspectives and assistance constantly have fueled my growth and research. I learnt how to do research with his wise advice and enthusiastic devotion to science. In addition to academic life, his help and support have made my life in Japan much easier. Sincere thanks again to professor Y. Ju during my 8-year study.

Secondly, I want to give my sincere appreciation to professor K. Fukuzawa, professor K. Sasagawa at Hirosaki University, and associate professor Y. Toku. Their valuable advice allowed me to revise my thesis more thoroughly.

Thirdly, assistant professor Y. Kimura is the next one I want to thank for his meaningful suggestions, with which I conquered many difficulties.

Additionally, the financial support from PhD Professional: Gateway to Success in Frontier Asia is of great significance. Their events incredibly expanded my outlook on other research fields as well.

Finally, allow me to thank my wife and parents for their constant spiritual and financial support, which has motived me to pursue my academic dream.